This electronic thesis or dissertation has been downloaded from the King's Research Portal at https://kclpure.kcl.ac.uk/portal/

KING'S College LONDON

Development and calibration of soft X-ray microprobes for cellular irradiation

Arachchi Appuhamilage, Indika Pathirana

Awarding institution:
King's College London

The copyright of this thesis rests with the author and no quotation from it or information derived from it may be published without proper acknowledgement.

END USER LICENCE AGREEMENT

Unless another licence is stated on the immediately following page this work is licensed

under a Creative Commons Attribution-NonCommercial-NoDerivatives 4.0 International

licence. https://creativecommons.org/licenses/by-nc-nd/4.0/

You are free to copy, distribute and transmit the work

Under the following conditions:

- Attribution: You must attribute the work in the manner specified by the author (but not in any way that suggests that they endorse you or your use of the work).
- Non Commercial: You may not use this work for commercial purposes.
- No Derivative Works - You may not alter, transform, or build upon this work.

Any of these conditions can be waived if you receive permission from the author. Your fair dealings and other rights are in no way affected by the above.

Take down policy

If you believe that this document breaches copyright please contact librarypure@kcl.ac.uk providing details, and we will remove access to the work immediately and investigate your claim.

Download date: 04. May. 2023

Development and calibration of soft X-ray microprobes for cellular irradiation

Indika S. Pathirana Arachchi Appuhamilage

A thesis submitted to King's College London for the degree of

Master of Philosophy in Physics

2014

Department of Physics, King's College London

Abstract

The aim of this project was to design and build two different soft X-ray microprobe systems, MK I and MK III. The purpose of developing both sources was to study the biological cell damages due to focused soft X-rays.

The MK I microprobe employs low energy photons of Carbon K X-rays of 278 eV. An epi-fluorescence microscope, X-ray focusing elements assembly and a cell stage were designed to locate individual cells precisely. The MK I source calibration procedure and results are discussed in this thesis. A custom built proportional counter was used to measure X-ray outputs.

MK III is a novel design for different X-ray targets of Carbon, Aluminum and Chromium K X-rays. An electron focusing lens was designed with two pole pieces to focus X-rays into a small spot on the target. The Field Precision software package was used to simulate the electrons that focus into the X-ray targets. A phosphor screen was used to visualize and align the electron spot without any focusing elements.

This thesis reports the development of the two different microprobe facilities, describing the theoretical principles and the technical problems faced during those developments.

Acknowledgements

First of all I would like to thank my supervisor the late Professor Alan Michette for his guidance and supervision that he provided me until the last moment of his life. He gave me many suggestions in my studies as well as in life and let me feel United Kingdom like a second home to me. I am also grateful to Dr. Slawka Pfauntch for her valuable guidance given me throughout this period. This sudden death of my supervisor has changed the entire research project and all research equipments were moved to Imperial College due to supervisory issue.

I would like to offer my heartiest gratitude to Professor David Richard, the head of the department of Physics at King's College for handling this unexpected situation wisely and for the courage he gave me, to complete my studies. Professor Roland Smith of Imperial College guided me to complete rest of the research and teach me very important aspects of experimental procedures. I really appreciate the guidance, enthusiasm and kindness he showed me throughout this period. Special thanks to Professor Anatoly Zayats, current supervisor at King's and my second supervisor, Dr. Sergi Gracia-Manyes for their help and discussion in my hard times.

I am also grateful to many colleagues, technical and administrative staff at King's and Imperial College. My studies were impossible without the financial support given by the Sri Lankan government and department of Physics at King's College London.

The opportunity to complete this research would not have been possible without my wife Saumya, son Aken and my parents. Without their strong support, encouragement and patience, it would not become successful.

Contents

Chapter 3. Microprobe source calibration

Chapter 4. MK III - an extensible micro-irradiation facility

List of Figures

Chapter 1. Introduction

Chapter 2. The re-instating of a microfocus X-ray source MK I for biological experiments

Chapter 3. Microprobe source calibration

Chapter 4. MK III - an extensible micro-irradiation facility

List of Tables

Publications, Abstract and Presentations

Publications

1. **Indika Arachchi Appuhamilage**, Saleh S. Alatabi, Daniel Adjei, Radhwan Alnaimi, Alan Michette, Slawka Pfauntsch. "Development of a Soft X-Ray Microprobe for Radiobiology Studies". Accepted and Processing at Journal of Acta Physica Polonica A 2014.

2. Radhwan Alnaimi, Daniel Adjei, Saleh Alatabi, **Indika Arachchi Appuhamilage**, Alan Michette. "King's College Laser Plasma X-Ray Source Design". Published in Proceedings of SPIE volume 8777: Damage to VVU, EUV, and x-ray optics IV: and EUV and x-ray optics: synergy between laboratory and Space III, May 2013.

Abstract

1. **Indika Arachchi Appuhamilage**, Daniel Adjei, Alan Michette "Re-instating the ultrasoft-soft X-ray microprobe for radiobiological studies" in XLVIII Zakopane School of Physics, Poland, book of abstracts, ISBN 978-83-63542-009, P26, 2013.

Oral Presentations

1. **Indika Arachchi Appuhamilage**, Saleh Alatabi and Alan Michette "Modeling of Water-cooling Electron Focusing lens", presented at the Experimental Biophysics and Cell biology Group meeting at Queen's University, Belfast, Northern Ireland, November 14, 2011.

2. **Indika Arachchi Appuhamilage**, Alan Michette and Slawka Pfauntsch "Studies of radiation-induced cancers " in Physics Rounds seminar at the London Regional Cancer Program, University of Western Ontario, Ontario, Canada, February 16, 2012.

3. **Indika Arachchi Appuhamilage**, Daniel Adjei, Alan Michette and Slawka Pfauntsch "Development of soft X-ray microprobe" in DoReMi - Modelling radiation effects from initial physical events program, Department of Physics, University of Pavia, Pavia, Italy, May 27 - June 7, 2013.

Poster Presentations

1. **Indika Arachchi Appuhamilage**, Alan Michette and Slawka Pfauntsch "Silica mirrors for cell and tissue probing" Applications of X-ray microtomography on heterogeneous materials, 21st Jyväskylä summer school, Finland, 08 – 19 August 2011.

2. **Indika Arachchi Appuhamilage**, Daniel Adjei, Alan Michette and Slawka Pfauntsch "The soft X-ray microprobe for radiobiological studies" XLVIII Zakopane School of Physics, Zakopane, Poland. Breaking frontiers; submicron structures in physics and biology, 20 – 25 May 2013.

CCD	Charged-Coupled Device
DNA	Deoxyribonucleic acid
dsb	Double Strand Break
ICRU	International Commission of Radiation Units and Measurements
LET	Linear Energy Transfer
MCA	Multi-Channel Analyser
OSA	Order Selecting Aperture
PC	Personal Computer
RBE	Relative Biological Effectiveness
UV	Ultra Violet

Chapter 1

Introduction

1.1 Introduction

Radiation is the term used to describe energy transfer between points via electromagnetic waves or energetic particles. Often considered sinister, radiation is an ever-present phenomenon that exists everywhere. Life on earth has developed in a background radiation field of ultraviolet, natural radioisotopes and cosmic rays. This thesis describes the development of a tabletop soft X-ray (278 eV) micro radiation system generating a quasi-monochromatic (278 eV) microfocused beam for investigating the effects of low doses on cells and tissues (Folkard *et al*., 1997c). This chapter introduces radiation and interactions together with the history of the existing radiobiological microbeam facilities.

The main aim of this project is the development of two different microprobe facilities to irradiate cells and sub cellular organelles with different energy of X-rays. Initial chapters discuss re-instating an electron beam driven 'microfocus' source termed MK I. The second source based on this design and termed MK III is a novel design. MK I was mainly 'low energy' Carbon K X-rays (278 eV) to carry out experiments based on cell irradiation and damage assessment. This type of microprobe has been very popular in other scientific fields including scanning microscopy (Jacobsoen, 1999).

1.2 Scientific rationale

Radiation biology investigates the interaction of ionizing radiation with living organisms. Ionizing radiation is commonly used in cancer therapy and radiation biology studies. Ionizing radiation can damage DNA and then trigger transformation from healthy to cancerous cells. Radiation biology methods can be used to estimate the hazards of such as transformation caused by therapy, the application of radiation sources in medical diagnostics, the everyday exposure to background radiation from natural radioactivity or cosmic rays and the exposure to higher doses during intercontinental flights or occupational exposure of workers in the nuclear industry, medical and scientific laboratories.

Irradiation of single cells with X-rays requires beam shaping to a spot comparable to the dimension of the cell (~ 10 μm diameter for HeLa cells). To enable good interpretation of results and more precise evaluation of the irradiation dose either a monochromatic beam or one with a small energy range should be used. X-ray beams from modern synchrotrons, which remain very intense even after passing through monochromating, can be shaped to small sizes without focusing, using only collimation by ultra-precise slits. Such collimation was used, at the Tsukuba Photon Factory (Tanno *et al.,* 2006), where a monochromatic 5.35 keV beam was collimated down to a size of less than 10 μm and provided an irradiation dose rate of 0.3 Gy/s, corresponding to a collimated beam intensity of about 10^4 photons per second per unit area into focal spot. The Tsukuba beam line used for radiobiology experiments is able to

collimate X-ray beams of energy 4-20 keV to sizes of about 5 μm. The absorption of soft X-rays (278 eV) produces very low energy electrons within the irradiated sample. The short range of secondary electrons (~7 – 500 nm) will allow a critical analysis of the distances involved in radiobiological mechanisms. Some theories explain radiobiological effects in term of energy deposition within "sensitive sites" whose sizes vary from relatively large dimensions about 1 μm (Keller *et al.,* 1972) to vary small regions of a few nanometers in diameter (Chadwick and Leenhouts, 1973). While experimental work (Cox *et al.*, 1977) has shown that the sub cellular sites involved in inactivation and mutation are of the order of magnitude of a few tens of nanometers or less, other studies (Booz and Feinendered, 1988) seem to indicate that the whole of the cell nucleus must be considered as critical target. The photoelectrons produced by soft X-rays have a range compatible to the size of critical cellular structures and so are sufficiently short range that they can potentially be used to discriminate between different radiobiological models.

The major part of the work described in this thesis was directed at the development of a facility suitable for biological studies. Carbon K X-rays must be produced at a sufficiently high rate and the related high-energy bremsstrahlung radiation removed in order to obtain the quasi-monochromatic radiation necessary for high-resolution focusing.

1.3 Ionizing radiation and interactions with matter

Radiation exists with a continuum of energies and at low intensity below the multi-photon threshold only those with sufficient energy to break molecular bonds are of radiobiological consequence. This condition is typically met by particles and photons with energies greater than a few electron volts. Directly ionizing charged particles transfers energy through collisions and can include electrons, protons, and heavy ions. Neutrons like other neutral particles are indirectly ionizing as they do not interact electrostatically. Instead, depending on their kinetic energy, they either knock charged particles from a nucleus by sheer momentum transfer or, if moving more slowly, get captured by it. In the later case a nucleus can become unstable and subsequently undergo radioactive decay in order to reach a stable state. In so doing it releases energy in the form of charged particles or gamma rays and it is these secondary species, and those liberated kinetically, that actually give rise to ionization.

1.3.1 Ionizing photon interactions in biological materials

The process by which X-ray photons are absorbed depends on the energy of the photons concerned and the atomic and the chemical composition of the absorbing material. When X-ray photons interact with tissue, they give up energy by one of three process: the photoelectric effect, the Compton effect, or by pair production. All three of these interactions results in the production of energetic electrons that, in turn, lose energy by exciting and ionizing target atoms and molecules and setting more electrons in motion. If an X-ray beam is

absorbed by tissue, the net result is the production of a large number of fast electrons, many of which can ionize other atoms of the absorber and are sufficiently energetic to break chemical bonds.

Photoelectric absorption occurs when a strongly bound core electron with a binding energy, E_B, absorbs an incident photon of sufficient energy, $E = h\nu$, to cause its ejection from the atom. The kinetic energy, E_K, imparted to the ejected photoelectron is

$$E_K = h\nu - E_B \quad (1.1)$$

Left in an excited state, the atom relaxes when the vacancy in its inner shell is filled by a weakly bound electron failing into it from a higher orbit. In order to lose energy it gains in the transition the electron may emit a photon of energy equal to the difference in energy levels. This difference, and thus the wavelength of the photon, is characteristic to the atom. However, rather than being radiated away by the photon itself, this excess energy can be internally transferred to ionize another outer shell electron. Auger emission competes with photoemission and is dominant at low atomic numbers. Compton scattering occurs when an incident photon of energy, E, is scattered off of a loosely-bound, outer shell electron at an angle, θ, to the direction of travel. Because the electron is essentially free, its binding energy is negligible and thus the energy lost by the photon during the inelastic collision is almost exclusively imparted to the recoiling electron as kinetic energy (equation 1.2),

$$E_K \approx h\nu - \frac{E}{1 + \frac{E}{m_e c^2 (1 - \cos\theta)}} . \qquad (1.2)$$

Rayleigh scattering occurs when an incident photon of energy, *E,* is scattered at an angle, *θ,* off a core electron. Because the electron is strongly bound to the nucleus, the effective mass of the scatter is that of the atom it self. This being the case, the electron cannot recoil and thus the photon cannot lose energy in the collision. Photon energy can also be conserved if an incident wave energy, E, is Thomson scattered by a free electron. Here the electric field of the X-ray beam accelerates the electron, causing it to emit radiation at the same frequency as the incident wave. If a photon of sufficient energy, E > 1022 keV, interacts directly with the nucleus it can cause the spontaneous production of an electron-positron pair. Whilst the electron will lose energy through successive collisions with other electrons, upon meeting an electron the positron will be annihilated and two 511 keV gamma rays are emitted.

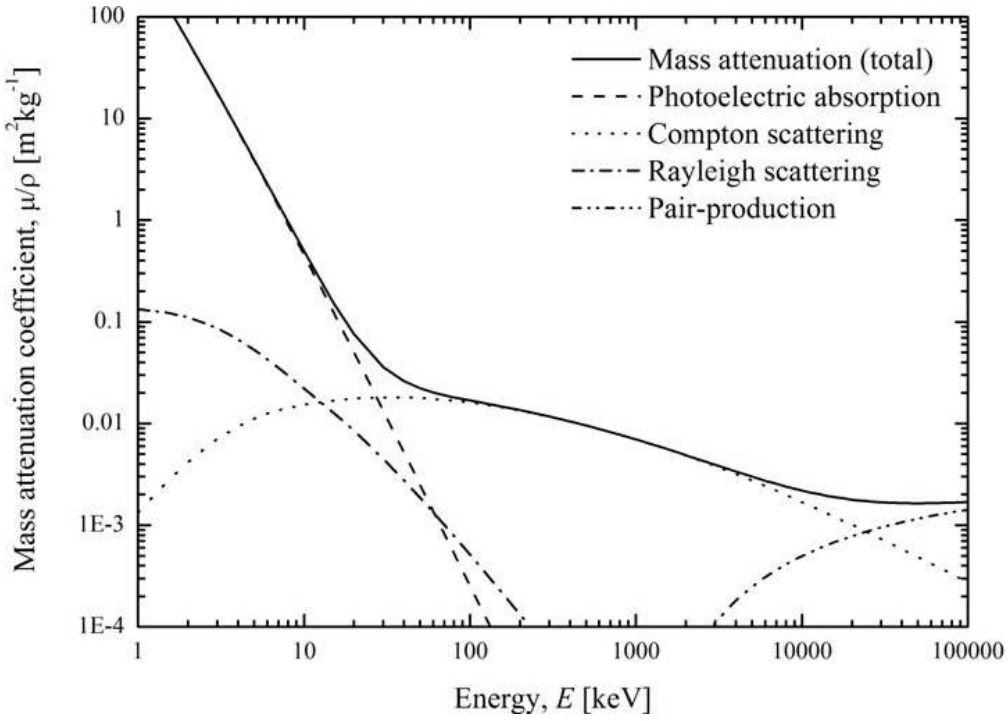

Figure 1.1 *Ionizing photon interactions in ICRU four component soft tissue (ICRU, 1989).*

Figure 1.1 shows the mass attenuation coefficients in International Commission on Radiation Units (ICRU) four component soft tissue (ICRU, 1989) for four of the five interactions as functions of photon energy. The total attenuation is the sum of the absorption and scattering components. The photoelectric absorption is clearly the dominant interaction for soft X-rays. This is no longer the case above ~30 keV, a typical energy used in mammography, where the rapidly decreasing photoelectric cross section falls below that of the slowly-changing Compton scattering process. Compton scattering remains the dominant process until pair production comes into play. Rayleigh scattering, whilst shown, is not considered biologically relevant as no net transfer of energy occurs.

Rather than the photon itself, it is the photo- and Auger electrons emitted during photoelectric absorption that actually cause damage to matter as they slow down to sub-energies (< few eV) through successive electrostatic collisions with bound electrons. The average energy lost by an electron per unit path length due to ionizing collisions, and emission of radiation, is known as its stopping power, *S.* The collisional stopping power, S_{col}, of an energetic electron is usually calculated from the Bethe formula (Bethe, 1930, Bethe, 1932)

$$-\frac{dE}{dx} = \frac{1}{(4\pi\varepsilon_0)^2}\frac{4\pi e^4 z^2}{m_e v^2} NZ\left[\ln\frac{2m_e v^2}{I} - \ln\left(1-\frac{v^2}{c^2}\right) - \frac{v^2}{c^2}\right] = S_{col} \qquad (1.3)$$

where N and Z are the number density and atomic number of the absorber (the product NZ specifying the total number of bound electrons a particle can collide with), m_e the electron rest mass, e the unit electronic charge, ε_o the permittivity of free space, c the speed of light in a vacuum, v and z the velocity and ionization of the incident particle, and I, the mean excitation potential of the absorber. However, at low energies the Bethe formula becomes unreliable, as binding energy of atomic orbitals may be greater than the kinetic energies of incident electrons.

1.3.2 Linear energy transfer

According to the previous section, the stopping power of an electron in matter is the sum of its collisional and radiative stopping powers

$$S = S_{col} + S_{rad} . \tag{1.4}$$

Although this describes the energy lost per unit length by an incident electron along its path, if energy radiates away as it slows down, the actual energy it deposits directly into the medium will be less than *S*. For low energy electrons, such as those produced by photoelectric absorption of soft or ultra soft X-rays (energy ~ 278 eV), radiative losses in tissue are insignificant and thus the S_{rad} term will tend to zero. As no energy escapes the medium, the collisional stopping power, S_{col} , will equal the average energy, dE , deposited along a given track, dx. Expressed in keV μm^{-1} (Hall and Giaccia, 2006), this quantity is known as the linear energy transfer (LET)

$$LET = \frac{dE}{dx} . \tag{1.5}$$

For any given radiation type, LET will decrease with increasing kinetic energy, whilst for different types of radiation with equal kinetic energies, LET will generally increase with the charge to mass ratio. Although a good indicator of radiation quality, it must be remembered that LET is averaged over an entire

track. If this track was subdivided into *n* segments of equal length, the energy loss per segment could vary greatly.

High LET radiation, such as MeV protons and heavy ions are densely ionizing. They interact readily with primary electrons to form columns of closely-spaced ionization events along their track. Conversely, energetic X-rays and other low LET radiations are sparsely ionizing as the ionization events they produce are widely-spaced. Typically, an MeV proton will produce several hundred times more ionization events per unit distance than a 250 keV diagnostic X-ray (Folkard, 2005).

For less energetic X-rays, the probability of Compton scatter diminishes whilst that of photoelectric absorption increases strongly to become the only significant source of attenuation at soft and ultrasoft X-ray wavelengths. As the total attenuation at these energies is ~ $10^4 - 10^5$ times grater than at 250 keV, low energy X-rays only produce short tracks in tissue before being stopped and, as a consequence, will deposit their energy in much smaller volumes.

Their higher ionization densities mean that soft and ultrasoft X-rays have higher LET's than diagnostic X-rays and, if concentrated into sufficiently narrow breams, will be able to mimic the tracks produced by heavy charged particles due to the similar kinetic energies of their photo and Auger electrons

to the δ- rays (secondary electrons) ejected in collisions with primary ions (Michael *et al.,* 1996).

Soft and ultrasoft X-rays interact with atoms through photoelectric absorption, a process that results in the ejection of photoelectrons and, due to the prevalence of low-Z elements in tissue, the emission of Auger electrons. As soft tissue is approximately 70% water by mass, in addition to it being a principal constituent of biological molecules, oxygen is the main target for interactions with X-rays. When a soft X-ray of energy greater than 0.543 keV encounters an oxygen atom it has the greatest probability of being absorbed by an electron in its innermost shell, the K-shell. For 1.487 and 4.511 keV soft X-rays, this electron will be ejected with a kinetic energy of 0.955 or 3.977 keV, the difference between the photon and binding energies. In both instances the K-shell vacancy is then rapidly filled by an electron from the L-shell, the next and outermost shell, and the excess energy is lost through the emission of a 0.484 keV Auger electron. Although the energies of the irradiating X-rays differ, the energies of the Auger electrons are equal because the atomic orbitals are quantized. As 0.278 keV X-rays only have sufficient energy to cause the ejection of a photoelectron from the L-shell, as the oxygen atom picks up a free electron to fill its outermost shell vacancy, there is no higher shell from which an Auger electron can be emitted during its relaxation. High energy X-rays, which are Compton scattered by electrons in an atom's outer shell, can lose up to half their energy in a single collision but, as most scattering is confined to angles close to the forward direction, the energy loss in most collisions will be

in the keV range. For all ionizing radiation, the damage to matter is ultimately due to electrons released in primary ionizing events. These electrons, be they photoelectrons or Auger electrons, lose kinetic energy by causing the ionization or excitation of atomic electrons as they slow down. With an ionization threshold of ~20 eV in tissue (Goodhead and Nikjoo, 1989), the energy transferred to a secondary electron in such a collision can be up to half that of the primary electron, *E*. If they have sufficient energy, secondary electrons can themselves cause further ionization or excitation, the process repeating until ~E/20 eV events have occurred. A measure of ionization density, LET is intimately linked to the energy of the primary electron because it is this that constrains the range over which ionization events can take place.

1.3.3 Microdosimetry

Due to the varying of electron energy released in primary ionizing events, radiation of different types and energies will deposit their energy in a material with differing spatial distributions and on timescales of a order picosecond (Hill *et al*., 2002) or less (Smith, 2000). Whilst charged particles, and low-LET X-rays, lose their energy through a succession of ionizing events with varying degrees of separation, individual soft or ultrasoft X-rays are completely absorbed by atoms within which they interact and thus lose all of their energy at a single point in space – essentially not producing extended tracks at all. Centered at this point, the absorbed energy, which is transferred to the release of primary electrons, will be constrained within a spherical volume

of maximum radius, x, equal to the photoelectron range. This analysis neglects any contribution from short-range secondary electrons and relies on the fact that, originating from higher atomic orbits, Auger electrons will have a shorter range than photoelectrons. It also presupposes that primary electrons may not be emitted in the same direction or those subsequent radiative processes do not transport energy over long distances. Within this volume, the photoelectron of energy, E_p, will impart some energy, ε_i, to secondary electrons at $I \approx E_p/20$ eV interaction points (Goodhead and Nikjoo, 1989, Folkard, 2005). Similarly, if an Auger electron of energy, E_A, is emitted, it will impart some energy, ε_i, to secondary electrons at a further $I \approx E_A/20$ eV interaction points. The total energy deposited, ε, in the volume by primary electrons is therefore the sum of the imparted energies, ε_i, at all interaction points, i, (Smith, 2000)

$$\varepsilon = \sum_i \varepsilon_i \,. \tag{1.6}$$

In the discrete ionizing events, equation (1.6) will also hold true when primary electron tracks from many such events overlap within the same volume. This may be the case when a material is irradiated with a flux of X-rays or if it is traversed by high-LET particles. In both cases, primary and secondary electron tracks will not necessarily begun and end within the volume, and thus the energy deposited (equation 1.7) will be the net difference in the kinetic energies, dE_e, of electrons entering, or being ionized within, the volume, and those leaving it, dE_l. The last term in equation 1.7, dE_{rm}, which represents a

change in rest mass due to nuclear reactions, is only significant if the incident radiation is a neutron, or of a very high energy in the multi-MeV range.

$$\varepsilon = dE_e - dE_l - dE_{rm} \tag{1.7}$$

To quantify the amount of radiation deposited in a microscopic volume, the concept of specific energy imparted, z, is often used (Smith, 2000, Randers-Pehrson, 2002). Defined as the energy, ε, imparted to the mass, m, within a rest volume,

$$z = \frac{\varepsilon}{m} \tag{1.8}$$

is a stochastic quantity that can only be determined through a series of experiments or simulations. Absorbed dose, whilst analogous to the specific energy imparted, is simply used to describe how much radiation is deposited in a non-defined volume. Commonly used in macrodosimetry, absorbed dose is defined as,

$$D = \frac{dE}{dm}. \tag{1.9}$$

The energy, dE, is deposited in a unit mass, dm, and is usually expressed in Grays where 1 Gy = 1 J kg^{-1}. Whilst it may appear that specific energy imparted and absorbed dose can be directly compared, problems can arise when doses are very low. To explain this, consider a block of tissue of mass, m,

irradiated with a single soft X-ray photon of energy, E. If the photon was absorbed in the block, the dose to the block would be E/m. However, if the block was in fact composed of n cells of equal size and mass, this would imply that each cell received an equal share, E/nm, of the dose. As soft X-rays interact with matter in discrete ionizing events, only one cell will be able to absorb the photon and thus, assuming all primary electron tracks are contained within the cell, $n - 1$ cells will receive no dose. This being the case, the dose to the cell cannot be ascertained from the dose to the block unless the size and mass of the block tend towards those of the cell, or the incident X-ray flux was to become very much larger. To account for this discrepancy, Booz (1978) introduced the concept of 'mean specific energy in affected volumes' where dose is only averaged over volumes in which energy has actually been imparted. In the example given the mean specific energy to the cell will thus be greater than that given to the block instead of the other way round. Randers-Pehrson (2002) renamed this parameter 'specific dose' and began to apply it to specific targets, such as the nuclei of biological cells, rather than specific volumes. Whilst this reinterpretation is, strictly-speaking, less accurate because biological targets of the same type may in fact have different volumes, describing radiation exposure in terms of, say, the specific dose to the nucleus or to the cytoplasm, allows the biological effects of different types of radiation to be directly compared.

Following the receipt of equal doses of different radiations, the magnitude of a given biological effect in a specific type of biological target is not usually the same. A function of its LET, and thus the spatial distribution of deposited energy, the ability of a given radiation to produce a given biological effect is known as its "effectiveness". As biological effectiveness can be expressed in many different ways it is usually expressed relative to that of 250 keV X-rays (Hall and Giaccia, 2006) and is thus termed the relative biological effectiveness (RBE). Essentially a radiation weighting factor, RBE's, *w*, for a range of radiations are shown in table 1.1 (Alpen, 1998).

Radiation type	*w*
X-rays, γ-rays, electrons, positrons, muons	1
Neutrons <0.01 MeV	5
Neutrons 0.01 - 0.1 MeV	10
Neutrons 0.1 - 2 MeV	20
Neutrons 2 - 20 MeV	10
Neutrons >20 MeV	5
Protons	2 -5

Table 1.1 *Radiation weighting factors for different types of radiation and different energies.*

As a result of their RBE, for different types of radiation to produce the equivalent biological effects, different absorbed doses, D, are necessary. Found by multiplying the absorbed dose by the RBE, the equivalent dose H is

$$H = wD. \tag{1.10}$$

Because RBE is has no units, although equivalent dose has the same unit as absorbed dose, in the context of causing a biological effect it is expressed in Sieverts rather than Grays, i.e. 1 Sv = 1 J kg^{-1}. Although table 1.1 states that X-rays have an RBE of 1, the RBE of X-rays has been found to increase with decreasing energy (Raju *et al*., 1987). This should be expected given that soft and ultrasoft X-rays have higher LET's than 250 keV X-rays and will therefore cause more localized damage. Whilst the RBE's of many biological endpoints have been measured for many different types of radiation, the most common is for biological cell killing. Cell killing RBE's of ~3 (Thacker *et al*., 1986) and 2.18 (Prise *et al*., 1989) have been found relative to 250 keV X-rays for 0.278 keV and 1.487 keV X-rays, respectively. Relative to MeV gamma rays, De Lara *et al.* (2001) found that 0.278 keV X-rays yielded an RBE of 2.8, similar to that of Thacker *et al.* (1986), whilst 4.511 keV X-rays yielded an RBE of 1.5. These three X-ray wavelengths are thus capable of producing a spectrum of biological damage that ranges from that produced by high-LET protons to that produced by low-LET X-rays.

1.4 Radiobiology of ultra-soft X-rays

1.4.1 History of ultra-soft X-rays in radiobiology

The beginning of radiobiology studies using ultrasoft X-rays has to be attributed to Lea (1941) towards the end of the first half of the 21st century. Previous studies using X-rays of 7.1 keV and 5.4 keV were used to investigate sex-linked lethal mutation in *drosophilia* (Timofeeff-Ressovsky, 1934; Gowen *et al*., 1933). The first ultrasoft studies using X-rays of 1.5 keV and 3 keV were performed by Lea and Smith and shown to inactivate plant viruses (Lea and Smith, 1942a). Lea used a cold cathode tube with copper, silver and aluminium transmission targets to produce characteristic X-rays of 8.26 keV, 2.99 keV and 1.49 keV respectively. The potential applied to the tube varied from 3 kV to 40 kV and the emission rate was controlled adjusting the pressure in the tube achieving a maximum output rate of 8×10^3 photons s^{-1} with a 20 μm thick aluminium target and 1.5×10^3 photons s^{-1} with a 66 μm copper target (Lea, 1941). Those first experiments were directed to investigate the formation of chromatid aberrations in the pollen of Tradescantia bracteata (Lea and Catcheside, 1942b; Catcheside and Lea, 1943). Improvements were made some years later by Neary when experiments were followed by statistical analysis and dosimetric considerations (Neary *et al.,* 1964; Neary *et al.,* 1967). He used a cylindrical air proportional chamber (0.8 cm diameter) to calibrate the dose delivered to the targets and a parallel-plate ionisation chamber normal to the X-ray beam to monitor the individual exposures. Practical difficulties due to the short range of the radiation used made the experiments less than ideal as Neary himself acknowledged, and big variations in the dose delivered to the pollen

were caused by additional absorbing materials such as overlaying pollen or water. Data using magnesium K-line X-rays (1.26 keV) were also included in Lea's work. These experiments pointed out that ultrasoft X-rays, once thought to be completely ineffective, were actually very effective in producing chromatid aberrations. Moreover, the good efficiency of aluminium X-rays causing for such radiobiological damage supported the hypothesis that the whole chromatid diameter could no longer be identified with the critical size in the target mechanism of aberration induction. The acceptance of such hypotheses opened the way for a simpler interpretation of the induction of aberrations by radiation. Primary lesions in chromosomes may be produced by one energy-loss event of 60 eV in a volume of the order of few cubic nanometers rather than by a combined action of a few tens of events in 0.1 μm structures as postulated previously by Lea and Catcheside (1942b).

Considerable improvement and new insight for the use of ultrasoft X-rays in radiobiology comes from Goodhead and co-workers. They extended the studies to mammalian cells, including hamster V79 and human HF19, and to lymphocyte cells (Cox *et al.,* 1977; Goodhead and Thacker, 1977a; Goodhead, 1977b; Godhead *et al*., 1979; Thacker *et al.,* 1986; Virsik *et al.,* 1980). A wide spectrum of endpoints was investigated, from inactivation to mutation and chromosome aberration. Their work used carbon K X-ray (0.278 keV) for the first time. Radiation with such a localised energy deposition was particularly appropriate at the time because of the conflict between different models attempting to describe the effects of ionizing radiations on living organisms.

The ultrasoft X-ray studies provided evidence contrary to the theory of dual action radiation that explained radiation damage in terms of deposition of energy in a relatively large "sensitive site" (about 1 μm). As a consequence other hypotheses were formulated that suggested that the critical target is a few nanometers in diameter. The experiments confirmed the previous findings regarding the effectiveness of ultrasoft X-rays and the size of sub-cellular sites involved in inactivation and mutation. Goodhead *et al.* (1979) concluded that the critical distances involved must be smaller than 7 nm and that independent, very localised energy depositions are sufficient to produce significant damage. These results, and subsequent data (Brenner *et al.,* 1987; Raju *et al.,* 1987) lead to the conclusion that the RBE increases with decreasing X-ray energy, and therefore photoelectron track length. Thacker *et al.,* (1986) reported a RBE of 3 for cell killing by carbon K X-rays relative to hard X-rays and of 2 for aberration induction in V79 cells pointing out how the low-energy electron track-ends contribute ≥ 30 % of the total dose and are the main cause of damage in all low-LET radiation. The observed effective linear component of induction of chromosome exchanges by ultrasoft carbon K X-rays led Thacker to an interesting conclusion. Because the energy deposition is within 7 nm and this distance scarcely allows more than one part of the chromosome to be involved in the irradiation, it raises the hypothesis that only one chromosome needs to be damaged by radiation to cause an exchange event.

The rapid improvement of track structure theory and microdosimetric techniques (Paretzke, 1987; Goodhead, 1987) made possible

Monte Carlo simulations for different types of radiation incident on a variety of targets (Wilson and Paretzke, 1981; Charlton *et al.,* 1985; Booz and Feinendegen, 1988). Mass absorption coefficients for ultrasoft X-rays in mammalian cells were calculated in order to better delineate the spectrum and the pattern of energy deposition. Nikjoo *et al.* (1989) reported that oxygen is responsible for 80 – 90% of the interactions in soft tissues while in DNA nearly 50% of the carbon K ultrasoft X-rays interact with phosphorous. Calculations of the absolute frequency of energy deposition in small targets of the size of DNA structures explained the high radiobiological effectiveness of low-energy photons.

The relative biological effectiveness of ultrasoft X-rays compared with hard X-rays has been found to be considerably higher than 1 for most of the effects studied including cell inactivation, mutation, chromosome exchange and DNA double strand break. Substantially smaller RBE values have been reported for the inactivation of some cell lines. An RBE of ~1.4 has been calculated for 10T1/2 mouse cells (Schillaci *et al*., 1988) and for AG1522 human fibroblasts (Cornforth *et al*., 1988). These discrepancies may be explained by differences in cell line radiosensitivity and in cell thickness. The sensitivity may be related to different sensitive targets or, more likely, to different repair efficiency. The cell thickness must be carefully considered when ultrasoft X-rays are used due to the high-attenuation coefficient. When attached, V79 cells are significantly thicker than 10T1/2 cells (Bettega *et al.,* 1998) so that for carbon X-rays, the dose absorbed in the mid-plane of a thicker

cell would be considerably less than that absorbed by the mid-plane of the thinner cell. These results underline the importance of the distribution of the sensitive sites inside the cell nucleus and in establishing an appropriate cell depth of the biological targets at which to specify the absorbed dose to the cell. Other investigations (Carpenter *et al.,* 1989) have shown how the RBE determinations for ultrasoft X-rays are influenced by the cell shape and thickness rather than by the biological variation of the various cell lines. An alternate approach to avoid the variation of biological factors was suggested by Meger *et al.* (1991). Using synchrotron radiation, it is possible to select X-rays with different energies that have the same attenuation coefficient resolving inconsistencies in the data between lines. Irradiating the same cell line with X-rays of different energies but having similar attenuation coefficients in tissues, it will be possible to investigate the effect due to the photoelectron energy. Herve du Penhoat (Herve du Penhoat *et al.,*1999) reported a 2 fold enhancement of lethality for 340 kV X-rays compared to 250 kV. This increase was attributed to a specific lethal effect of carbon K-shell ionisation in DNA. On the other hand, irradiating the samples with X-rays of similar energy but characterized by quite different attenuation coefficients (as occurs near absorption edges), the effect due to differences in dose absorbed through a cell can be isolated. These studies are still under investigation. In some studies, the induction of single and double strand breaks in Chinese hamster V79 cells irradiated with ultrasoft X-rays has been investigated under aerobic and anaerobic conditions. RBEs for dsb (double strand break) induction of 2.5 for aluminium X-rays (1.487 keV) and 3 for copper X-rays (8.06 keV) were

determined (Botchway *et al.,* 1997) using the technique of pulsed gel electrophoresis. Oxygen enhancement ratio values of 1.9 for inactivation and 2.1 for dsb production were obtained for aluminium X-rays. Botchway also stressed the importance of differences in cell morphology and attenuation of ultrasoft X-rays through the cell nucleus. The discrepancies in the RBE value for induction of double strand breaks by aluminium K X-rays reported by Prise *et al.* (1989) were minimized when a conversion factor of 0.45 (fraction of dose deposited in the cytoplasm) was used to convert surface dose to nuclear dose absorbed in the nucleus. Improvements in electron microscopy and the use of confocal microscopes have given new insight in to the investigation of the spatial organization of the nucleus. Griffin *et al.* (1996) calculated that, for an average dose of 1 Gy of aluminium X-rays, the first-micron slice receives 0.96 Gy against the 0.56 Gy of the subsequent 5 micrometer slice. Therefore, the high frequency of complex exchanges detected after ultrasoft X-ray irradiation has been correlated to the higher dose delivered to the DNA in close contact with the nuclear membrane. This is in agreement with the concept that active genes are located close to the nuclear membrane.

1.4.2 Importance of ultra-soft X-rays in radiobiology

Ultrasoft X-rays are of special importance for mechanistic studies of ionizing radiation damage in living cells due to the localised nature of their energy deposition. For photons of energy lower than 5 keV (ultrasoft X-rays), the photoelectric effect is the main method of interaction with biological tissues; the contribution of Compton scattering is less than 0.1% (Nikjoo *et al.,*

1989). The dominant interaction in tissue is with oxygen atoms and this leads to the production of photoelectrons of low energy (250 eV for carbon X-rays and 950 eV for aluminium X-rays). In the case of carbon X-ray (278 eV) irradiation, photoelectrons are the only secondary species produced. For higher-energy ultrasoft X-rays Auger electrons are also generated inside the target (~ 500 eV Auger electron energy after aluminium X-ray irradiation). The secondary electron tracks generated by the absorption of a photon are very limited in range, releasing their energy in a few nanometers (average electron range of 7 nm for 278 eV carbon K X-rays and 70 nm for 1.5 keV Aluminium K X-rays). These ranges are comparable to the sizes of critical sub-structures in the cell nucleus such as DNA strands (double helix) (~ 2 nm), nucleosomes (~ 10 nm) and chromatin fibers (~ 25 nm). Low-energy photons can thus be used to investigate the size of sensitive sites within the cell nucleus and the critical distances associated with lesions produced by radiation. Moreover, because of the high LET of the secondary electrons produced, ultrasoft X-rays represent an ideal tool to address the consequences of clusters of damage to the DNA. It has been calculated (Nikjoo *et al.,* 1989) that a single carbon K X-ray (278 eV) is responsible for about 26 interactions (ionizations and excitations) in a volume comparable to the DNA double helix while an aluminium photon (1.487 keV) generates about 150 interactions over a much larger volume. Considering an energy deposition of $E \geq 100$ eV, Goodhead and Nikjoo (1989a) showed that such events occur in about 23 DNA segments per cell following irradiation by 1 Gy of low-LET radiation, 47 segments with aluminium X-rays, 69 with carbon X-rays and 94 with 3 MeV α-particles. Such

energy deposition is believed to create substantial molecular damage to the DNA. The sensitivity and role of complex multi-site damage to the DNA are still under investigation and the resolution offered by ultrasoft X-rays can potentially supply substantial data and information to advance the understanding of the mechanisms of radiobiological action.

1.5 Microbeams in radiobiology

Micro-irradiation techniques have been recognized as a powerful tool for investigating the interaction of radiation with biological matter. The main characteristic of all microbeam facilities is the ability to deliver a pre-selected dose of ionizing radiation to a small target of biological relevance. It is possible to classify the microbeams into two categories: those using a collimated approach and those focusing the incident radiation. Each method has limitations but also advantages that make it suitable for particular applications.

The focusing method is particularly appropriate for certain types of electromagnetic radiation where optical elements can be used to focus or diffract radiation of a determined wavelength. The use of transmission optics will however introduce distortions and aberrations in the exit beam due to scatter, absorption and internal reflection. A further problem arises from absorption in air. High-resolution focusing is obtained under vacuum conditions, unacceptable for most of the biological samples unless mounted in a windowed wet-cell within the vacuum chamber housing the source and

focusing optics. Therefore, scatter by the air gap that separates the focusing device from the samples will degrade the size of the focus. As a consequence, the sample position is critical and there will inevitably be part of the sample irradiated with different intensity from the "hot-spot". Focusing apparatus for charged particles present additional problems like the alignment of the focusing magnets and the difficulties in obtaining a low-flux beam necessary for radiobiological purposes.

1.5.1 Charged-particle microbeams

The first charged-particle microbeam was designed by Zirkle and Bloom in 1953. Collimators were used to reduce to micrometer size a broad beam of 2 MeV protons produced by a Van de Graaff accelerator. Alpha-particle microbeam systems are in principle similar to Zirkle's proton microbeam. A great advantage was the use of alpha particle laboratory sources that avoided the problems and the expenses associated with particle accelerators. The most common method for the production of collimators was to manufacture a hole in a solid thin metal sheet. A valid example is the collimator used by Kuzin and Wainson (1966) to investigate the effects of α-particle irradiation on the synthesis of DNA in HeLa cells. Limitations in the particle detection remained and further complications were due to long irradiation times required because of the low flux of transmitted particles.

1.5.2 Laser microbeams

The development of sources capable of generating high-intensity monochromatic radiation benefited the development of micro-irradiation techniques. The higher-power and shorter-wavelength sources were possible to design with laser microbeams, more suitable to investigating radiation damage in biological systems. Moreno and Salet (1985) investigated the photosensitivity of various parts of single cell using a 1 mW HeNe laser (λ = 632.8 nm). Laser microbeams are still widely used for cell manipulation and gene deletion applications (Berns *et al.,* 1991).

1.5.3 Ultraviolet microbeams

The first microbeam was developed by Tschachotin in 1912. In this apparatus, the ultraviolet light (250 nm) produced by a mercury lamp was used to illuminate a pair of adjustable slits. The light passing through the slits was then used as object by a quartz microscope objective to produce a hot-spot of a few microns in diameter. The cells were plated on a 5 μm thick mica sheet and viewed under visible light.

This original design was improved by Perry, Uretz and Bloom (Perry, 1956; Uretz *et al.*, 1954). The slit was substituted by a 100 μm diameter pinhole that could be demagnified through a microscope object to produce a 2 μm diameter spot. A further improvement was the use of the same optics for both UV irradiation and visible light illumination. This allowed accurate positioning of the targets in the focus position. In both facilities, the cells were

viewed at and after the irradiation with high mechanical precision. The first relevant biological experiments (Shimomura et al., 1967) were directed at investigating the functions of cellular organelles in grasshoppers, newts and HeLa cells.

1.6 Modern microbeam facilities

The first single-cell micro-irradiation facility of the modern microbeam era was developed at the Pacific Northwest Laboratory (Braby and Reece, 1990). A 2 MV tandem accelerator was used to produce a hydrogen or helium-ion beam that was subsequently bent 90^{o} as to have a vertical upward beam. This facilitate the irradiation procedure as the samples could be in their normal tissue culture conditions during the experiment. The collimation system relies on a 30 μm thick sheet of mica on which holes between 0.7 μm and 2.0 μm in diameter have been produced (Braby, 1992). The holes are produced by exposing the mica to a low dose of high-energy ions and then removing the damaged material by chemical etch. As the holes are randomly distributed across the mica sheet, a precollimator (i.e. a capillary tube) has to be used to confine the beam to a determined hole. The detection method basically consists of detecting the light flashes produced by the ions in crossing a thin plastic scintillator (~ 10 μm) placed between the collimator and the samples. The scintillator also acts as vacuum window. The photons emitted by the scintillator as the ions pass through are detected by a small photo-multiplier tube (2.5 cm in diameter) mounted to the microscope lens turret. A servo system automatically rotates the turret to position the objective or the PM tube

over the collimator to visualize the samples or count the particles delivered. The PM tube output is connected to a fast piezoelectric shutter (0.1 ms) that controls the sample irradiation.

The Colombia University microbeam uses a 4.2 MV Van de Graaff accelerator to produce beams of protons, deuterons, helium-3 nuclei and α-particles for a range of LET from 20 to 225 keV μm^{-1}. The collimation system consist of two stainless steel foils (500 μm thick) with central laser drilled holes of 5 μm and 6 μm respectively (Randers-Pehrson et al., 1993; Randers-Pehrson,1994). The two holes are separated by a gap of 300 μm and aligned using a laser beam and light microscope. High-energy resolution is achieved as shown by the energy spectrum where 90% of α-particles emitted are within the full energy peak. The overall spatial resolution claimed is 5 μm in diameter. An epi-fluorescence microscope and fluorescence stains are used to locate cellular targets while a micropositioning stage assures target-beam alignment. The system operates under computer control and allows the irradiation of up to about 12×10^3 cells per hour (Randers-Pehrson et al., 1999). The detection system is based on a transparent gas filled proportional chamber located above the cell dish. This requires the incident particles to have enough energy to completely traverse the cells and the extra layer of culture medium in order to be detected by the proportional counter. The detector is built in the microscope objective so that the cells can still be viewed during the irradiation phase.

Another microbeam facility currently used for radiobiological studies is that in operation at Queen's University, Belfast. This facility contain variable target materials (aluminium and titanium) (Schettino *et al.,*2003a), and using zone plates optimized for resulting 1.487 keV and 4.511 keV characteristic radiation, respective X-ray fluxes of 4×10^3 and 1×10^2 photons per second could be delivered to cellular targets (Schettino *et al.,*2003b).

1.7 Microbeams for non radiobiological studies

The ability to produce a very fine beam of ionizing radiation represents also a powerful tool in scientific fields other than radiobiology. This was recognized since the early 1950's with Zirkle and Bloom (1953) and a few years later there were two laboratories (Pierece et al., 1966; Mak et al., 1966) that were using collimated beams of few hundreds microns for nuclear reactions. However, the need of brighter beams promoted the use of quadrupole lenses as a replacement for low efficiency collimators. Improvements in the physics and design aspect of electromagnetic lenses gave new insight in the investigations of microbeams. Considerable benefit came also from the development of Si(Li) detectors and the use of computers that allowed researchers to collect and analyze large amounts of data in relatively short times. By the end of the 1970's there were more than 5 scanning ion microscopes around the world aiming at a resolution of 1 μm (Watt, 1982). Today, there are several microprobes operating both in high (~ 1nA) and low current (~ 1 fA) mode with a resolution of a fraction of a micron.

Recent improvement in nuclear microprobe technology allows the achievement of spatial resolution at the 100 nm level using high-energy ions. A common method to focus high-energy ions into a spot of submicron size is using magnetic or electrostatic quadrupole lenses. Electric and magnetic fields can be arranged to control the flow of ions in the same way optical lenses control the propagation of light.

1.7.1 X-ray microbeam

Soft X-rays are easily attenuated by anything with which they interact; the use of diffractive optics is therefore preferred to refractive systems in order to obtain high resolution focusing. The most commonly used diffractive lenses are Fresnel zone plates. These are circular diffraction gratings with a spatial resolution limited to the width of the finest, outermost zones. Today most zone plates are made by electron beam lithography and can be manufactured with finest zone widths as narrow as 30 nm allowing one to potentially focus the X-ray beam in a few tens of nanometers spot. As a result the numerical aperture of the zone plates is generally less than 0.1, which implies a depth of field in the range of a few micrometers. The use of monochromators, wigglers and undulators in synchrotron facilities provides X-ray beams, which are both tuneable in energy and well collimated. Their time-averaged brightness is about 10^{10} times that of the laboratory sources available just few decades ago. This allows the use of zone plates to obtain focused X-ray beams providing a considerably higher dose rate which are suitable for a range of application.

The main application of soft X-ray microbeams is in the microscopy field. Soft X-ray microscopy offers a set of characteristics in between those of visible light and electron microscopy. The wavelength (~ 10 nm) is much smaller than that of visible light, giving the potential for high spatial resolution imaging. In visible light microscopy, lenses with high numerical aperture are limited by a wavelength-limited resolution. In X-ray microscopy, using diffractive optics (Fresnel zone plates) the Rayleigh resolution is limited to 1.22 times the width of the narrowest zone. Moreover, the photon energy is well matched to inner shell electron energies in the low atomic number elements. In particular, by operating between the K edges of carbon (~290 eV) and oxygen (~540 eV) (so called "water window"), it is possible to obtain intrinsic contrast between organic material and water and good penetration in micrometer thick specimens. This allows spectroscopic mapping of the biochemical elements present in cells and tissues with high spatial resolution and sensitivity.

Soft X-ray microscopes can be basically divided in two main categories: transmission and scanning X-ray microscopes. Transmission X-ray microscopes imitate the design of conventional optical microscopes. Zone plates are used both as condensers to focus the X-ray beam on to the samples and as objectives to collect the X-ray from the sample and direct them towards a detector (usually a CCD camera). These microscopes are characterized by exposure times of a few seconds. Scanning microscopes usually use only one zone plate as a high resolution objective to focus the X-ray beam in to sub-

micron part of the samples. The sample (or in some occasions the X-ray beam) can be scanned to acquire information about the whole specimen. Scanning microscopes generally have exposure times of minutes but impart about 10 times less radiation damage to the specimen than transmission microscopes. A schematic illustration of the common configurations used for the soft X-ray transmission and scanning microscopes shown in figure 1.2. These microscopes need very bright sources (i.e., undulaors or storage rings) and are considerably more expensive to built and maintain although more affordable microscopes are being developed based on laser sources. The final resolution of these microscopes is a few tenths of a nanometer, still inferior to that offered by electron microscopes. However, there are a number of potential advantages in using a soft X-ray microscope. Specimens up to few tenths of microns thickness can be imaged. Moreover, the lack of inelastic scattering allows to achieve an energy resolution of ~ 0.2 eV for spectro-microscopy applications while plural inelastic scattering limit the resolution of electron microscopes to ~ 1 eV.

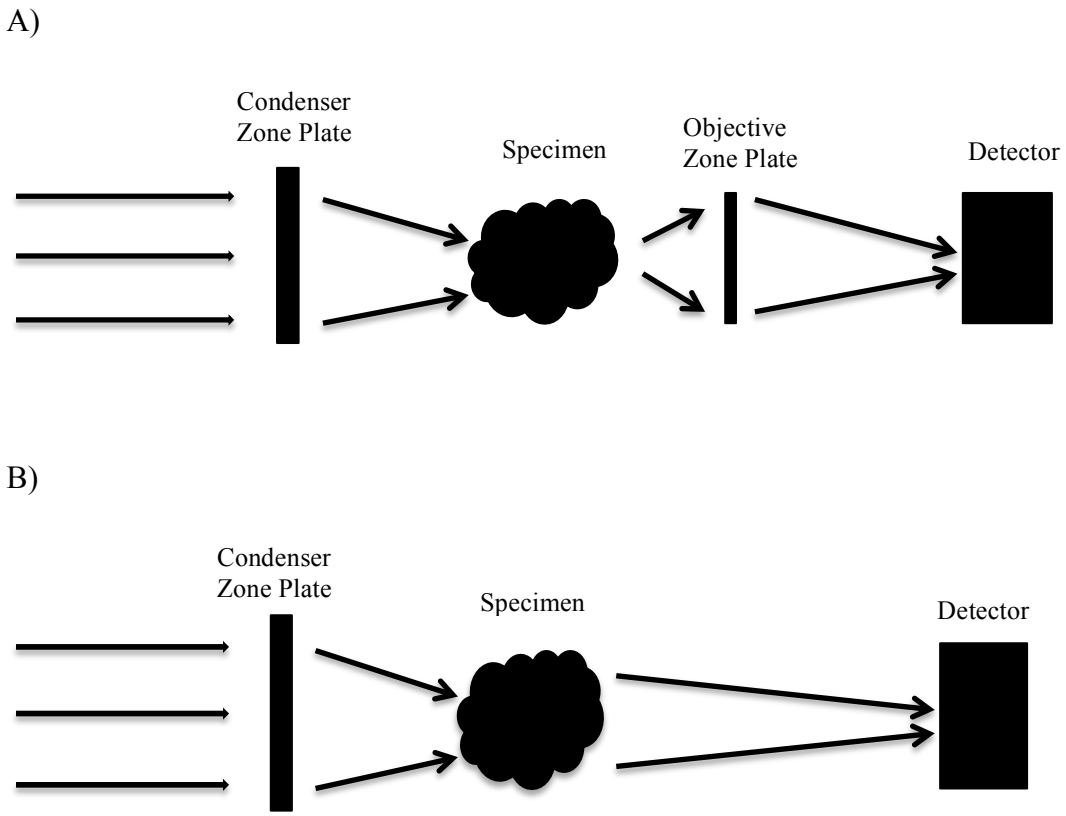

Figure 1.2. *Geometries used for X-ray microscopy. A) Transmission X-ray microscope (TXM). B) Scanning transmission X-ray microscope (STXM)*

Chapter 2

The re-instating of a microfocus X-ray source MK I for biological experiments

2.1 X-ray production

The region of the electromagnetic spectrum included in the wavelength range $\lambda \sim 0.01 - 10$ nm is ascribed to X-rays. X-rays are defined as photons of energy $E \sim 120$ eV – 120 keV, according to the quantum relation

$$E = h\,c\,/\,\lambda \qquad (2.1)$$

Where $h = 6.62618 \times 10^{-34}$ J s is Planck's constant and $c = 2.99792 \times 10^{8}$ m s^{-1} is the speed of light in a vacuum.

X-ray can be generated by two main processes. In the first, electrons in atomic or molecular orbits are excited or ejected (i.e., the photoelectric effect) and electrons from higher levels fill the resultant "vacancies". The energy gained is partly dissipated in thermal rearrangements and partly emitted as electromagnetic radiation whose energy depends on the properties of the particular atom. This type of process gives discrete line spectra (labeled with the letters K, L, M, …according to the quantum number of the vacant level filled) and is then called "characteristic radiation". The

second process involves the deceleration of charged particles (usually electrons) in the electric field of an atomic nucleus; the energy lost leads also to the emission of radiation. This radiation (called "bremsstrahlung") is continuous and covers a wide frequency range whose upper limit depends on the energy of the incident charged particle. Both of these processes may occur simultaneously producing an X-ray spectrum composed of characteristic and continuous photons.

The most common and relatively simple method to produce X-rays is to bombard a solid target with accelerated electrons. In this way, both characteristic X-rays and bremsstrahlung is produced. The initial event in characteristic X-ray production is the removal of an inner shell electron, and thus the minimum energy that must be supplied by the bombarding particle is the K-shell binding energy. Apart from this, the wavelength of the characteristic lines depends only on the target material as described by Moseley's law (Michette and Buckley, 1993a)

$$\lambda \sim 1.212 \times 10^{-7} / (Z - 1)^2 \qquad (2.2)$$

where Z is the atomic number of the target material. Unlike characteristic X-rays, the bremsstrahlung spectrum has only a small dependence on the nature of the target, but other factors such as the energy of the incident particle and the internal and external filtering are dominant. Since characteristic X-rays are emitted in a secondary-transition process, there is no angular correlation

between the direction of the incident particles and that of the emitted photons. Characteristic X-rays are then emitted isotropically (neglecting attenuation by the target). Bremsstrahlung on the other hand, is emitted anisotropically, tending to go more in the electron direction with increasing electron energy. This angular dependence plays a strong role in thin targets and at high electron energies but becomes much less pronounced for thick targets and low electron energies (Motz *et al.,* 1971). Summerfield's theory for the spatial distribution of the continuous X-rays leads to the following formula

$$I(\Theta) = \frac{e^2 a \sin^2 \Theta}{16\pi c^2 r^2 \cos\Theta}\left(\frac{1}{(1-\beta\cos\Theta)^4} - 1\right) \qquad (2.3)$$

where $I(\Theta)$ is the intensity of X-rays emitted as a function of the angle Θ between the incident particles direction and the emitted X-rays. r is the distance from the X-ray source at which the detector placed, c is the speed of light, e the electron charge, a the deceleration of the particle and $\beta = v/c$. This theory based on classical considerations, predicts results that are in remarkable agreement with the experimental measurements (Agarwal, 1991).

The semi-classical theory developed by Kramer (1923), leads to a flat radiant energy spectrum as a function of the photon energy for particles incident on thin targets up to maximum photon energy equal to the energy of the incident electrons.

The resulted formula (Kramer's spectrum) predicts a liner decrease of the number of bremsstrahlung produced as a function of their energy according to the formula

$$R(h\nu) = CN_e Z(h\nu_{\max} - h\nu) \tag{2.4}$$

where R is the differential energy distribution of bremsstrahlung generated in the thick target of atomic number Z, N_e indicates the number of electrons incident on the target and $h\nu$ is the photon energy. The maximum energy expected for the continuous X-rays ($h\nu_{max}$) is equal to the total kinetic energy of the incident electrons. When R and $h\nu$ are expressed in MeV, the constant C has a value of 2×10^{-3} MeV^{-1}. The main phenomena not considered by the formula (2.4) are electron back-scattering from the target, energy lost by the electrons in entering the target and X-ray absorption by the target itself. The energy of the incident electrons mostly goes to heating the target, except for a very small fraction emitted as X-rays. The conversion efficiency (ε) of incident electron kinetic energy into continuum bremsstrahlung X-rays is expressed by the empirical formula (Compton and Allison, 1951)

$$\varepsilon = 1.1 \times 10^{-9} ZV \tag{2.5}$$

where Z is the atomic number of the target and V is the voltage through which the electrons are accelerated. Thus, even with heavy targets (e.g., tungsten, Z =

74) and high voltages (V = 100 kV) very poor efficiencies are obtained (ε = 0.8%).

2.2 The microprobe ultra-soft X-ray source

The ultrasoft X-ray source used for this project was initially built for X-ray microscopy purposes by the National Physical Laboratory (UK). The source was installed at King's College London (KCL) during 2008. It was used to study the optical characterization of Micro-Structured Optical Arrays (MOAs) during 2011. After the study of MOAs, the source was reinstated to study radiation effects on biological targets at subcellular levels. The microfocus source used for MOA studies at KCL is shown in figure 2.1.

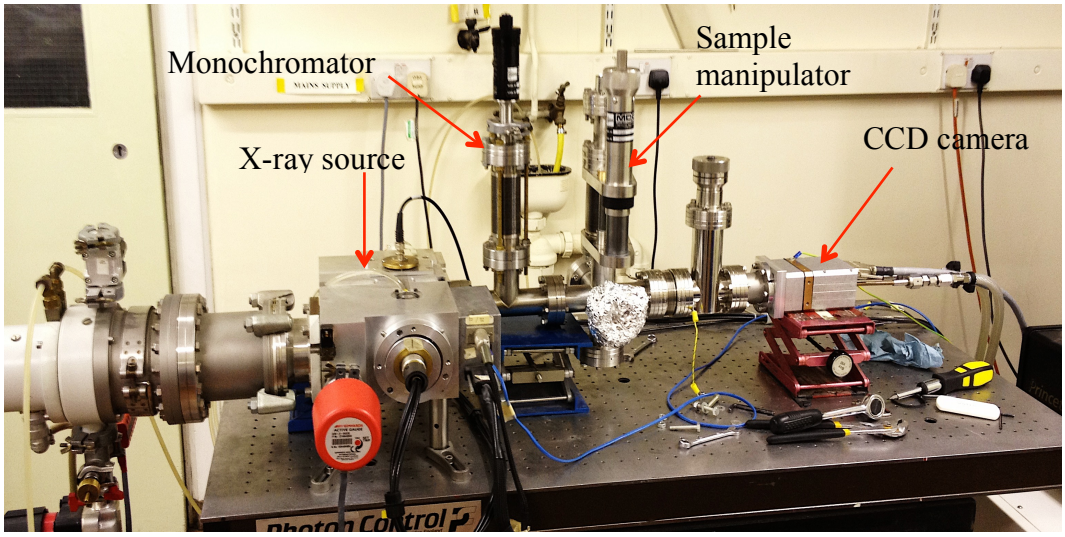

Figure 2.1. *The microfocus soft X-ray source configured for optical testing. X-rays emitted by the source pass through the monochromator and sample manipulator on towards the CCD camera.*

2.3 The re-instating of a microfocus X-ray source

Initial optical characterization of MOAs experiments was performed without an X-ray monochromator. The monochromator was developed to monochromatize the X-ray beam and experiments of multilayer mirrors. A micrometer, with a 180 mm long rod, was used to adjust the angle of the stage. A sample could be placed behind the focusing components on a stage, which would allow movement in two directions perpendicular to the X-ray beam to realise imaging by raster-like scanning. Figure 2.2 shows the structure of the monochromator manipulator used for MOAs and the characterization of multilayer mirrors.

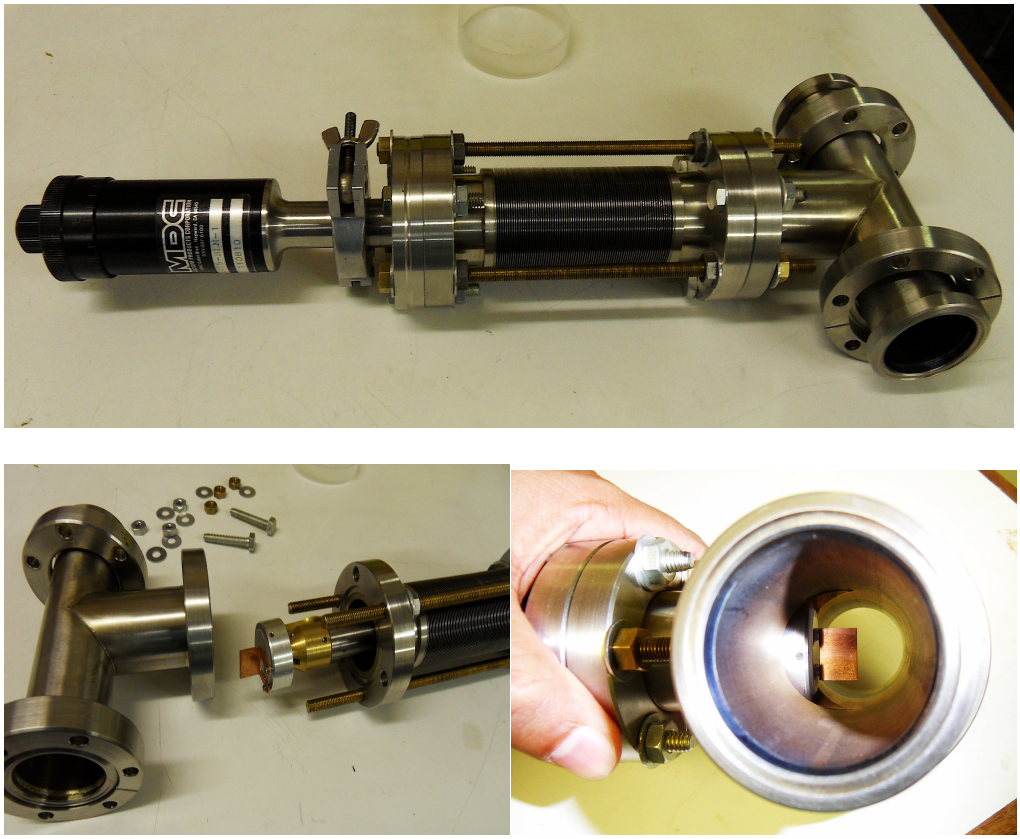

Figure 2.2. *The monochromator and structure of the mirror holder.*

The microprobe ultrasoft X-ray source was reinstated by changing several components. For this reinstatement process the electro magnetic lens, X-ray source power supply, orientation of the source and monochromator manipulator were redesigned, and a summary will now follow.

The schematic diagram of the X-ray source was shown in figure 2.3. After reinstatement the microfocus source is capable of producing small (~ 200 μm) size spots of electrons on the surface of a target.

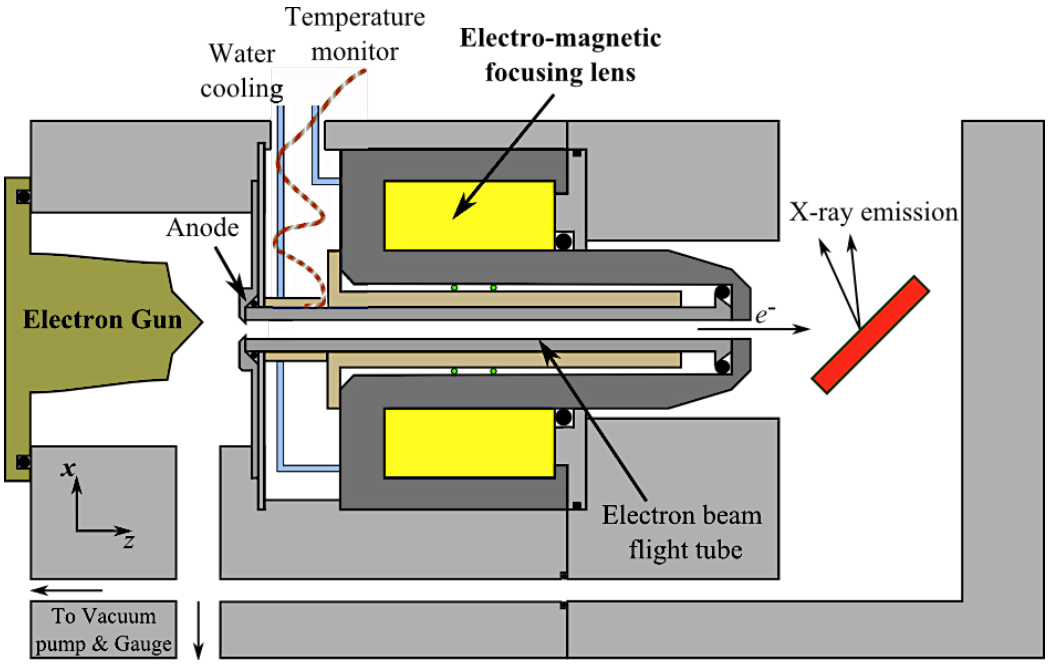

Figure 2.3. *Schematic illustration of the microprobe X-ray source.*

The source provides characteristic X-rays by the action of accelerated electrons striking a solid carbon target.

The body of the source is made of two solid aluminium blocks; one houses the electron gun while the target is located in the second block from the top of which the carbon K X-rays emerge. The two blocks are connected by an electro-magnetic lens that focus the electron beam generated by the electron gun on to the target. The source is evacuated using a turbo-molecular pump to about 10^{-5} – 10^{-6} torr. Such a vacuum inside the source is necessary in order to avoid the electrons and X-rays being absorbed by the air. A vacuum interlock system, controlled by an Edwards 2002 controller, allows the electron gun to be energized only when satisfactory vacuum conditions are reached.

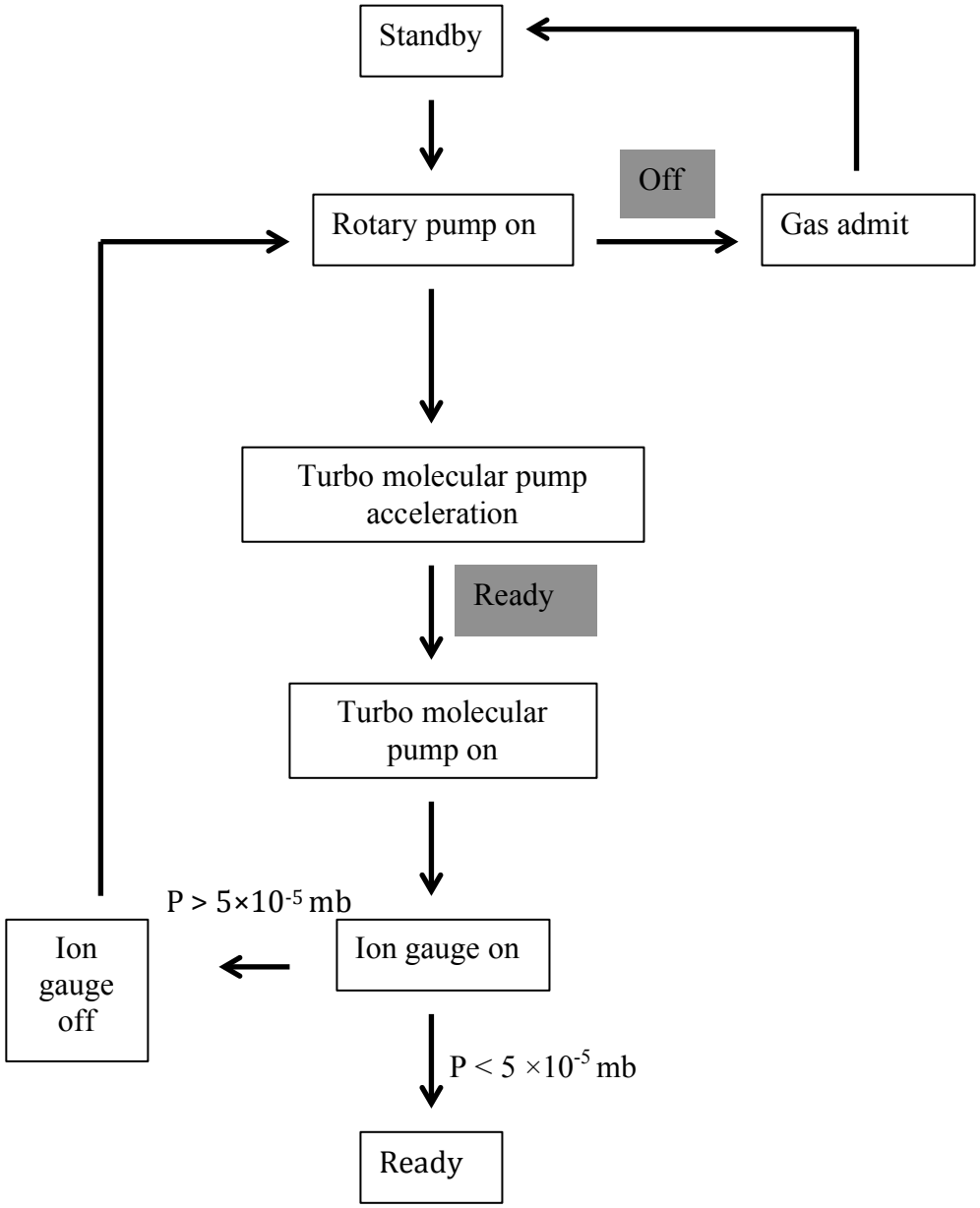

Figure 2.4. *Flow chart sequence for the microprobe source vacuum interlock (Controller: Edwards 2002). Highlighted boxes indicate switches pressed by the operator.*

The electrons are produced by a heated tungsten filament (Agar Scientific Ltd) through which runs a 2 – 4 A current. The filament is mounted in the electron gun consisting of a ceramic body to electrically isolate the filament from the

rest of the source. In order to achieve good alignment between the filament and the electromagnetic lens, two screws enable the electron gun to be moved accurately even when the source is running. The final part of the electron gun is a brass cap (Wehnelt) that surrounds the filament with a hole (~1 mm radius) drilled in the middle to let the electrons escape. The Wehnelt is screwed in to the electron gun with a thread of 800 μm $turn^{-1}$ in order to accurately adjust the distance between the top of the filament and the Wehnelt aperture. The electrons produced by the filament are accelerated towards the focusing lens and therefore the graphite target, by a potential difference applied between the filament itself (cathode) and the target (anode). The target is isolated from the rest of the source and its potential maintained at 0 V. The energy of the electrons hitting the target is therefore determined by adjusting the voltage of the filament. As the potential difference between the cathode and the anode will attract the electrons towards the target (anode), it is common to call it the "anode voltage" even if strictly speaking it is the cathode voltage that is adjusted. Having the target isolated allows the current produced by the electrons hitting the target to be monitored, as this is a good indication of the X-ray rate produced. The potential difference between the filament and the Wehnelt can also be adjusted. This potential difference together with the distance between the Wehnelt and the filament, play a critical role in determining the flux of electrons leaving the electron gun. Electronic details of the microprobe X-ray source are shown in the figure 2.5.

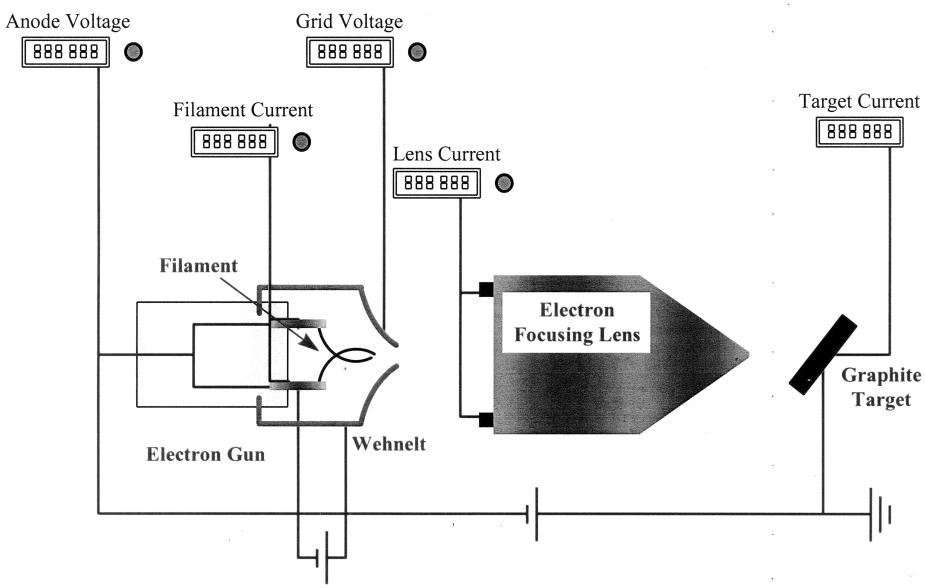

Figure 2.5. *Schematic illustration of the main electric components of the microprobe X-ray source MK I.*

As part of the refurbishment of the microprobe facility, the microprobe source was equipped with a new power supply that allowed anode voltages up to 15 kV (producing electrons of energy up to 15 keV). The power supply also limits the maximum number of electrons that can travel from the filament to the target to a current of 10 mA. The features of this power supply have been chosen on the basis of unpublished information (Shand M. T., 2012) that suggested a peak for carbon K X-ray production as a function of the incident electron energy at about 10 keV. The maximum current was chosen considering the maximum power that is possible to dissipate into the carbon target without damaging it. If all the electrons that leave the electron gun hit the target, they will dissipate a total power of 20 W, well beyond the target limit considering that no cooling system is present at the moment. The filament

current, the anode voltage and the Wehnelt voltage are all continuously monitored and can be individually adjusted at any time during the experiment in order to control the carbon K X-ray rate.

The accelerated electrons are focused on to the carbon target by a water-cooled magnetic lens. Initially, the entrance aperture of the lens was about 1 mm in diameter but it was subsequently replaced by a 2.5 mm diameter aperture in order to increase the number of electrons focused on to the target and therefore the number of characteristic X-rays. The Wehnelt and the lens entrance aperture are aligned by adjusting the position of the electron gun to maximize the number of electrons hitting the target (i.e., the target current). The lens consists of two deflection coils and a solenoid. The deflection coils are arranged orthogonally to each other to steer the electron beam. This allows us to control the location of the electron beam on the target. The coils were originally designed for an X-ray microscopy application where the electron beam had to be scanned on the carbon target. In the current application, they are used before the biological experiments to ensure that the electrons are focused on the target.

Electron focusing is done by the solenoid. The wires forming the solenoid are twisted around a metallic tube down which the electrons can travel from the filament to the target. In this way the magnetic field produced by the solenoid is directed along the tube. The electrons are therefore subjected to this magnetic field before reaching the target and constrained to a beam of

micrometer size. Adjusting the current that runs through the solenoid can control the intensity of the magnetic field. This is necessary in order to focus into the target electron beams of different energies. Figure 2.6 and 2.7 show the structure of the electromagnetic focusing lens.

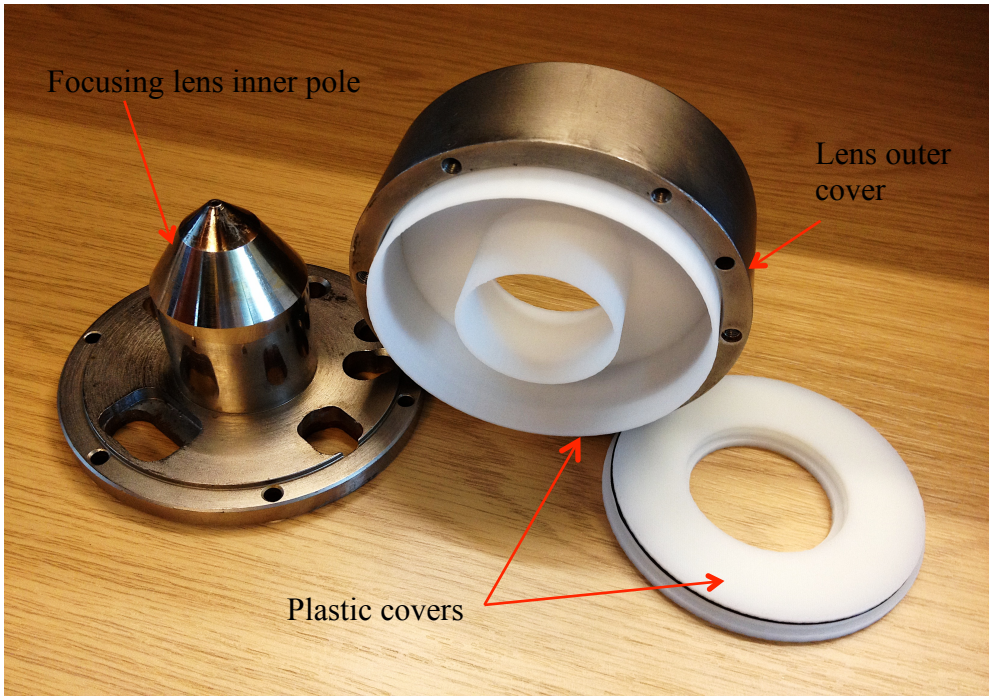

Figure 2.6. *Structure of the focusing electromagnetic lens. Solenoid placed inside the plastic covers.*

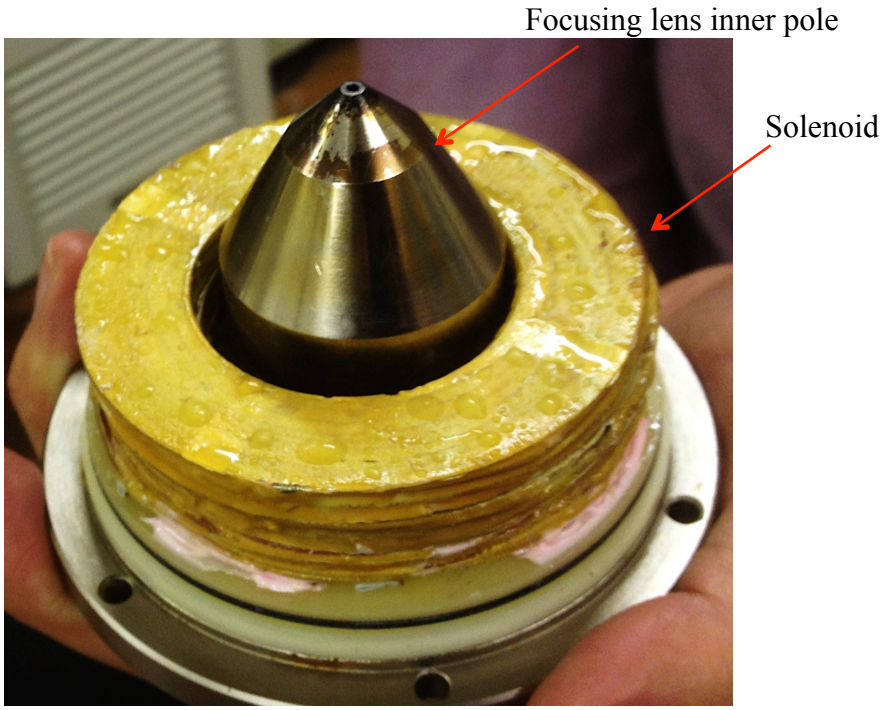

Figure 2.7. *Water shield solenoid placed around inner pole of the focusing lens.*

Since the focusing action of the zone plate is analogous to that of a conventional optical lens, the X-ray focus corresponds to the image produced by the zone plate of the X-ray source (i.e., the spot produced by the electrons on the graphite target). Therefore, the size of the X-ray focal spot critically depends on that of the electron spot on the target. Using the electromagnetic lens, the electrons can be confined to a spot of diameter ~ 200 μm.

The target is placed 5 mm from the lens exit. A 4.4 mm thick graphite block with an area of about 110 mm^2 exposed to the electrons is used as the target. It is oriented at 45^0, both to the electron direction and the zone plate assembly. Due to the short range of the electrons in graphite, this allows the X-rays to emerge from the exit window (positioned above the target)

without attenuation in the target (self-absorption). The graphite block is held by an isolated brass support connected to an electrical vacuum feed through in order to monitor the number of electrons hitting the target per second (target current). When the other parameters of the source are kept constant (i.e., anode voltage, filament current and electron gun position), there is a unique relationship between the target current (whose intensity can be controlled by adjusting the Wehnelt position and potential) and the carbon K X-ray production. Therefore the X-ray rate can be determined during the exposures by monitoring the target current.

The exit window is a 100 nm thick silicon nitride (Si_3N_4) window with an area of (500 ×500 μm^2). These windows are strong enough to hold an atmosphere of pressure difference and present a high transmission for low energy photons. (e.g., transmission of 44 % for 278 eV carbon K X-rays). Better transmission could be achieved using very thin Mylar film (0.9 μm would result in a 55 % transmission, 0.5 μm would result in a 65 % transmission) but are very fragile for the required vacuum conditions. Figure 2.8 shows the transmission of different windows for low energy photons.

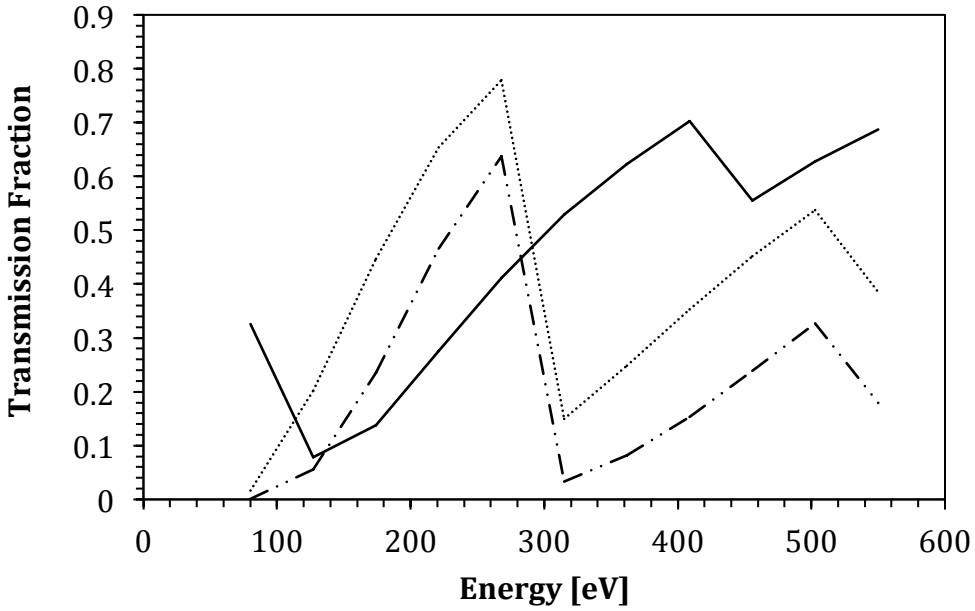

Figure 2.8. *Low energy transmission fraction for different vacuum windows. (——) 100 nm silicon nitride (Si_3N_4), (·····) 0.5 μm Mylar ($C_{10}H_8O_4$), (– · · –) 0.9 μm Mylar. (from Henke.lbl.gov / CXRO data program)*

2.4 The Silica mirror

The electrons focused onto the graphite target produce both characteristic X-rays and continuous bremsstrahlung. Bremsstrahlung is produced when incident electrons are deflected by the electric field of the nuclei of the target. The subsequent transitions between a continuum of energy levels produce a continuum spectrum up to the incident electron energy. For radiobiology purposes it is necessary to obtain an almost pure beam of carbon K X-rays in order to achieve critical sub-cellular targeting. The focal length of the zone plate also depends on the energy of the incident photons, therefore bremsstrahlung would be focused differently from the carbon K X-rays giving

a constant unfocused background to the absorbed dose. Using the phenomenon of total reflection, which occurs at small incident angles and low energies, it is possible to use a mirror to "filter" the X-ray spectrum. The difficulties in using optical elements to reflect X-rays is mainly due to the small values of the refractive index decrement δ (typically values of 10^{-2} -10^{-5}). This means that the complex refractive index (n = 1- δ - iβ) is very close to unity so that reflectivities are large only at very small angles (normal-incident X-ray reflectivities are of the order of magnitude of δ^2).

High reflectivity, however, is obtained at very small grazing incidence angles. As shown by Snell's law

$$n_1 \cos\theta_i = n_2 \cos\theta_r \tag{2.6}$$

where θ_i and θ_r are the incident and refracted angles, n_1 and n_2 are the refractive indexes of air ($n_1 = 1$) and the mirror, for incidence angles smaller than the critical angle θ_c, where

$$\cos\theta_c = n_2 = 1 - \delta \tag{2.7}$$

the electromagnetic waves cannot propagate in the mirror and total reflection occurs. For $\theta_i < \theta_c$ and with $n_1 = n_{air} = 1$, no values of θ_r satisfy Snell's equation, i.e., there is no refracted wave and all of the incident wave has to be reflected. In practice, however, a total reflectivity is never obtained; because of imperfectly smooth surfaces and impure mirror material, a fraction of X-rays is always absorbed by the mirror.

Using a simulation program (*Henke.lbl.gov / CXRO data program*) which uses measured X-ray characteristics, reflection properties have been investigated in order to choose the most suitable mirror materials and configuration. The result indicate for that, for very small incident angles, mirrors made of low atomic number materials reflect a very high fraction of low-energy X-rays (such as carbon K = 278 eV), while almost removing the bremsstrahlung component. Higher reflectivities for low-energy X-rays (< 500 eV) are achieved with relatively high atomic number mirrors (e.g., gold Z = 79 and iron Z = 26) at the expense of a less pure output. For example, using a copper mirror (Z = 29) at a grazing angle of 3^0, it is possible to reflect more than 70 % of the low-energy X-rays but the reflected beam will still contain more than 1 % of 2 keV bremsstrahlung. Under the same conditions, using an aluminium mirror (Z = 13) the low-energy X-ray output decreases to about 65 % but now less than 0.07 % of 2 keV bremsstrahlung is reflected. A silica mirror was therefore chosen (SiO_2, Z_{si} = 14 and Z_o = 8), assuring a high reflectivity for the energy range 100 – 500 eV while substantially reducing the bremsstrahlung component about 1 keV.

The incident angle also plays a fundamental role in filtering the X-ray spectra. Using a ray tracing program (*Henke.lbl.gov / CXRO data program*), it has been calculated that with a very small incident angle (< 1^o), a reflectivity of nearly 80 % is achieved for quite a large range of energies (0 – 1.6) keV. However, as the incidence angle increases the reflectivity drops in a non-uniform manner as a function of the X-ray energy. Low-energy X-rays (<

400 eV) still have quite high reflectivities (> 30 %) for incident angles up to 4° while the higher-energy bremsstrahlung (> 700 eV) is already reduced to less than 1 % at an incident angle of 3°. The simulations seems to indicate that the optimum angle for simultaneously maximizing characteristic carbon K X-ray output and minimizing the bremsstrahlung component is about 3° as shown in figure 2.9.

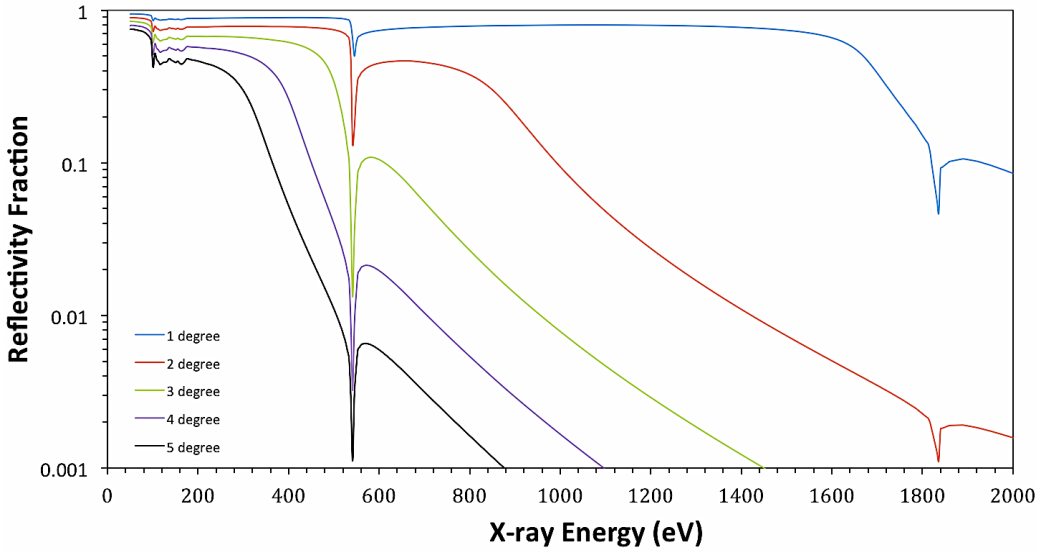

Figure 2.9. *Reflectivity of a silica mirror as a function of the incident X-ray energy for different grazing angles. (from Henke.lbl.gov / CXRO data program)*

The silica mirror was originally held in a fixed position between the graphite target (i.e., X-ray source) and the exit window. This arrangement does not allow us to regulate the X-ray reflection angle preventing full advantage of the best carbon K X-ray reflecting conditions to be taken. A new arrangement to hold and occasionally position the mirror had to be designed and built. This

arrangement enables the simultaneous rotation of the mirror around a pivot and translation of the mirror itself (and the exit window) relative to the X-ray source.

As the pivot is placed just below the exit window, the mirror rotation determines the angle between the mirror surface and the axis orthogonal to the exit window (i.e., reflection angle). On the other hand, the X-ray incidence angle (i.e., the angle between the mirror surface and the imaginary line that connects the X-ray source with the reflection point on the mirror) is determined both by the mirror turning and by the flange translation. As indicated in figure 2.9, the mirror turning and the exit flange translation are controlled independently and externally by two micrometers (technical designs are shown in figure 2.11 A and 2.11 B). In order to have the reflected photons emerging orthogonally to the exit window, the incidence and reflection angles have to be adjusted to the same value. The requirement of orthogonality between the emerging X-ray beam and the exit window is necessary in order to have a vertical X-ray optical path along which to easily align the X-ray focusing elements and the biological samples. The maximum X-ray reflection angle that is possible to select with this arrangement, is about 4.5^{o}, because of space limitations inside the X-ray chamber.

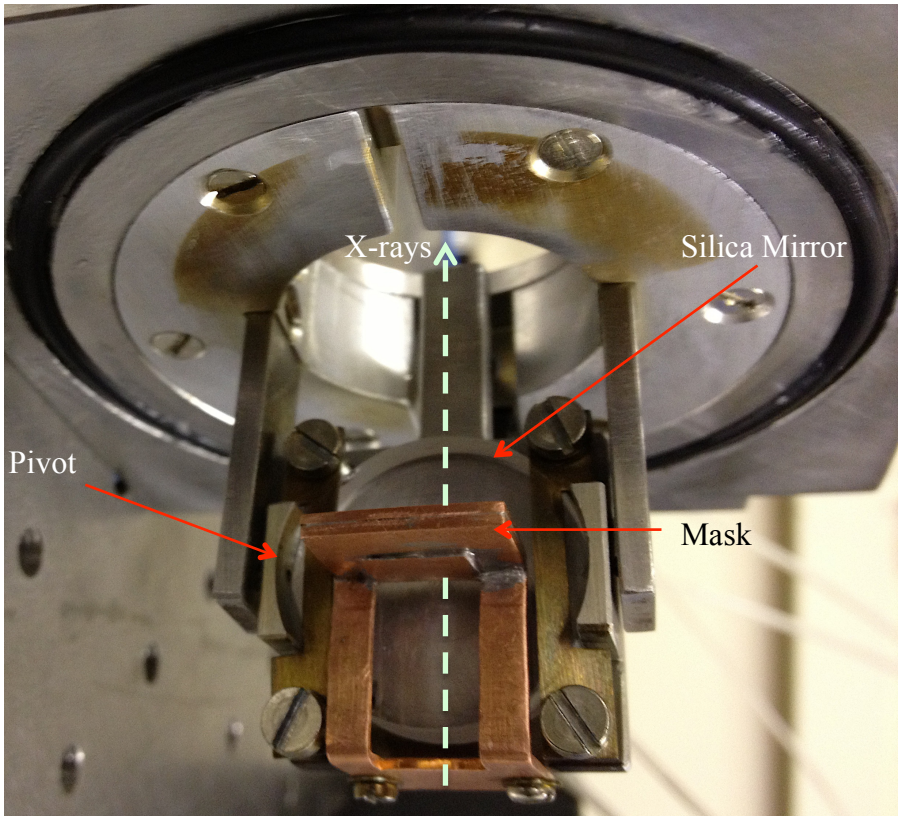

Figure 2.10. *Arrangement to position the Silica mirror for bremsstrahlung elimination. The mask is necessary to avoid straight through radiation. The gap between the mask and the mirror surface is about 400 µm.*

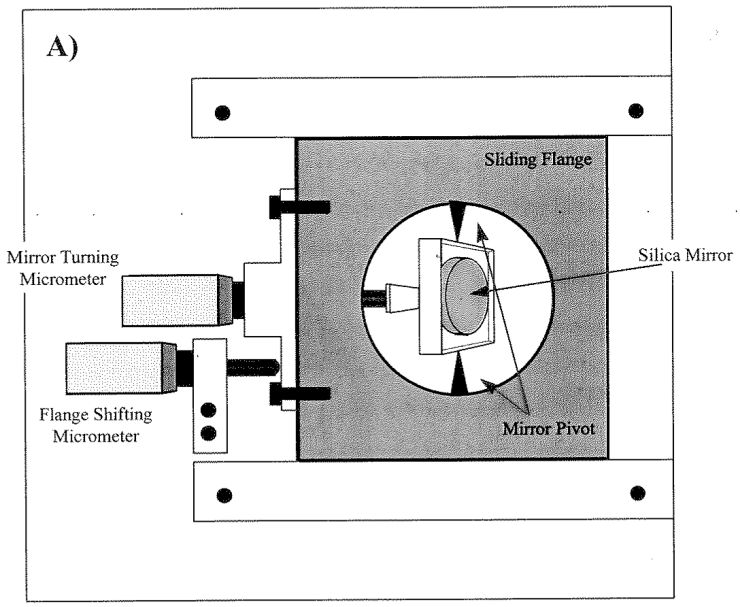

Figure 2.11 A. *Top view of the Silica mirror positioning assembly.*

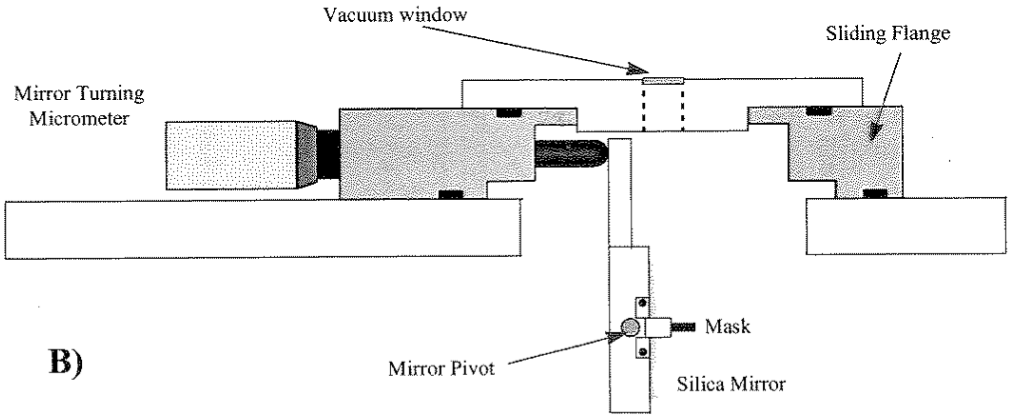

Figure 2.11 B. *Side view of the Silica mirror positioning assembly.*

2.5 X-ray focusing elements

The X-ray focusing system is based on a circular diffraction grating with increasing line density (zone plate) and a small pinhole (order selecting aperture, OSA). Using a zone plate, the characteristic X-ray beam is diffracted to a series of positive and negative (virtual) foci ($m = \pm 1, \pm 2, \pm 3, \ldots$) plus some undiffracted radiation corresponding to the order $m = 0$. A central mask (apodized spot) and the OSA, appropriately positioned above the zone plate, prevent all but the first-order radiation from reaching the samples. A schematic illustration of the action of the focusing system is shown in figure 2.12.

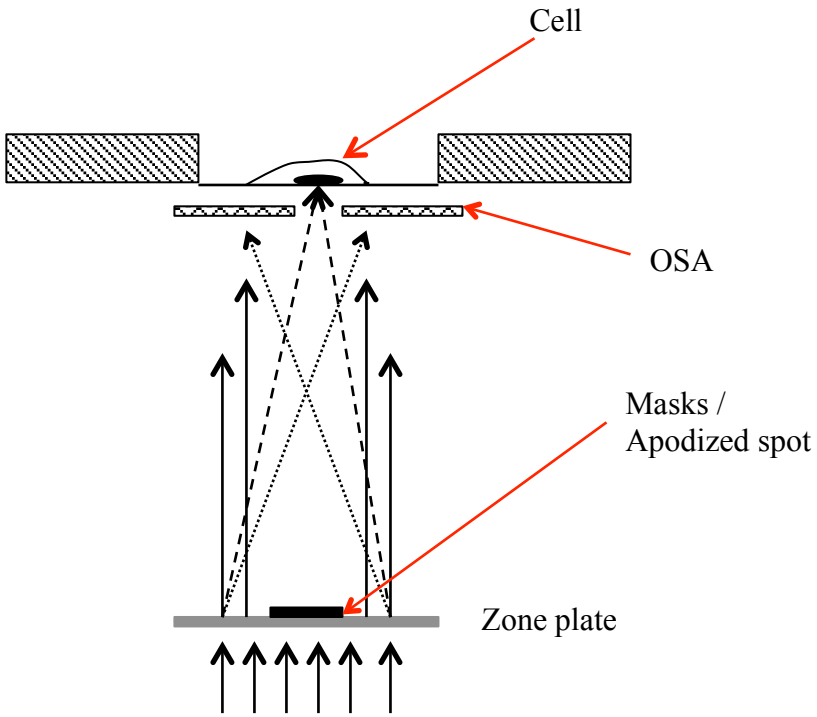

Figure 2.12. *Schematic representation of zone plate focusing action. Zero order (solid arrows) and third-order radiation (dotted arrows) are stopped by masks (Apodized spot and OSA) and only the first order (dashed arrows) is focused on the cells.*

2.5.1 Zone plate assembly

A special arrangement to assemble and align the X-ray focusing elements (i.e., the zone plate and the OSA) has been designed. This assembly must provide some flexibility in the alignment procedure, as zone plates with different characteristics may be needed. The arrangement is mounted on a circular flange located above the silica mirror (figure 2.13). The critical parts are assembled at the end of a vertical tube (internal hole diameter of 3 mm) whose external surface is engraved with vertical grooves. At the top exit of the

tube, a silicon nitride window (100 nm thick) is glued to a cap (that forms a seal with the tube) and works as a vacuum window. The zone plate chip (usually 5 × 5 mm^2) is planned to assemble on a metallic disk (1 mm diameter) using an aerosol glue (photo spray mount). The metallic disk is located above the silicon nitride window and secured by a circular magnetic sheet glued on to the cap. The clamping arrangement using the magnetic sheet is strong enough to avoid unwanted movements, due to the source vibration or to accidental knocking, but allows us to easily move the zone plate for an easy alignment of the zone plate with the exit window. Moreover, the absence of screws or other forms of mechanical clamping reduce the movements due to the clamping operations. The end of the tube with the cap and the zone plate, is surrounded by a cylinder that can slide along the vertical tube. The vertical grooves engraved along the tube, and ball bearings within the cylinder assure a precise vertical sliding of the cylinder while preventing rotational and horizontal movements. The bottom part of the cylinder is equipped with a clamp in order to lock the cylinder at any desired height along the tube. On the top of the cylinder, a second metallic disk carrying the OSA is clamped, again using magnetic sheets. The cylinder cavity is flushed with helium in order to reduce the X-ray attenuation. The technical drawing is shown in figure 2.14.

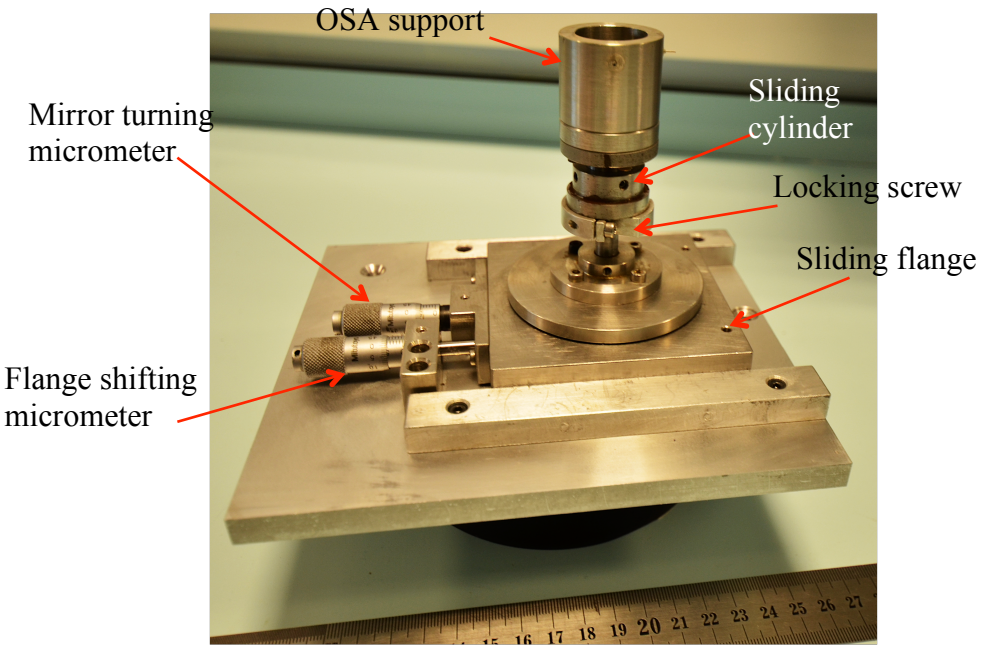

Figure 2.13. *Picture of the X-ray focusing elements assembly.*

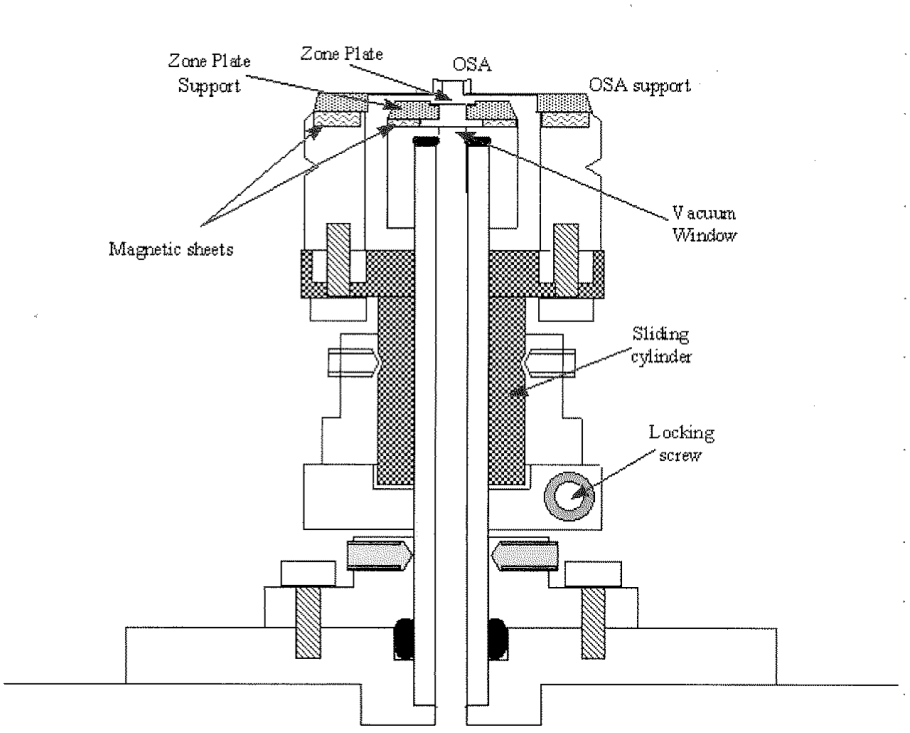

Figure 2.14. *Structure of the X-ray focusing element assembly.*

2.6 The micro imaging and irradiation stage system

The imaging acquisition and micropositioning system consist of a UV epi-fluorescence microscope coupled to a Charge Coupled Device (CCD) camera and a three axis micropositioning stage (figure 2.15). The micropositioning stage (Prior H101A, Prior Scientific Limited, Cambridge, UK) has an accuracy of 250 nm $step^{-1}$ in the *x*-*y* direction and will used to support the dishes with the biological samples in order to scan them under the microscope objective and finally align them with the probe. The cell dishes will clamped to the stage by pressing it against a reference corner with a screw. This prevents the dish from sliding on to the stage during the stage acceleration. Moreover, the cell dish can be repositioned in the same position and orientation with an uncertainty of few hundreds of microns at any time after the irradiation.

The stage can be operated either manually, using a joystick (in the *x* and *y* direction), or more accurately via a personal computer (in all three directions). Using an optical iris, it is also possible to couple the micropositioning stage to any of the X-ray focusing elements (i.e., zone plate and OSA). In this way the alignment of the focusing elements can be precisely performed “on line” using the microscope to visualize them. Replacing the microscope objective with the X-ray detector, fine adjustment can be made to the OSA in order to improve the alignment, (by maximizing the X-ray count rate). The use of the optical iris allows the X-ray focusing elements to be clamped and released avoiding changes in position.

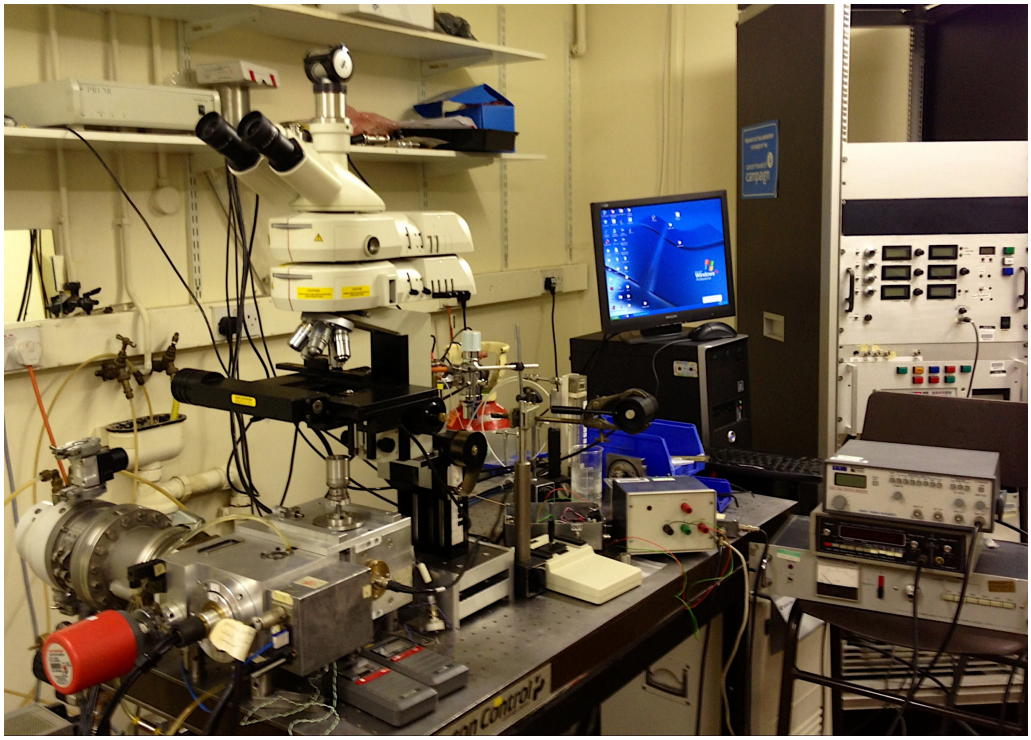

Figure 2.15. *MK I microprobe facility for radiobiological studies.*

The custom-built epi-illuminated polarized microscope (Leica DMLM, Leica Microsystems (UK) Ltd) and CCD camera (Philips UK Ltd) are assembled above the micropositioning stage. As the position of the X-ray focus spot produced by the zone plate and that of the focusing elements themselves is not adjustable in the vertical direction, it is necessary to be able to move the microscope in the *z* direction in order to focus on the zone plate, the OSA or the sample targets. This can be done using microscope stage. The main characteristic of this microscope is the non-critical importance of the distance between the various optical elements of the microscope such that the objective can be moved in the *z*-direction such that the acquired image will always have the same characteristics (magnification and focal sharpness). The distance between the objective and the sample will obviously remain critical and is

determined by the focal length of the objective used. With this system the microscopy body and the CCD camera can remain fixed while the objective is mounted on a vertical sliding assembly.

The imaging system is based on CCD chip (FT 800) with 672 × 500 pixels. Using a × 10 objective, the field of view obtained is approximately 1.400 × 1.052 mm and each pixel covers an area of 2.1 × 2.1 μm^2. This results in a good spatial resolution without the need for further optical elements that would reduce sensitivity. The resolution of the system is obviously related to the magnification of the objective used. With a × 10 water immersion lens, a resolution of the order of a few micrometers is obtainable, while using a × 40 lens a resolution finer than 1 μm can be achieved.

The micro-positioning stage, the image acquisitioning system is planned to be individually controlled by custom designed software (based on Visilog) that also monitors the status of the X-ray source. The software is still under development but the main functions have already been developed. This controls the CCD camera and the micropositioning stage to provide the basic image processing routines needed for object finding. The main camera setting (CCD gain, intensifier gain) can all be continuously monitored and controlled.

2.7 Microprobe X-ray detector

There are different types of X-ray detectors (i.e., X-ray film, channel electron multipliers, gas detectors, semiconductor detectors), each

characterized by specific properties like efficiency, spatial and energy resolution. The X-ray detector used to measure the microprobe output is a proportional gas counter. Several factors influence the choice of a proportional counter as X-ray detector for the microprobe. First, using a proportional chamber it is possible to acquire a full energy spectrum of the emerging X-ray beam, essential to evaluate the bremsstrahlung component. Moreover, the use of thin Mylar films as entrance window (the same used as substrates for the cell dishes) and the high detection efficiency of the gas used [P 10 gas (10 % methane in argon) detection efficiency > 99%] allow us to measure the X-ray dose to which the sample will be irradiated without further calculations or extrapolations. Finally, proportional chambers offer the advantage to measure the X-ray dose rate in real time without the need of subsequent chemical or optical developments.

Gas detectors work by collecting the ions generated by the interaction of X-ray photons with the atoms of the gas. With an appropriate difference of potential between the anode and the cathode, the electrons produced by the X-ray are sufficiently accelerated to cause further ionisation in proximity of the anode. The magnitude of the induced potential will be then directly proportional to the energy of the incident X-rays. The energy resolution for proportional counters is determined by the spread of the pulse height and therefore by the number of electrons produced per incident photon. Considering the statistical fluctuations in the number of electrons produced by a single photon interacting with P 10 gas and in the electron multiplication gain

that occurs close to the anode, the relative statistical variation in the pulse height is given by (Michette and Buckley, 1993b)

$$\frac{\Delta E}{E} = \frac{\Delta p}{p} \approx \frac{0.43W}{\sqrt{E}} \tag{2.8}$$

where W is the average energy required to produce an ion pair. From equation (2.8) it is possible to note how the energy resolution for proportional counters improves, increasing the energy of the incident X-rays. Using P 10 (W ~ 25 eV) to fill the chamber, an energy resolution of ~ 65 % is expected for carbon K X-rays.

The geometry of the proportional counter used for detecting carbon K X-rays from the microprobe source is shown in figure 2.16. The anode consists of a brass pin with a hemispherical end (~ 0.5 mm radius) positioned in the middle of an aluminium chamber. The body of the detector (i.e., the cathode) is kept neutral while a voltage can be supplied to the pin in order to create a potential difference between the electrodes. The inside of the chamber is shaped so as to maintain a uniform electric field around the anode. The radiation-entrance window is a 0.5 μm thick Mylar film placed at the end of the chamber so that the radiation must enter the detector parallel to the anode. The top of the chamber is equipped with two holes that are used to fill the detector with the detection gas.

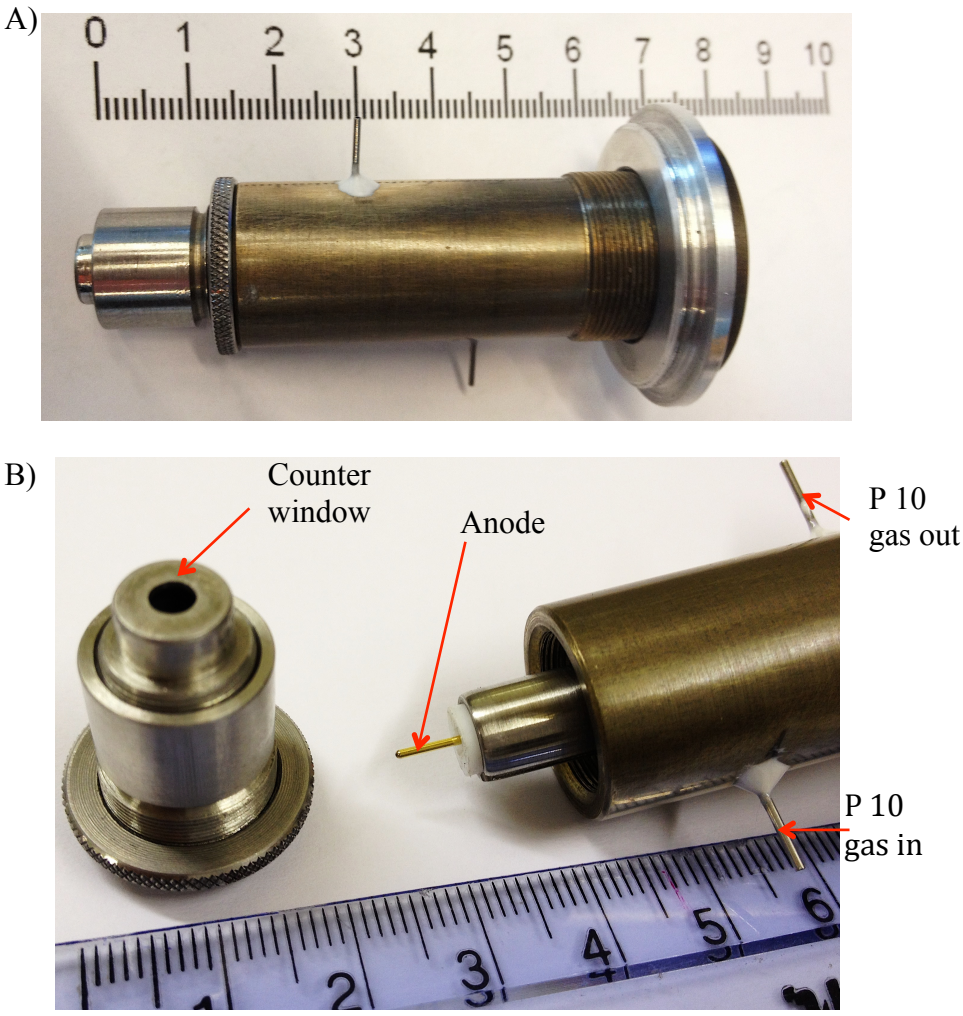

Figure 2.16. *Custom built proportional counter used to measure the microprobe X-ray output. A) Proportional counter B) Counter inner structure.*

The detector pulse-height signal is acquired on a PC based multichannel analyzer after being appropriately amplified and shaped using commercial pre-amplifier and amplifier modules. Using the multichannel analyzer, the signal spectrum produced by the detector can be expressed as a function of the energy of the photon that originates the signal. This classification is necessary in order to analyze the energy spectra of the

emerging X-ray beam, evaluate the bremsstrahlung component and finally quantify the characteristic X-ray rate for dosimetric calculations.

2.7.1 Characterization of the X-ray detector

The proportional counter described in above section was characterized at 278 eV using the microprobe itself. Initially an optimum combination of flow rate and pin voltage (anode voltage) was determined for the 3 mm anode pin distance. Measured using a Vernier caliper, this was the maximum distance over which X-rays could be absorbed before the power supply become incapable of providing sufficient anode voltage to collect all the resulting ion-pairs. The integrated count rate was first measured with a flow rate (P 10 gas) of 3 mL s^{-1} at 1300 V and then at 50 V increments up to a maximum of 1900 V. The maximum possible voltage was 2 kV. The procedure was repeated at flow rate intervals of 1 mL s^{-1} up to a maximum of 9 mL s^{-1} whereupon the behavior of the counter become erratic, an indication of Geiger discharge. Despite each curve demonstrating a similar response, the marked increase in counts with flow rate pertained to the pressure of P10 gas in the chamber.

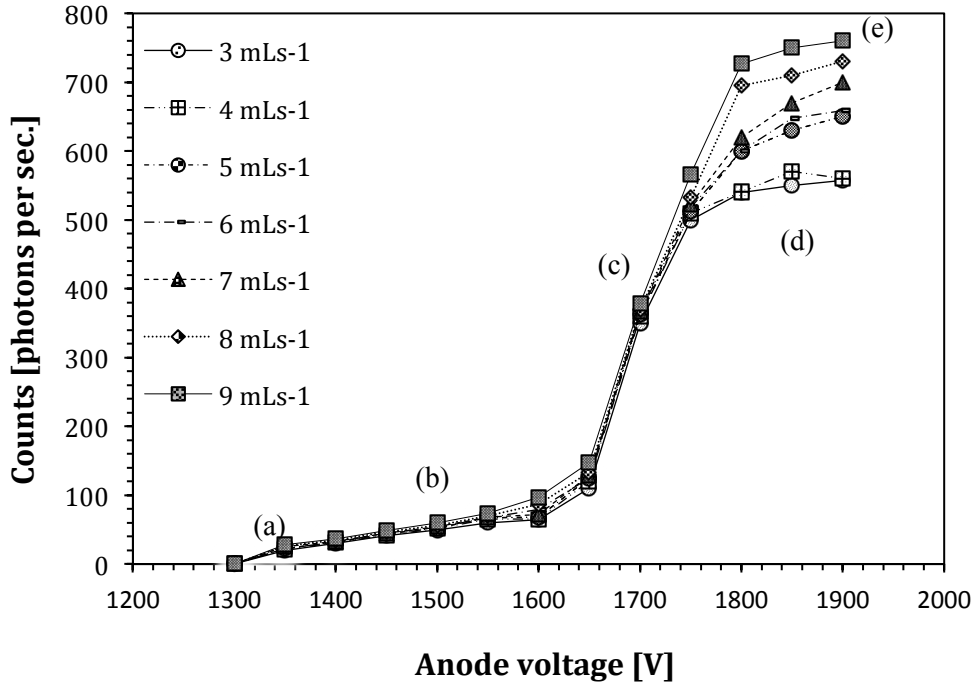

Figure 2.17. *Number of counts as a function of the anode voltage.*

Below 1400 V, absence of counts at any flow rate indicates that recombination of ion-pairs is the dominant process [Figure 2.17 (a)]. As the voltage was raised above this there was a steady increase in counts as the electrons gained sufficient energy to escape their positive partners [Figure 2.17 (b)]. Due to the lack of a smooth knee in the curves between 1600 V and 1650 V there was assumed to be a small plateau that corresponded to ion saturation, although this was not directly observed. Above 1650 V the counter begins to operate in proportional mode [Figure 2.17 (c)], reaching a plateau at 1900 V [Figure 2.17 (d)]. Since, at atmospheric pressure, 278 eV photons are completely absorbed within a path length of 80 micrometers of P 10, this plateau results from collection of all the ion-pairs formed in the counter and implies that at lower voltages the electric field is insufficient to overcome space charge in low field

regions. The maximum value for < 250 eV photons have a transmission of up to ~ 10% under these conditions (Henke et al., 1993). Observations of the stretched Mylar window with increasing gas flow rate showed that it began to bow outwards at flow rates above 7 mL s^{-1}.

Bowing of the window signified that the gas pressure inside the chamber was greater than that of atmosphere on the other. With no precise way to measure pressure in the counter, as it corresponded to atmospheric pressure and could therefore be attributed well-defined absorption properties, 7 mL s^{-1} was chosen as the optimum flow rate. Once operating conditions were established (7 mL s^{-1} at 1900 V), the linear response of the counter was verified.

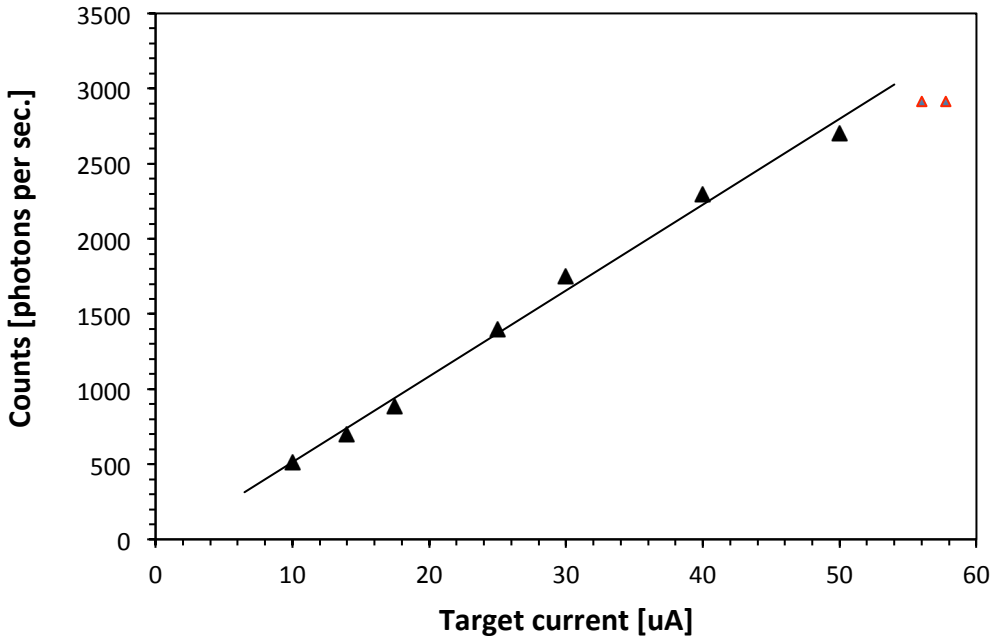

Figure 2.18. *Linearity of counter response with increasing target current. (Average of four measurements at 10 kV, error bars too small to show)*

The X-ray flux from a microprobe is linearly proportional to target current; count rate were measured for increasing target current at a fixed acceleration voltage of 10 kV. To prevent the counter becoming saturated, and to minimize the dead time, a 10 μm diameter aperture (OSA) was used to limit the flux reaching the proportional counter. As expected from theory, count rates increased linearly with current up until approximately 2700 counts per second (Figure 2.18, ▲). Beyond this the response of the counter began to plateau (Figure 2.17, ▲), because at this count rate the dead time ~ 1.2 % was not significantly different from that obtained at lower current.

2.8 Summary

The ultrasoft X-ray microprobe facility developed at the King's College London is based on an electron bombardment source for the production of characteristic carbon K X-rays. Electron bombardment X-ray sources are relatively low cost (compared to laser plasma source or synchrotron facilities). Moreover, their small dimension and relatively straightforward construction are features that make these sources accessible and easily adaptable as part of complex facilities. The main disadvantages presented by the electron bombardment sources are the low efficiency in the production of characteristics X-rays (< 1 %) and the contamination by bremsstrahlung in the produced X-ray beam. The final carbon K X-ray dose rate obtained after few modifications to the existing source is expected to be sufficiently high to allow to perform biological experiments in the low and medium dose region of X-

rays. Further improvements require more critical design with higher energy electron gun and cooling target facilities.

The bremsstrahlung component is removed by using the phenomenon of total reflection that occurs at small reflection angle for low energy photons. Theoretical calculations indicate that focusing the X-ray beam through a small angle reflection on a mirror made by high atomic number material, it is possible to drastically reduce the bremsstrahlung component while a still significant high fraction of carbon K X-ray is reflected. The calculations also suggest the use of silica (SiO_2) mirror and a reflection angle of about 3^o as optimum configuration.

The microscope and the stage are also important elements in locating the targets and in aligning them with the probe for the irradiation. The accuracy of the stage (~ 0.25 μm) and the high-magnification objectives available (× 40) should provide a targeting precision to match the size of the X-ray focus. All the main features of the microprobe facility are controlled via a fast personal computer and in-house developed software that is continuously updated.

Chapter 3

Microprobe source calibration

3.1 MK I source

In the microprobe source, bremsstrahlung and characteristic X-rays are produced by electrons striking a graphite target. For a given anode voltage (e.g., fixed electron energy), the X-ray production rate has been shown to be directly proportional to the number of electrons hitting the target (Atkinson *et at.,*2004). This number of electrons can be determined by monitoring the current generated by the electron beam striking the target (target current), as this is electrically isolated from the rest of the source. Figure 3.1 clearly shows the linear relationship between the characteristic X-ray count rate and the target current measured for the MK I source using custom made proportional counter (see section 2.7) connected with 5001 Universal Counter-Timer.

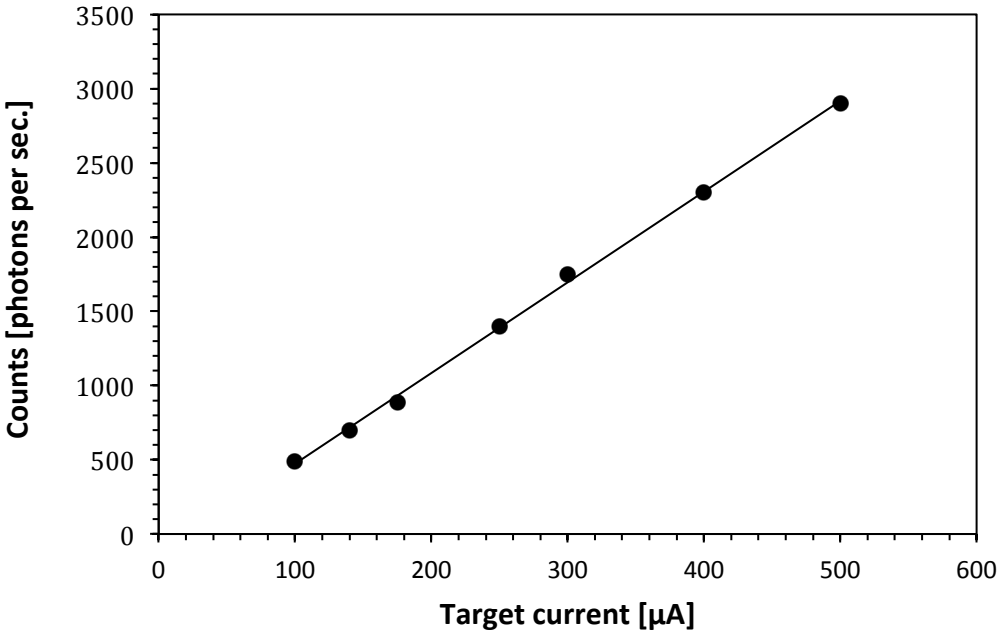

Figure 3.1. *Characteristic X-ray dependence on the target current. Data obtained with an anode voltage of 10 kV and without reflection from the silica mirror (see section 2.3). Target current errors (± 0.05 µm instrument error) are too small to be shown on the graph.*

Therefore, the target current can regulate the X-ray dose rate. This can be determined by the current that runs through the tungsten filament (filament current), assuming the X-ray yield was linearly dependent on the electron beam current.

3.1.1 Electron gun characteristics

The electron gun is possible to align accurately while the source is running, using four electron gun alignment screws. This allows adjustment of the position of the filament head relative to the focusing lens entrance in order

to maximize the number of electrons collected by the electromagnetic lens. The alignment is achieved by maximizing the target current once all the other parameters of the electron gun have been set. Generally, small adjustments of the electron gun position were initially required to compensate filament movements due to thermal variation. The original entrance hole of the focusing lens, which was only 1 mm in diameter, was replaced by a 2.5 mm diameter hole to increase the flux of electrons focused on to the target. Although larger holes will provide a more intense flux of electrons on to the target, increasing the X-ray production rate, they will also result in a larger focal spot. The electron spot produced by the electromagnetic lens on the target can be considered as the image of the hole through which the electrons enter the lens. The minimum size of the electron spot (i.e., the X-ray source) depends critically on the size of the lens entrance hole. Similarly, the size of the X-ray spot produced by the zone plate will depend on the size of the X-ray source.

The number of electrons emitted by the filament is determined by the current passing through it (filament current). According to specifications, it should be possible to run a maximum current of 4.0 A through the filament. However, constant use at this current reduces the lifetime, and so it was chosen to limit the filament current to 3.0 A (see section 2.3). Provided there is a good alignment between the filament and the focusing lens, an increase in the number of electrons produced by increasing the filament current should give a similar variation to the target current. In figure 3.2 the variation of the target

current as a function of the filament current is shown for different distances between the filament and the Wehnelt.

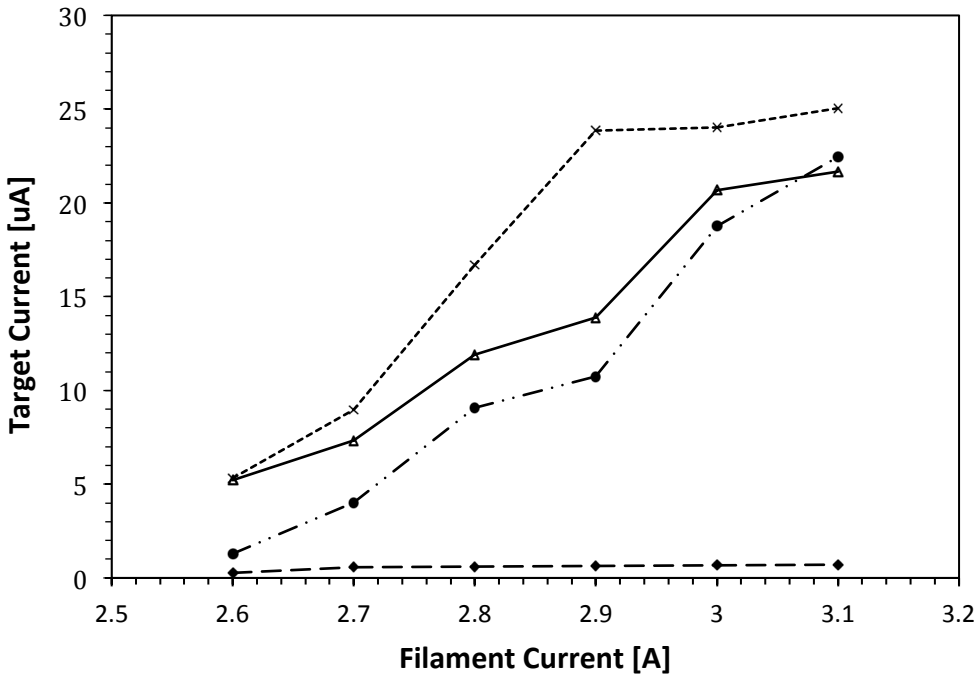

Figure 3.2. *Target current dependence as a function of the filament current for different gaps between the filament and the Wehnelt: (---) 0.0 mm, (-..-) 0.25 mm, (....) 0.5 mm and (⟵) 0.75 mm, Anode voltage was 10 kV. Measured target current errors (± 0.05 μA instrument error) too small to be shown on the graph.*

The observed increase of the target current seems to suggest a liner increase of the number of electrons produced as a function of the filament current. This may suggest that the limitation of a 3.0 A for the filament current should be reconsidered in order to obtain a high X-ray dose rate for specific experiments. From figure 3.2, it is possible to appreciate the importance of the gap between

the filament and the Wehnelt. The position of the Wehnelt and its potential, both play an important role in determining the number of electrons that are emitted by the electron gun. Plotting the same data as figure 3.2 as a function of the filament-Wehnelt gap (figure 3.3), it is evident that there is an optimum distance between the filament and the Wehnelt.

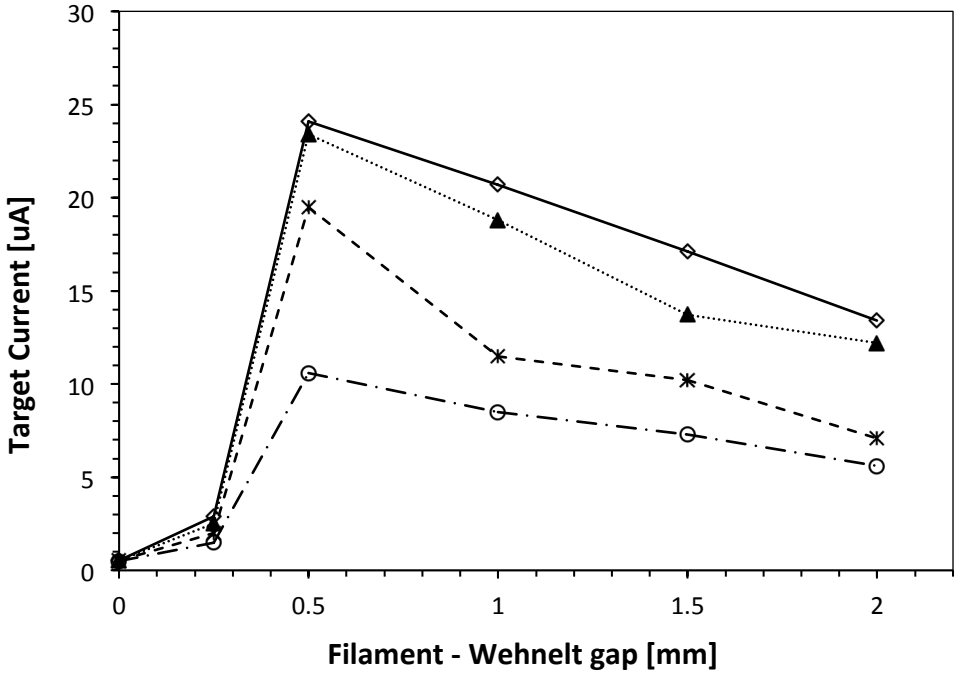

Figure 3.3 *Measured dependence of the target current on the gap between the filament and the Wehnelt for different filament current values. (-.-) 2.7 A, (---) 2.8 A, (....) 2.9 A, (─) 3 A. The potential difference between the Wehnelt and the filament is 3 V in all cases. Target current errors (± 0.05 μA) too small to be shown on the graph.*

For each fixed filament current, the target current passes through a maximum as the distance between the filament and the Wehnelt increases for a fixed Wehnelt potential. As the Wehnelt potential is set to values lower than the

filament potential, the emitted electrons are attracted back to the filament. However, the electrons that escape the filament have an initial kinetic energy and travel towerds the Wehnelt. This will lead to the formation of an electron cloud (space charge) with some electrons attracted back to the filament by the Wehnelt potential, counteracted by new electrons emitted towards the Wehnelt. An appropriate adjustment of the Wehnelt position and of its potential will allow the electric field produced by the cathod-anode potential to reach the electron cloud. The electrons produced will therefore be accelerated towards the carbon target. However, high Wehnelt voltage will shield the electron from the anode voltage. By regulating the Wehnelt voltage, it is therefore possible to control the flux of electrons directed towards the target. The distance between the Wehnelt and the filament is also critical. If the Wehnelt is very close to the filament, it could lie in the electron cloud area, collecting part of the electrons. Only a small fraction of the emitted electrons will therefore be accelerated towards the target. For large distances, on the other hand, even small Wehnelt voltages could shield the electric field of the anode. As suggested by the data in figure 3.3, an optimum situation is reached with a gap of about 0.5 mm between Wehnelt and the filament and with a Wehnelt voltage of about 3 V. All of these situations are illustrated schematically in figure 3.4.

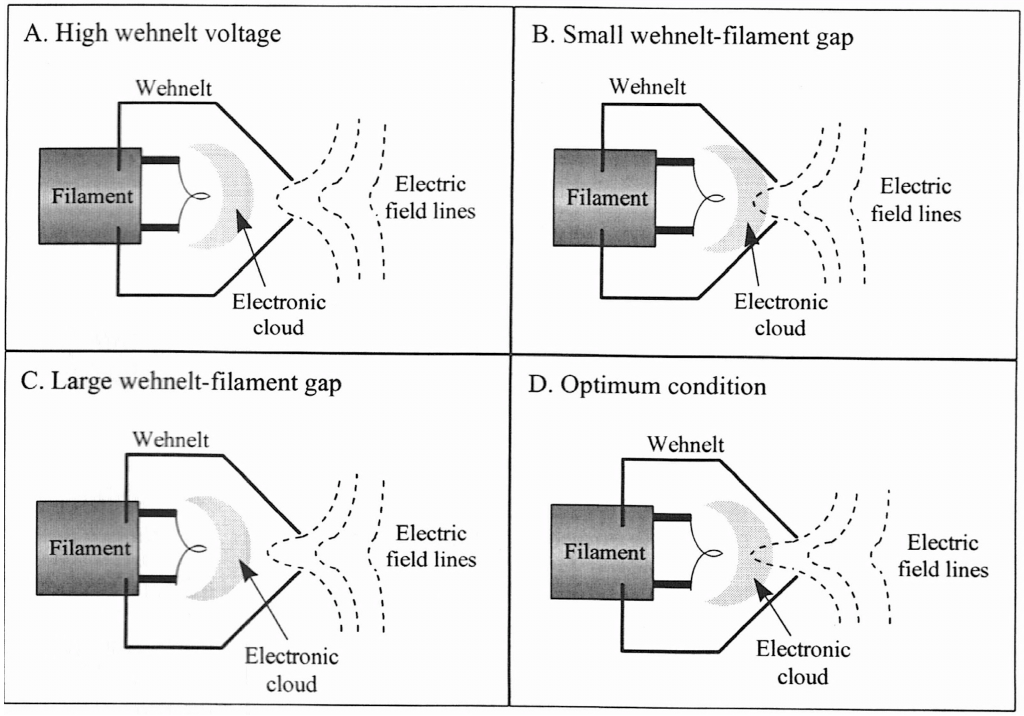

Figure 3.4. *A schematic diagram to highlight the importance of the Wehnelt in directing the electrons towards the target. A) high Wehnelt voltage: the electric field is shielded, the electrons are not accelerated towards the target. B) small Wehnelt-filament gap: some electrons are collected by the Wehnelt itself. C) large Wehnelt-filament gap: the electric field cannot reach the electron cloud. D) optimum conditions: electrons are extracted by the electric field and accelerated toweards the target. (Figure reproduced with kind permission from Hui Jiang)*

While the position of the Wehnelt cannot be altered during the experiment, its voltage can be adjusted at any time allowing control of the electrons flux that hits the target. As indicated in figure 3.4 A, a high Wehnelt voltage shields the electric field produced by the cathode-anode potential preventing the electrons

from escaping. Mesurements of the target current variation as a functions of the Wehnelt voltage are shown in figure 3.5.

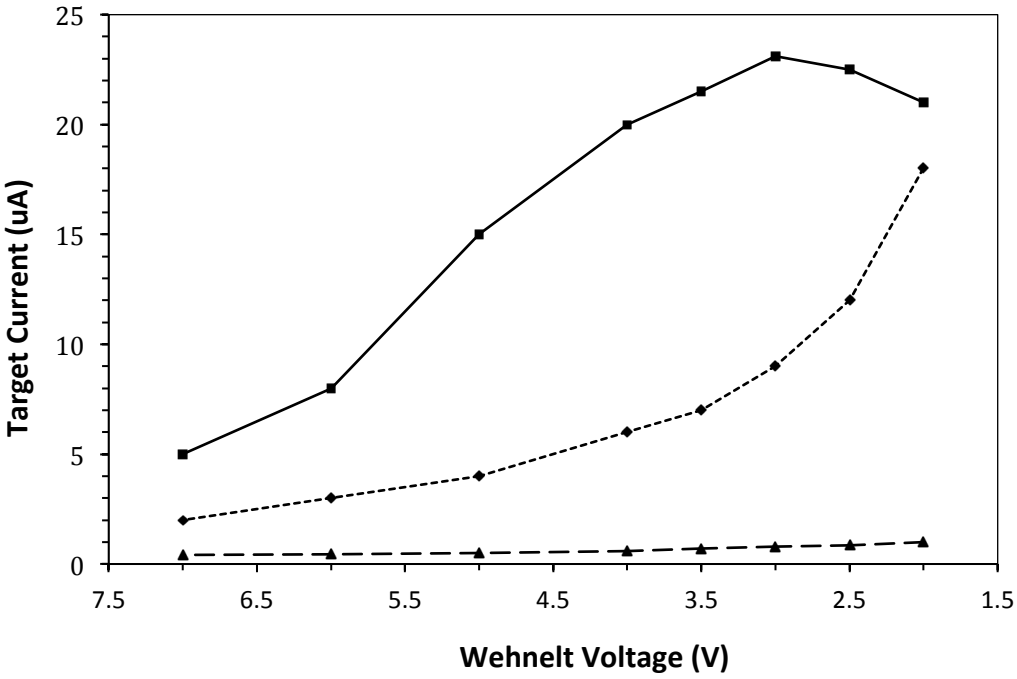

Figure 3.5. *Dependence of the target current from the Wehnelt voltage for different Wehnelt-filament gaps. (——) 500 μm gap, (----) 250 μm gap and (– –) 0 μm gap Target current errors (± 0.05 μm) too small to be shown on the graph.*

The shielding effect of the Wehnelt potential is evident as the target current increases at small Wehnelt voltages. Interestingly, a saturation effect seems to be reached with for a filament-Wehnelt gap of about 0.5 mm and low Wehnelt voltages. This indicates an optimum configuration to extract the maximum flux from the gun. In this configuration the electrons are drawn away from the filament as rapidly as they are emitted.

3.2 Electromagnetic focusing lens

The size of the X-ray focused spot is determined by the characteristics of the zone plate and by the size of the X-ray source. The purpose of the electromagnetic lens is therefore to collect the electrons generated by the filament and to focus them to a fine spot on the target surface. As described in section 2.2 the focusing lens consists of two orthogonal deflection coils and a final focusing solenoid.

The MK I electromagnetic lens is a single coil consisting of 180 turns of copper wire around a soft iron core to create an electromagnetic field for the focusing of the electron beam. In order to test the efficiency of the focusing of the electron beam at a focal spot size, it was drawn in AutoCAD (Autodesk, CA, USA) and a structured mesh constructed with the MESH program Code of the Field Precision software® (Field Precision, NM, USA). For a single pole of the MK I, the concentration of the electro magnetic field lines are generated by a finite element magnetostatic analysis utilizing the PERMAG simulation code as shown in Figure 3.6.

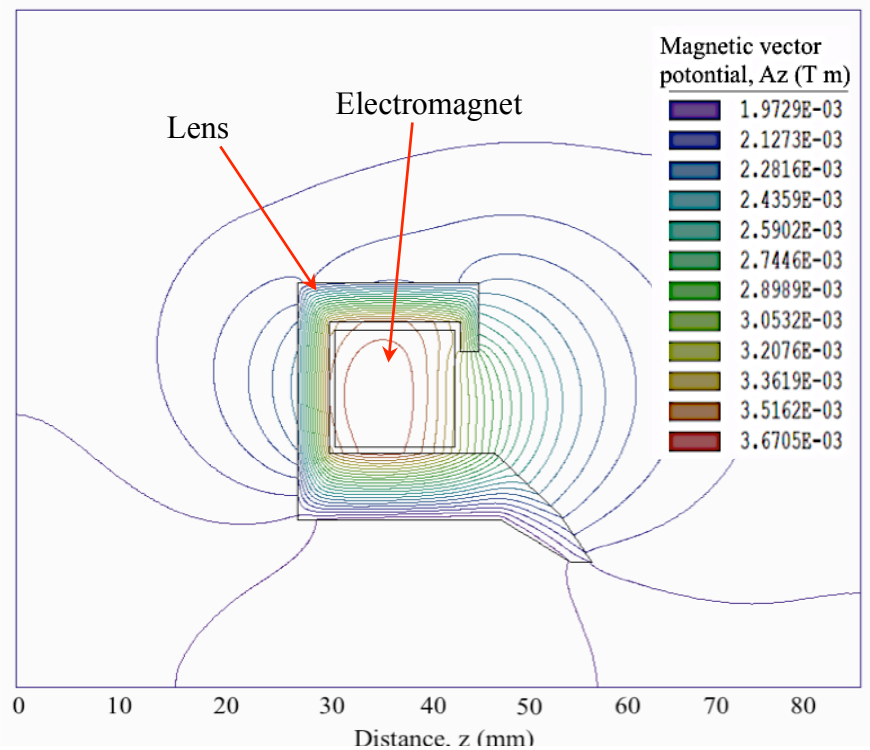

Figure 3.6. *Concentration of filled contour lines in the electromagnetic lens.*

Figure 3.7 shows the calculated concentration of field lines within the electromagnetic lens.

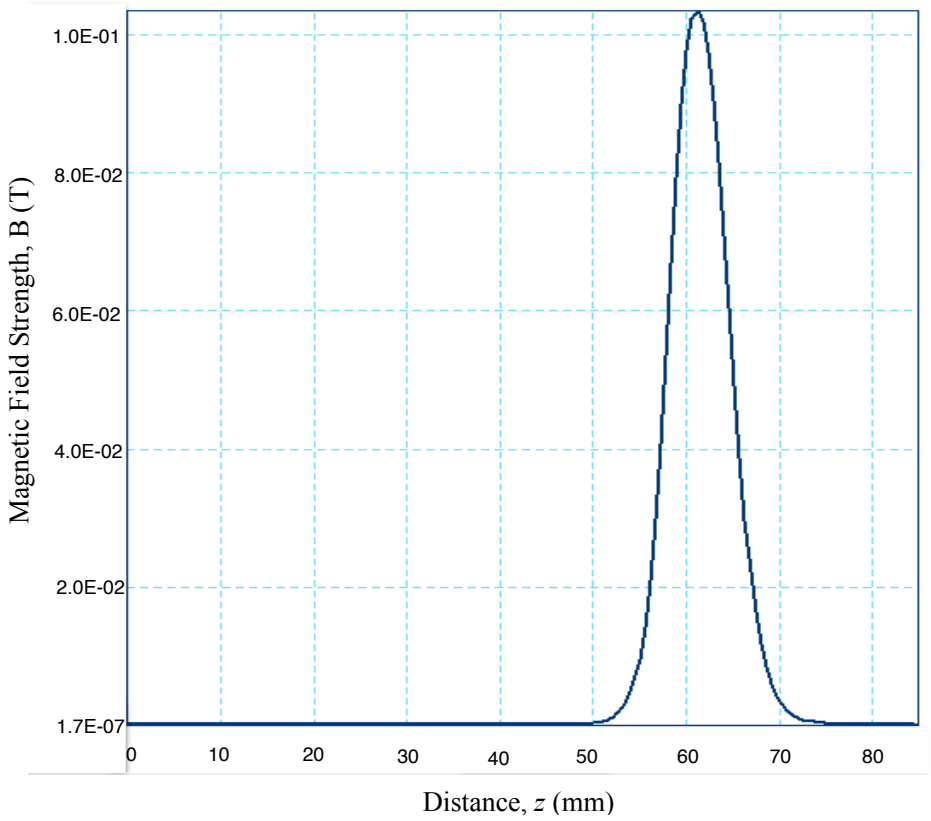

Figure 3.7. *Calculated electromagnetic field strength along the axis of the electromagnetic lens. The estimated maximum magnetic field strength was 0.103T.*

The result of tracking a 10 keV paraxial electron beam (focusing lens current of 10.5 A) through the electromagnetic lens as shown in Figure 3.8, indicates that the electrons are focused to a point roughly 5 mm from the pole piece. The maximum and best-estimated demagnification of the electron beam is estimated to be ~150 μm in diameter.

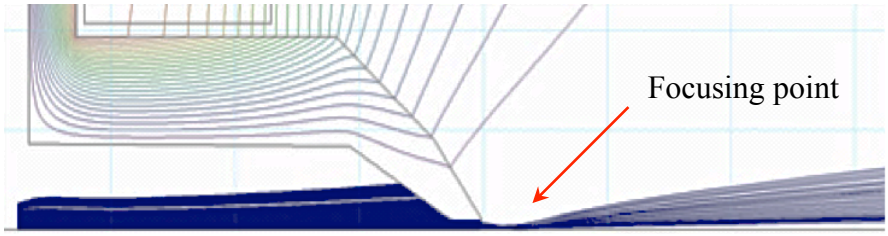

Figure 3.8. *Simulated focal distance for a 10 keV paraxial electron beam.*

There are three main methods to check that the electrons are actually focused on to the graphite target, one of which also allows the spot size to be determined. The first method is based on thermodynamic considerations. The great part of the electron energy dissipated into the target will increase its temperature while only a minor fraction will produce bremsstrahlung and an even smaller fraction characteristic X-rays. As the electrons are focused, they do not hit the target uniformly resulting in a non-uniform energy distribution. The subsequent temperature increase will also not be uniform because of the low conductivity of the graphite. Moreover, the temperature of the part of the target on which the electrons are focused will depend on the number and energy of the incident electrons (i.e., the total energy deposited) and on the size of the focal spot. Because the heat produced by the electrons remains localised on the target, for the same total energy deposited the target will reach different temperatures according to the size of the electron spot. The power dissipated in the graphite target (defined as energy per unit area) represents a good indication of how the target temperature changes with the size of the electron spot. As the target changes its temperature, it will emit a different electromagnetic spectrum that will finally depend on the size to which the

electrons are focused on to the graphite target. An analysis of such a spectrum as function of the current that runs through the focusing solenoid indicates the optimum solenoid current for the finest electron focus. The best electron focus will be characterized by an electromagnetic spectrum clearly shifted towards the red region. This method does not provide any estimate of the size of the electron spot. Moreover, it presents some technical difficulties that make it not particularly suitable for the present case. In order to analyze the electromagnetic spectrum emitted by the target, it has to be possible to have visible access to the target surface, but the microprobe source does not allow this. Accurate equipment has also to be used in order to detect changes in the electromagnetic spectrum that could be very small. Finally, the light from the heated tungsten filament will add complications to the spectrum analysis.

The second method was evaluating the electron distribution. A measurement of electron distribution has been achieved using a phosphor scintillator [type of phosphor: ZnS:Ag (P-22 Blue)] screen, converting the energy of incident electrons falling on the target to visible light. The visible light produced may then imaged using visible light CCD with a zoom lens focused onto the target. Installation of a clear glass window directly on the exit port of the microfocus source allows the CCD to be positioned close to the source. By changing the current passing through the solenoid of the magnetic focusing lens, the smallest distribution of electrons incident on the target may be determined, allowing the properties of the electromagnetic focusing lens to be evaluated. This is shown in figure 3.9, where the visible image produced by the phosphor screen is

recorded in both the horizontal and vertical direction. In order to avoid damage to the phosphor screen, the filament current of the electron gun was limited to 2.0 A, reducing the current contained within the electron beam.

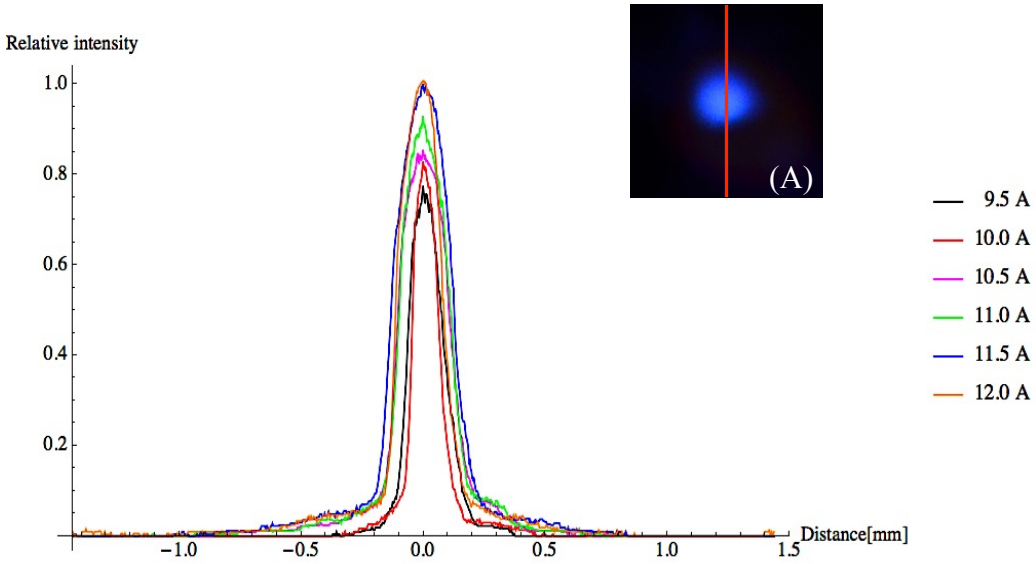

Figure 3.9 (a). *Electron distribution at the X-ray target, estimated by conversion to visible light using a scintillator screen placed on the X-ray target in vertical direction [Image (A)]. This image (A) shows the visible light image on 10.5 A lens current.*

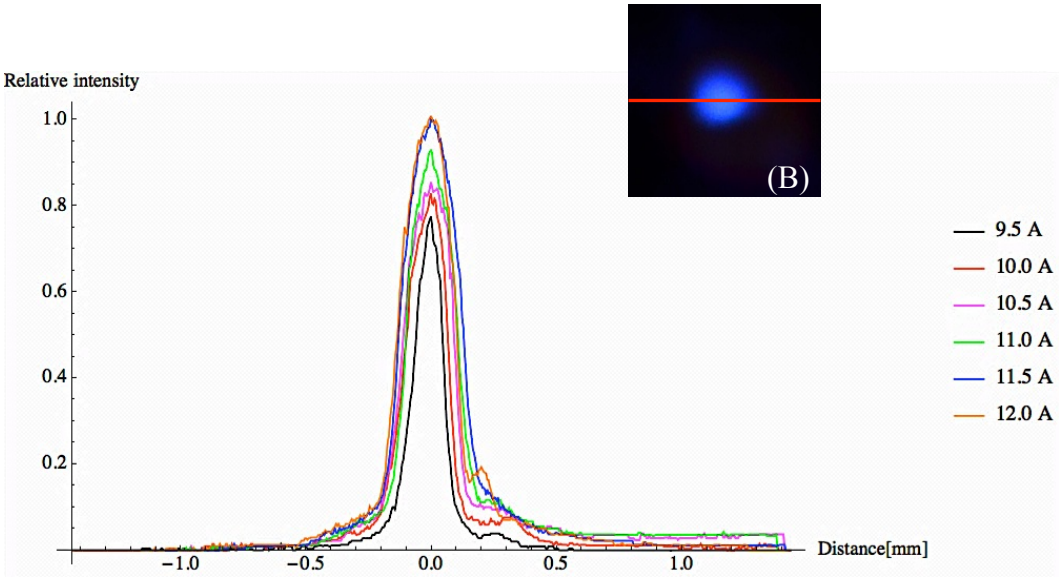

Figure 3.9 (b). *Electron distribution at the X-ray target, estimated by conversion to visible light using a scintillator screen placed on the X-ray target in horizontal direction [Image (B)]. This image (B) shows the visible light image on 10.5 A lens current.*

Figure 3.9 (a) and (b) show that the diameter of the electron beam is has a width of ≈ 200 μm obtained at a focusing lens current of 10.5 A and a filament potential of 10 keV. This is the distribution produced as the electrons interact with the scintillation screen, and also multiple interactions and scattering, as well as broadening may increase the diameter.

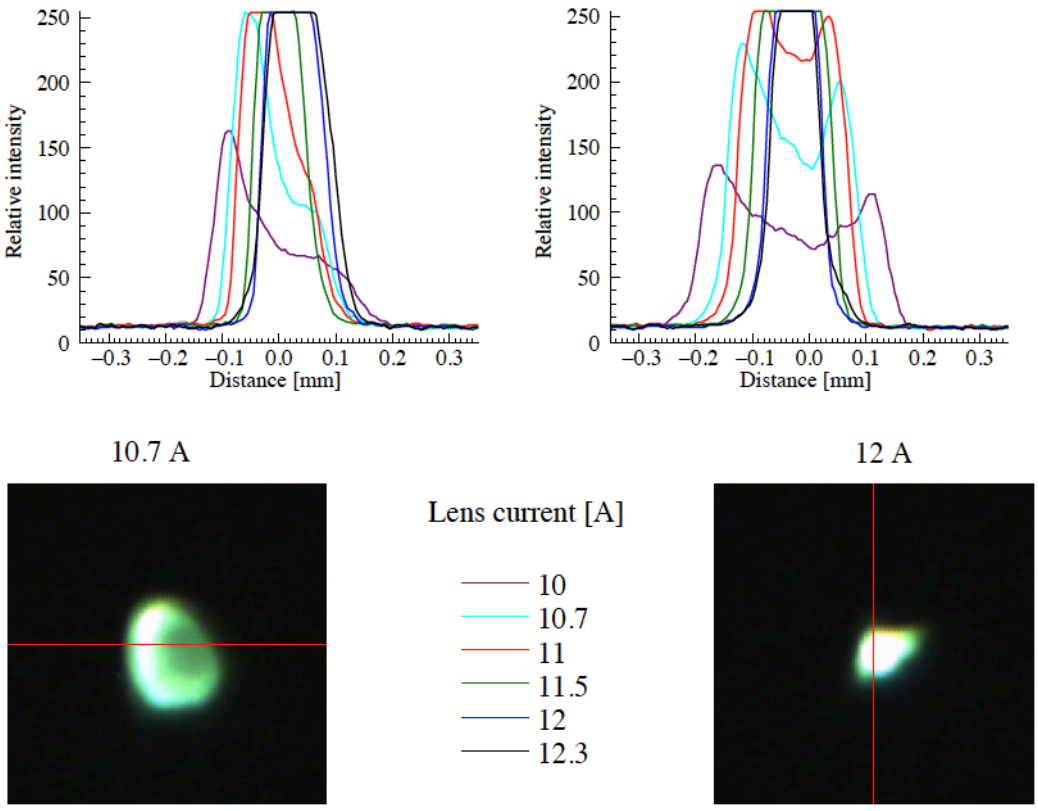

Figure 3.10. *Electron distribution at the X-ray target, estimated by conversion to visible light using a scintillator screen in both the horizontal (LHS) and vertical (RHS) direction.*

According to the above analysis it was clear that the phosphor images were saturated. To eliminate this natural density filter (ND 4) was fixed on the top of the exit glass window. The unsaturated results were presented in figure 3.9.

Figure 3.11 shows the electron spot size distribution variation with different lens current at filament potential of 10 keV.

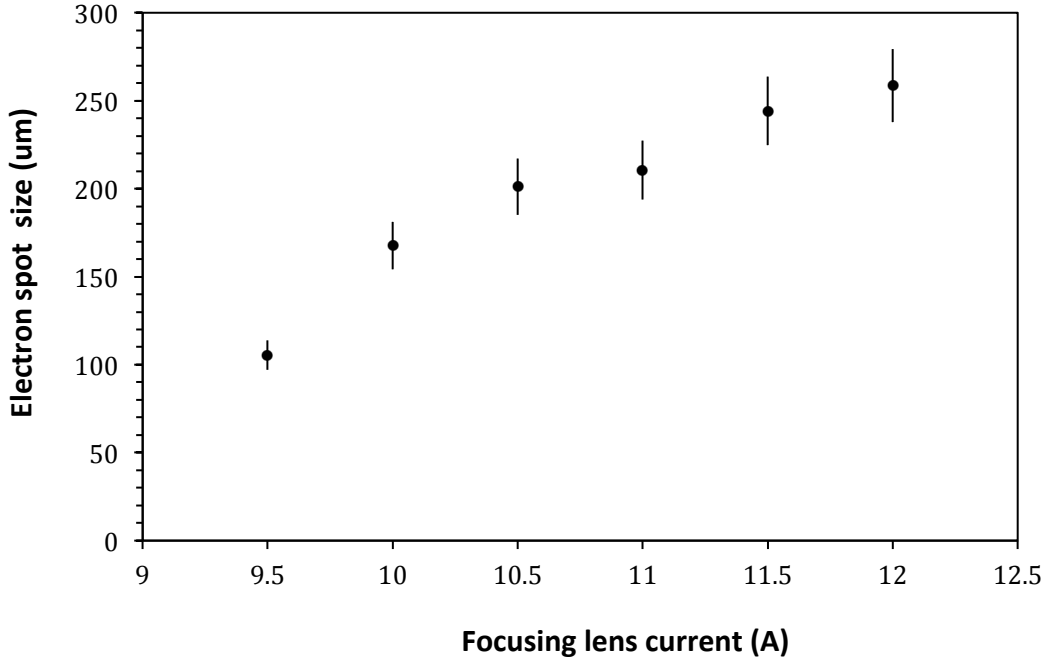

Figure 3.11. *Dependence of electron spot size with different focusing lens current. An error bars represent the calibration of the lens magnification.*

According to the above plot, an electron spot size on the phosphor screen increases with high lens current. When the lens current was reduced, the intensity of the electron spot also decreased. Therefore a small spot size can be obtained with low lens current.

The physical size of the X-ray source has also been estimated using a pinhole inserted in the manipulator arm to remove most of the X-ray signal. This acts as a pinhole camera when used with the CCD detector. A vacuum compatible X-ray CCD detector has been successfully coupled to the microfocus source, at the end of the X-ray path. This direct detection, back-

illuminated (Princeton Instruments PI-MTE in vacuum) (PI-MTE, Sept. 2011) detector used is specifically designed for in vacuum use, and is optimized for applications requiring detection of soft X-rays. The performance of the CCD chip has been described (Datasheet for CCD chip, Sept. 2011), with the overall performance of the detector summarized in table 3.1.

Pixel array size	2048 × 2048
Pixel size	13.5 μm
Detection efficiency at C K (0.278 keV)	50 %
Detection efficiency at Al K (1.487 keV)	70 %
Maximum operating energy	10 keV
Detector chip temperature (typical)	- 40^{o} C

Table 3.1. *Summery of the X-ray CCD properties when coupled to the microfocus X-ray source.*

The entire body of the detector (including the CCD chip, electrical and water coolant connectors) may be placed within a vacuum system. While this may ideal for certain applications, it requires a large vacuum chamber with additional manipulators, allowing positioning of the detector relative to the X-ray beam. As only the CCD chip is required to be contained within the vacuum chamber, a custom interface was designed in order to couple the detector to the microfocus source. This ensures the CCD chip is under vacuum conditions while the main body of the detector remains at atmospheric pressure.

The CCD chip is then cooled via a Peltier cooler, ensuring a low dark current in the detected image. The vacuum system ensures that condensation does not form on the CCD chip at cold temperatures. Operation of the detector at atmospheric conditions is also undesirable, due to the high attenuation of the incident soft X-rays. It is also essential that contaminations are kept away from the active area of the CCD chip. A hand operated gate value is therefore located immediately before the CCD chip along the X-ray path isolating the chip from the remaining vacuum system, and maintains a clean, debris free environment between experiments. The gate value also provided protection for the CCD chip during the transportation and installation on the microfocus source.

The resulting X-ray distribution produced by the pinhole camera is shown in figure 3.12. The X-ray was emitted by the carbon target pass through a pinhole of diameter of 50 μm. A visible light filter was used in this experiment and comprised a 2 μm thick titanium film mounted directly before the pinhole.

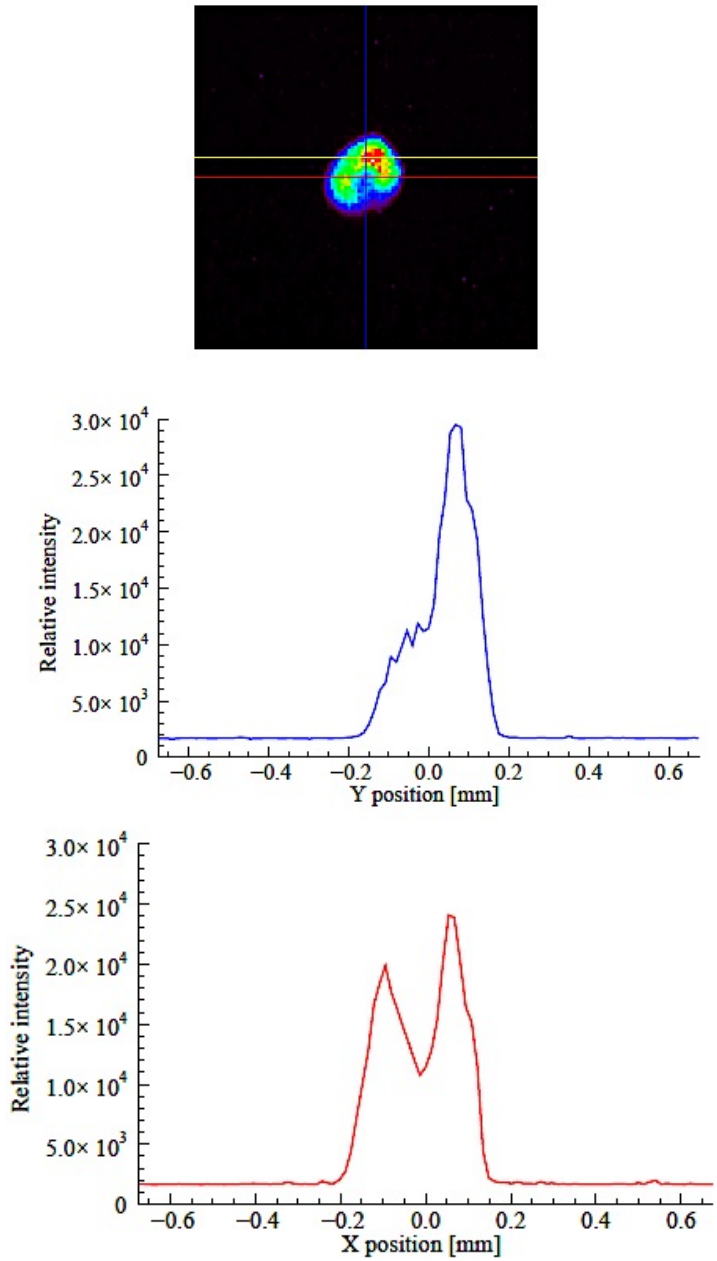

Figure 3.12. *The typical X-ray distribution measured using the X-ray pinhole camera. The distribution was produced using a focusing lens current of 10.5 A and the carbon target with pinhole of diameter of 50 μm.*

The total width of the X-ray distribution shown in figure 3.12 is approximately 300 μm. Considering the distance from the source to pinhole is 160 mm, and

the corresponding distance from pinhole to detector is 250 mm, the size of the X-ray emitting spot is ≈ 200 μm in diameter.

3.3 Silica mirror calibrations

The reflective properties of the silica mirror have been previously investigated using a simulation program (section 2.3).

The following figure 3.13 describes the arrangement for aligning and changing the Silicon mirror position.

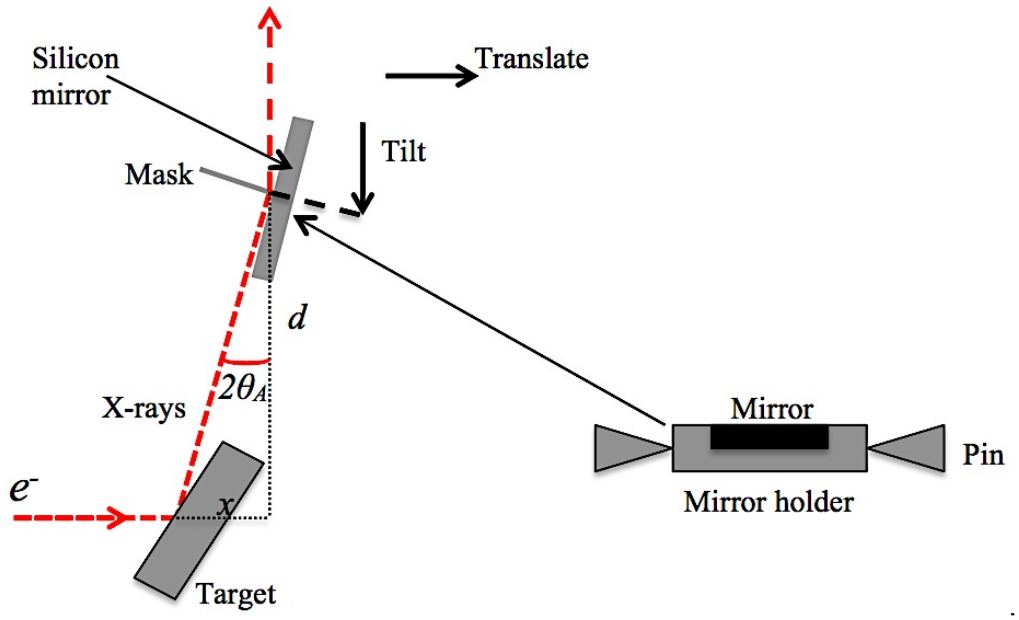

Figure 3.13. *Alignment of the mirror, required to produce a vertically oriented beam.*

The mirror holder was held between two ball-ended screws in a vertical position and was free rotate about a horizontal axis lying in the plane of the mirror surface. The screws protruded inwards from a C-shaped cup that

surrounded the mirror and was suspended beneath the optics assembly by two rods, one on either side. To tilt the mirror a thumbscrew-actuated micrometer was used. To maintain the vertical orientation of the beam after tilting the mirror to a selected grazing angle, θ_A, it was longitudinally translated a distance, x, in the direction of the beam. This distance is related to the tilt angle, and the vertical distance, d, from the source to the mirror axis, by the simple trigonometric relationship

$$x = d\tan\left(2\theta_A\right). \tag{3.7}$$

As it was impossible to determine the exact angle of the mirror *in-situ*, the tilt-translate alignment method relied upon positioning the mirror a predetermined distance, x, from the source and tilting it under X-ray illumination until a maximum signal was collected by the proportional counter. To ensure the mirror was being set to the grazing angle for the appropriate X-ray wavelength, the MCA channels from which the maximum counts were read were calibrated to the appropriate characteristic line in the unreflected X-ray spectrum.

Translation of the mirror was achieved by moving the entire optics assembly by a Vernier scale. Calculated translations for a range of grazing angles are shown in Table 3.2 for a silicon mirror.

Grazing angle, θ_A (^{o})	Beam deflection, $2\theta_A$ (^{o})	Translation, x (mm)
0.6	1.2	1.0
1.2	2.4	2.0
1.8	3.6	3.0
2.4	4.8	4.0
3.0	6.0	5.1

Table 3.2. *Mirror translations required achieving the necessary grazing angles.*

Due to the precision of the Vernier scale, the minimum repeatable translation increment was estimated to be 0.25 ± 0.1 mm. As this meant that mirrors could only be tilted in relatively coarse 0.15 ± 0.06^o steps, it was a design requirement that they be capable of maintaining near peak reflectivity over an angular range of ± 0.06^o from their specified grazing angle. Unreflected X-rays were prevented from passing through the vacuum window by the use of a mask, mounted on the mirror mounting cup, level with the rotation axis of the mirror, the straight bottom edge of a thin copper strip was positioned ~ 400 μm from the mirror surface. When the mirror was tilted by a degree, or more, this arrangement provided on line of sight yet allowed the reflected beam to fill the window.

3.3.1 Laser alignment of the Silica mirror

Once set to the appropriate angle, the tilt on the mirror was fixed and noted by using its micrometer. Monitoring the count rate and translating the entire optics assembly until a maximum signal was found easily regained the alignment between the source and exit window. This simple method was only successful because further tilting of the mirror was not required. However, in situations where the mirror had been tilted as well as moved, the correspondence between components was lost. Without any mechanical or electronic way of re-establishing an $x = 0$ position, defined as the point at which the mirror's rotation axis was directly above the center of the source, the only way of realigning the mirror appeared to be offline. Because this procedure was undesirable, as it involved bringing the vacuum system back up to atmospheric pressure, an alternative method was devised.

An obvious alternative procedure was to use a lens of suitably long focal length such that the bright source spot could be imaged directly through the vacuum window. Although this would have been possible, it would have requested the tilt and translation of the mirror to be adjusted simultaneously so that a line of sight could be established. Moreover, as a flat mirror only displaces the apparent position of the source and has no effects, there would have been no way of knowing is we were imaging the actual source or an image of it reflected off of the mirror itself. Therefore, it was decided to use a less ambiguous, laser alignment method that made use of a model 471830, 1 mW red (632.8 nm) helium-neon laser (LD Didactic, Hurth, Germany).

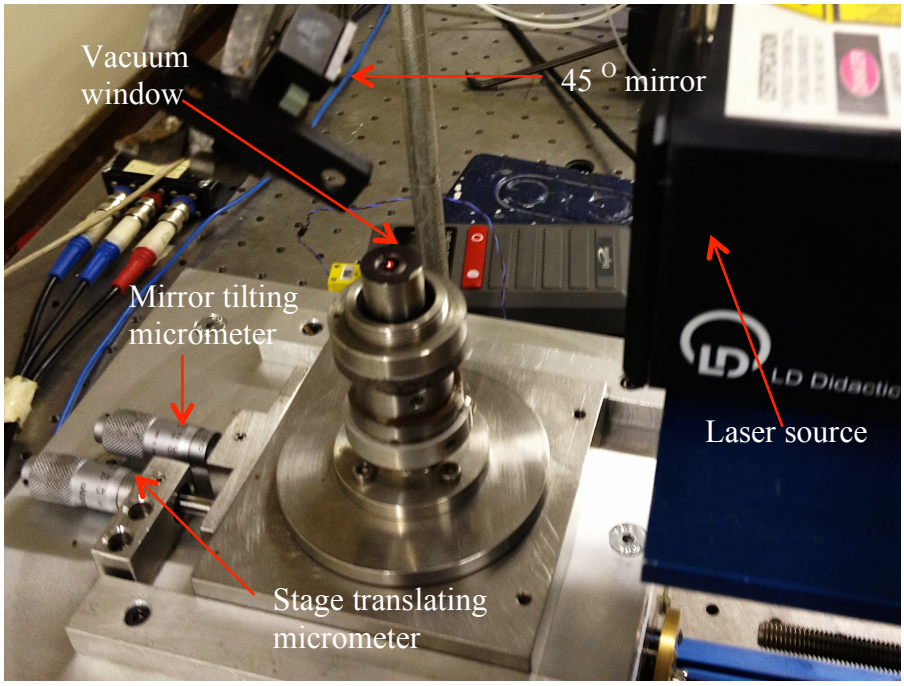

Figure 3.14. *The laser alignment set-up of the focusing elements of MK I source.*

The beam from the laser was bounced downwards off a silvered mirror that was set at a 45^{o} angle. Once the mirror was aligned the stage was moved until the laser beam passed down through vacuum window and a red spot was seen on the target face. Starting with the mirror at a sufficiently large an angle that there was no line of sight, the red spot was entirely due to the beam reflecting off the mirror (figure 3.15a). As the angle of the mirror was reduced, the spot was seen to move across the target until, when the angle was small enough, the mask no longer obscured line of sight and a second red spot appeared (figure 3.15b). As the mirror angle was reduced still further the reflected and transmitted spots converged, indicating the mirror was vertical (figure 3.15c).

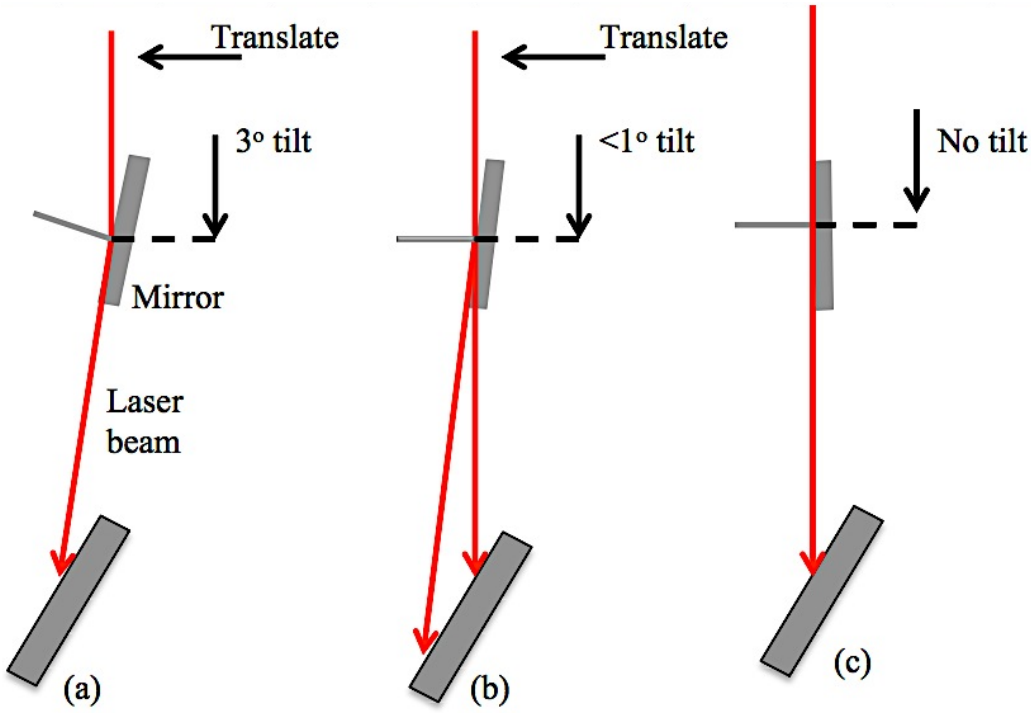

Figure 3.15. *Ray diagram describing the laser alignment method.*

Once the mirror was deemed vertical, the proportional counter was mounted above the silicon nitride window. Then, with the electron beam focused upon the target, the optics assembly was translated in the *z*- direction until the X-ray count rate was maximized. The mirror was then driven slightly forward, towards the electromagnetic focusing lens, until the count rate fell by half. At this point the mirror was obscuring one half of the source and the rotation axis was directly above it. By translating the mirror the required distance from this datum position (Table 3.2), the grazing angle was set by tilting the mirror until the count rate was maximized.

3.4 Summary

Particular attention and efforts have been spent to characterize and improve the X-ray source in order to achieve a high carbon K X-ray dose rate suitable for biological experiments. The effect of each single element forming the electron gun (i.e., filament current, anode voltage, filament-Wehnelt gap and the Wehnelt voltage) has been evaluated while monitoring the characteristic and bremsstrahlung X-ray dose rate. The optimum conditions are represented by a filament current of 2.9 A or higher (filament current limited by the filament life time) with the Wehnelt positioned at about 0.5 mm from the filament and with a relative voltage of 3 V. Under these conditions, a maximum flux of electrons can be extracted from the electron gun and directed towards the graphite target. The carbon K X-ray dose rate has also been measured as a function of the number of electrons hitting the graphite target (i.e. target current). Monitoring the target current is therefore possible to control that the X-ray dose rate stays constant during experiments.

The produced elections are focused to a spot to a few microns on the target using an electro-magnetic lens. The entrance of the lens has been increased from 1.0 mm diameter to a 2.5 mm diameter in order to collect higher number of electrons from the gun. This will result in an enlargement of X-ray source (i.e., electron spot on the target) and therefore of the final X-ray focus whose diameter is estimated to be ~ 200 μm. Two methods to calibrate the electro-magnetic lens are presented and discussed.

An arrangement designed to hold and position the silica mirror has been tested successfully. The effect of the mirror has been evaluated for different reflection angles. As expected, the background radiation was found to be negligible for most studies.

Chapter 4

MK III - an extensible micro-irradiation facility

4.1 Introduction

With increasing interest in the biological effects of low linear energy transfer radiation and the need to use more penetrating X-rays for tissue studies, it (soft X-ray microbeam project – MK I) was decided to upgrade to efficiently produce kilovolt X-rays (Folkard *et al.,* 2001b). By simply replacing the graphite target with one of aluminium or titanium (Schettino *et al.,* 2001a, Schettino *et al.,* 2003a), and using microstructured optical arrays (MOAs) instead of zone plates to optimize for the resulting 1.487 keV and 4.511 keV characteristic radiations, respective X-ray fluxes of 4×10^3 and 1×10^1 photons s^{-1} could be delivered to cellular targets (Schettino *et al.*, 2003b). Although by using more efficient MOAs, the dose-rate could have been increased without compromising the focused spot size, achievable gains would have been unlikely to reach a factor of ten. It was realized that in order to ensure the necessary order of magnitude increase in output, the performance of the X-ray source would require significant improvement. An electron gun was supplied by Kimball Physics (Wilton, NH, USA) and high voltage power supply unit from Glassman High Voltage Inc. (Glassman Europe Limited, UK). Features of the electron gun and power supply system are described in section 4.2.

4.2 MK III microfocus X-ray source

Figure 4.1 shows the new MK III microfocus source which, unlike MK I, is a modular system that can be easily upgraded in response to technical developments and future experimental need. The electron gun and target chamber are joined together by a 150 mm long custom build flight tube. This flight tube will support two pairs of deflector coils and electromagnetic focusing lens. The pressure in each chamber is monitored by an ionivac ITR-90 combined pirani-ion gauge and evacuated by a turbomolecular pump (Leybold Vacuum, London, UK) which is suspended through a large slot in the 1.5 × 1m optical bench (Melles Griot, Carlsbad, USA) upon which the source is built. A rotary pump located under the table provides backing pressure for the turbo pump. Instead of rubber 'O' rings, conflat flanges with metal gaskets [Ultra High Vacuum (UHV) technology,] are used on all critical vacuum seals. The vacuum level of $\sim 10^{-8}$ mbar is maintained throughout the system and a working vacuum of $\leq 10^{-9}$ mbar in the gun chamber.

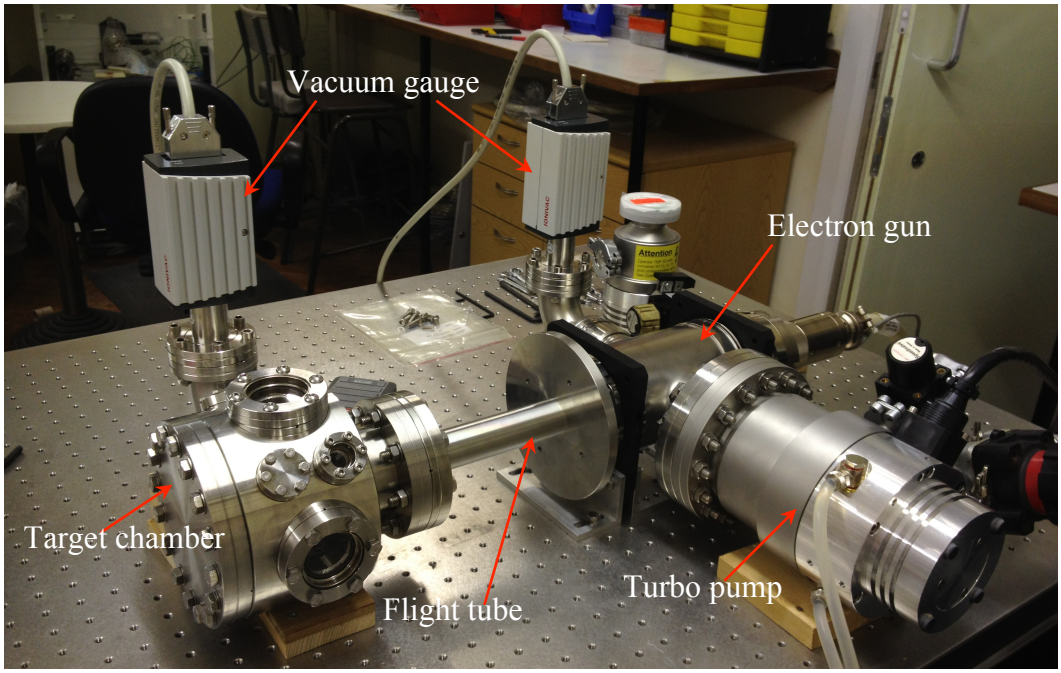

Figure 4.1. *The MK III source set-up. Target unit currently under construction and not shown in this figure.*

4.2.1 Electron gun

The Kimball Physics EGG-4200 electron gun is a multi-purpose modular electron gun. The gun has the capability of producing a high-energy electron beam. Beam current, beam divergence and beam energy are all adjustable over a wide range using different values of focusing optics. The electron acceleration energy can be varied from 1 keV to 30 keV and emission current is dependently adjustable from 1 μA to 4 μA. The firing unit of the electron gun is replaceable without removing the entire gun from the vacuum chamber. The firing unit included the cathode, cathode mount and Wehnelt aperture. This electron gun also facilitates the alignment of the firing unit with respect to the anode in real time while the gun is operating at full voltage with

beam on. The electron gun is bakeable to 350 ^{o}C with cables removed. The gun uses a custom LaB_6 guard ring cathode, consisting of a 1 mm carbon guard ring with a LaB_6 emitting surface in the center. The size of the emitting region can be changed from 50-300 μm according to experimental requirement.

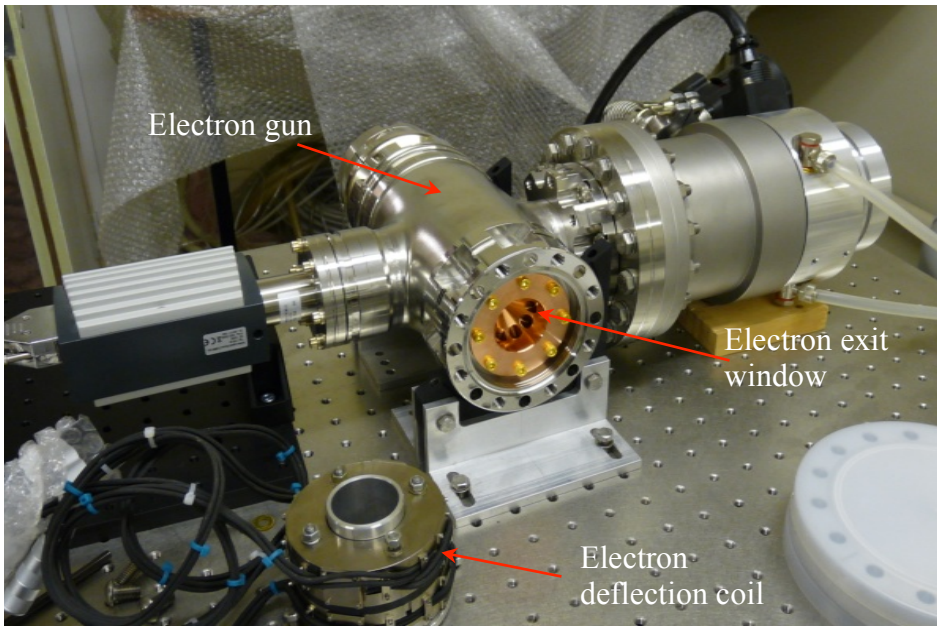

Figure 4.2. *EGG-4200 electron gun before installation.*

4.2.2 Electron gun power supply system

The electron gun is powered by an EGPS-4200 power supply system (Kimball Physics, Wilton, NH, USA). The EGPS-4200 has a modular design with small-scale power supply clusters, optically isolated signals and Flex Panel digital interface controller. This included computer control serial port (RS-232) and LabVIEW^{TM} computer program designed for remote computer control.

4.2.3 Calculated cathode properties

The ES-423E (extended life) cathode (Kimball Physics Inc., NH, USA) was procured for use in this electron gun. It comprised of a single LaB_6 crystal mounted on top of a carbon rod. The benefit of this type of mount, as opposed to that typically used for refractory cathodes, is the way in which the emitter is heated. Instead of flowing directly through the emitter, heater current flows through the base of the rod, causing it to heat up and thus, by conduction, heating the crystal indirectly. This gives improved emission stability and protects the crystal from thermal shock. The current density, J, at the surface of a thermionic cathode is calculated using the Richadson-Dushman equation (Richardson, 1912, Dushman, 1923, Richardson, 1924)

$$J = AT^2 \exp\left[\frac{-e\phi}{kT}\right] \tag{4.1}$$

where e is the charge of an electron, ϕ the work function of the cathode in volts, T is the emitter temperature in Kelvin and k is Boltzmann's constant, 1.38×10^{-23} m^2 Kg s^{-2} K^{-2}. Richardson's constant, A, may be found from

$$A_o = \frac{4\pi e m_e k^2}{h^3} \tag{4.2}$$

where m_e is the classical mass of the electron and h is Planck's constant. Supposedly a universal constant (Dushman, 1923, Richardson, 1924), A was found to vary from the theoretical value of 6.02×10^5 A m^{-2} K^{-2} if outgassed or 'impure' cathodes were used (Bridgman, 1926, DuBridge, 1928b). This variation was later attributed to the reflection of electrons back into the cathode

by impurities at the cathode surface (Wohlfarth, 1948). The 'constant' A was therefore re-expressed as

$$A = (1 - R)A_o \tag{4.3}$$

the product of $1 - R$, the probability of reflection, and $A_o = 1.204 \times 10^6$ A m^{-2} K^{-2}, a truly universal constant (Wohlfarth, 1948). Values of A are found experimentally.

Taking $A = 2.9 \times 10^5$ A m^{-2} K^{-2} and $\phi = 2.66$ V for LaB_6 (Lafferty, 1951), and $A = 1.204 \times 10^6$ A m^{-2} K^{-2} and $\phi = 4.53$ V for pure tungsten (Dushman, 1923), theoretical emission current densities, J were calculated for the two types of emitter. As Figure 4.3 clearly shows, for a given cathode temperature, LaB_6 can emit nearly five orders of magnitude more current than tungsten, the emission from the latter only being able to exceed the former at temperatures approaching its melting point (Kaye and Laby, 1995) where its lifetime will be very short (Bloomer, 1957). The ability to produce high current at low temperatures was a major reason for selecting a LaB_6 cathode.

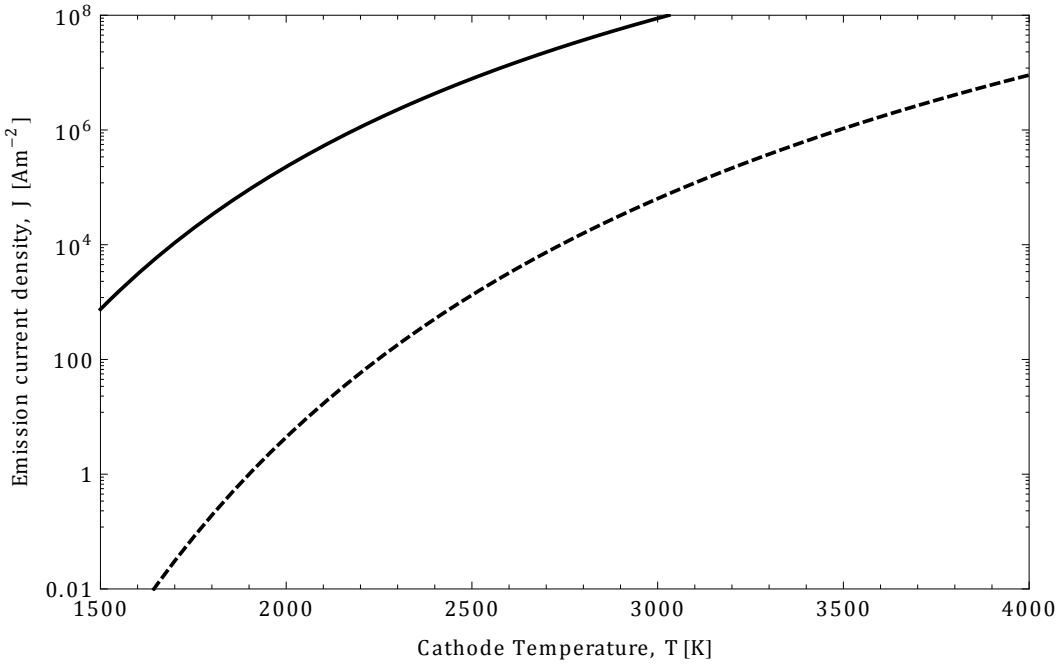

Figure 4.3. *Calculated emission current densities of lanthanum hexaboride (——) and tungsten cathodes (---) as a function of cathode temperature.*

Because emission from a LaB_6 cathode will depend on its temperature, this is a critical value to know. Unfortunately, cathode temperature is very difficult to determine *in-situ* and was not attempted. Instead, the cathode temperature was calculated at given heater current using a third order regression formula provided by the manufacturer (Kimball Physics, 2003a)

$$T = 41I^3 - 416I^2 + 1656I - 176 \quad (4.4)$$

This equation was determined by fitting a curve to the average measured temperatures, *T,* of ES-423E cathodes at fixed heater currents, *I.* Figure 4.4 shows the cathode temperature as a function of heater current.

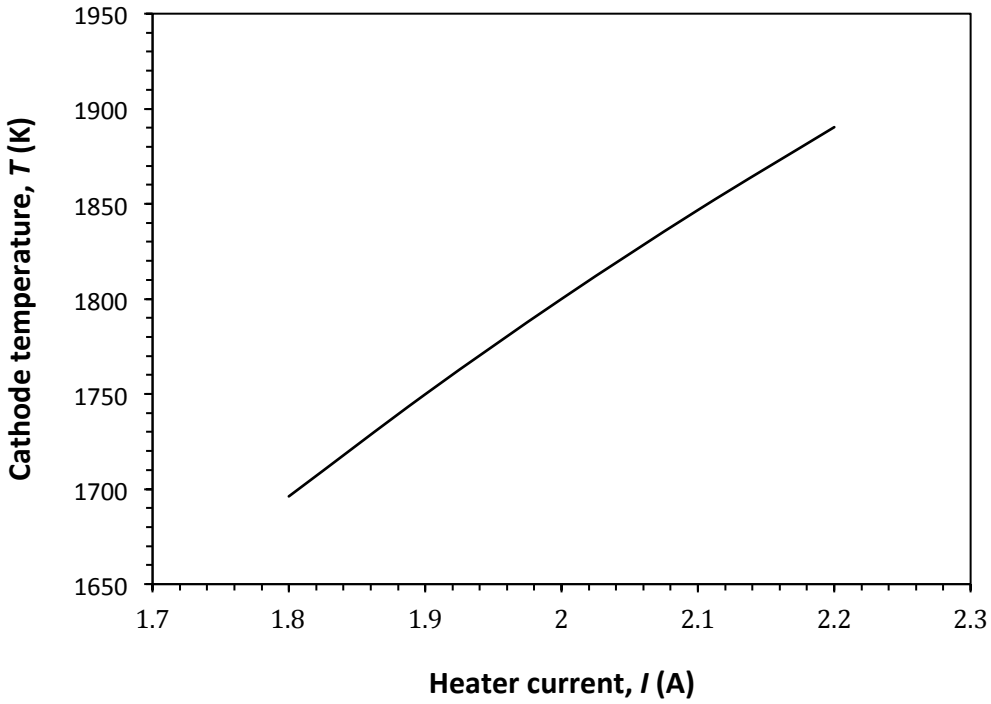

Figure 4.4. *Temperature of the lanthanum hexaboride cathode as a function of heater current.*

Cathode lifetime is a decreasing function of cathode temperature because the cathode material evaporates (Kimball Physics, 2003a) away more quickly at higher temperature. To balance the need for beam stability, adequate emission and maximum cathode lifetime, the cathode should be operated in the transition region between temperature and space charge limited modes.

To account for thermal field emission, the Richardson-Dushman equation is modified by subtracting the product of the Schottky constant, β_s (Schottky, 1914) and the root of the gun voltage, V, from the exponent (Dushman et al., 1925, DuBridge, 1928a, Humphries, 1990)

$$J = AT^2 exp\left(\frac{-e\phi - \beta_s V^{1/2}}{kT}\right) \tag{4.5}$$

The Schottky constant is given by

$$\beta_s = \left(\frac{e^3}{4\pi\varepsilon_o}\right)^{1/2} \tag{4.6}$$

where ε_o is the permittivity of free space. Using the Richardson-Dushman equation in its modified form, current densities were calculated for a 100 μm diameter LaB_6 cathode (surface area = 7.854×10^{-9} m^2) at heater current of 1.80 -2.20 A in 50 mA steps accelerating voltages of 10 – 15 kV (Table 4.1). These values differ by ~ 4 % from those of the manufacturer because of the choice of work function for LaB_6 (Sewell, 1991). Although emission was calculated for the microflat exclusively, in reality it occurs from all sides of the cathode.

	Emission current (mA)					
I (A)	10 kV	11 kV	12 kV	13 kV	14 kV	15 kV
1.80	0.110	0.111	0.113	0.114	0.116	0.117
1.85	0.151	0.153	0.115	0.157	0.159	0.161
1.90	0.203	0.205	0.208	0.211	0.213	0.216
1.95	0.268	0.271	0.275	0.278	0.282	0.285
2.00	0.348	0.352	0.357	0.361	0.366	0.370
2.05	0.445	0.451	0.456	0.462	0.467	0.473
2.10	0.561	0.568	0.575	0.582	0.589	0.596
2.15	0.698	0.707	0.716	0.725	0.733	0.741
2.20	0.859	0.870	0.881	0.891	0.901	0.911

Table 4.1. *Calculated emission current from a 100 μm diameter microflat according to equation 4.5.*

4.2.4 Wehnelt or Grid

The Wehnelt is a tubular structure that houses the cathode and has an aperture fixed to one end. The Wehnelt is also called the grid or control grid. Increasing the Wehnelt potential makes the Wehnelt aperture more negative with respect to the cathode. As the Wehnelt potential increases the electric field between the cathode and Wehnelt can suppress electron emission from the cathode perimeter, leaving only the centre of the of the cathode to emit.

Increasing the Wehnelt potential, practically experienced the beam completely suppressed. This grid cut-off can be used to pulse the electron beam off and on. The electric field created by the Wehnelt also controls beam divergence and uniformity by varying electron trajectory. The grid potential can be adjusted to optimize the efficiency of beam production.

4.2.5 Electron gun alignment

The goal of internal electron gun alignment is to produce an electron beam that travels down the gun column and through the center of the anode and focus lens apertures. This alignment was carried out using a phosphor screen [type of phosphor: ZnS:Ag (P-22 Blue)] fixed inside the target chamber. Figure 4.5 shows the evidence of phosphor screen image on the target position.

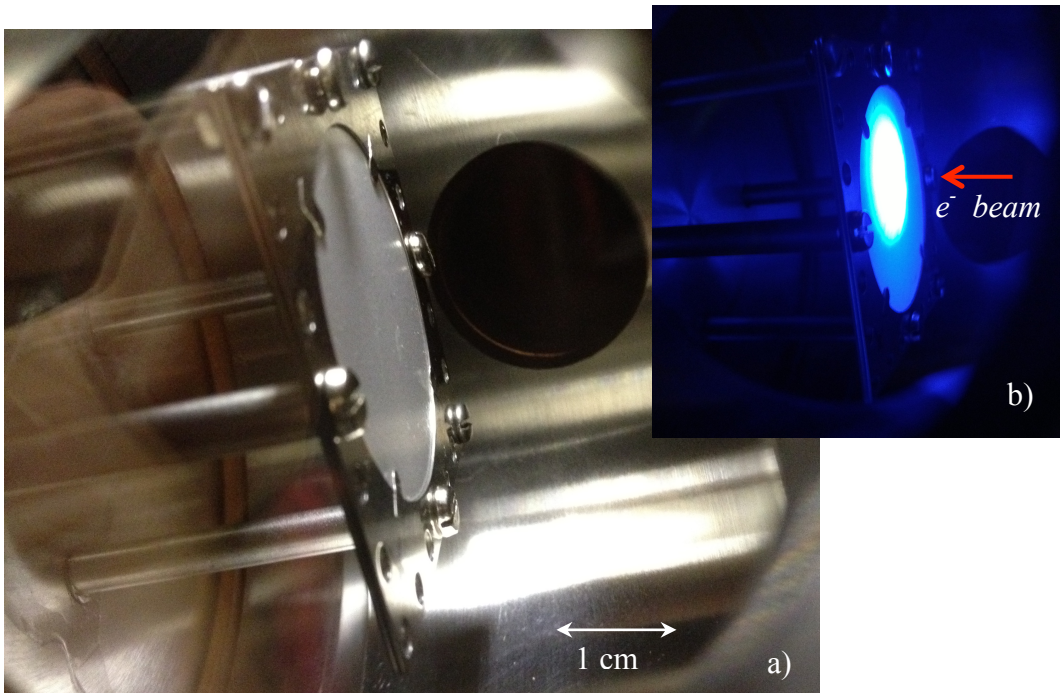

Figure 4.5. *Image a) shows the phosphor screen fixed inside the target chamber and b) indicates the evidence of aligning of electron gun. (Control parameters: 24.98 keV acceleration energy, 2.60 V source voltage and 324.5 V grid voltage)*

When the alignment screws on the feed through are turned in and out, they press on the spherical adjustment plate and cause the firing unit assembly to pivot back and forth. This allows the cathode in the firing unit to be aligned with the center of the stationary anode aperture. If the gun was aligned properly, the phosphor image shows a minimum diameter spot (focused spot) in the center, medium diameter spot (high focus voltage) and large diameter spot due to the low focus voltage. The minimum diameter spot was not very clear on above image (figure 4.5) due to high intensity of the incident electron beam.

4.3 Electron focusing lens design

Design the electron focusing lens, a simplified model of the electron gun, comprising only the three electrodes (LaB_6 cathode, grid electrode and anode), was constructed in AutoCAD (Autodesk, CA, USA). This model was feed into a program called MESH (Field Precision, NM, USA). This MESH program was used to create a structured mesh of triangular elements over the two-dimensional model space. A successfully generated MESH result was used to construct the electrostatic field within the gun using a program called ESTAT (Field Precision, NM, USA). The ESTAT input file, a short list of settings and boundary conditions in a specified order, was simple to construct with knowledge of finite element analysis. The first two settings were a scaling factor (DUnit), set to '1000' to indicate the model was in meters, and a geometry factor set to 'Cylin', a boundary condition telling the program that the model was circularly symmetric about the z-axis. These were followed by boundary conditions for the various objects and regions in the model. The first region, the model space was defined to be a vacuum with a relative dielectric constant (Epsi) of unity. Region 2, the grounded anode, was set to 0 V, whilst region 3 and 4, the cathode and microflat respectively, were floated at the accelerating voltage of the gun. The final region, the Wehnelt electrode, was given a slightly more negative bias than the cathode. Figure 4.6 shows the ESTAT simulation of the MK III electron gun.

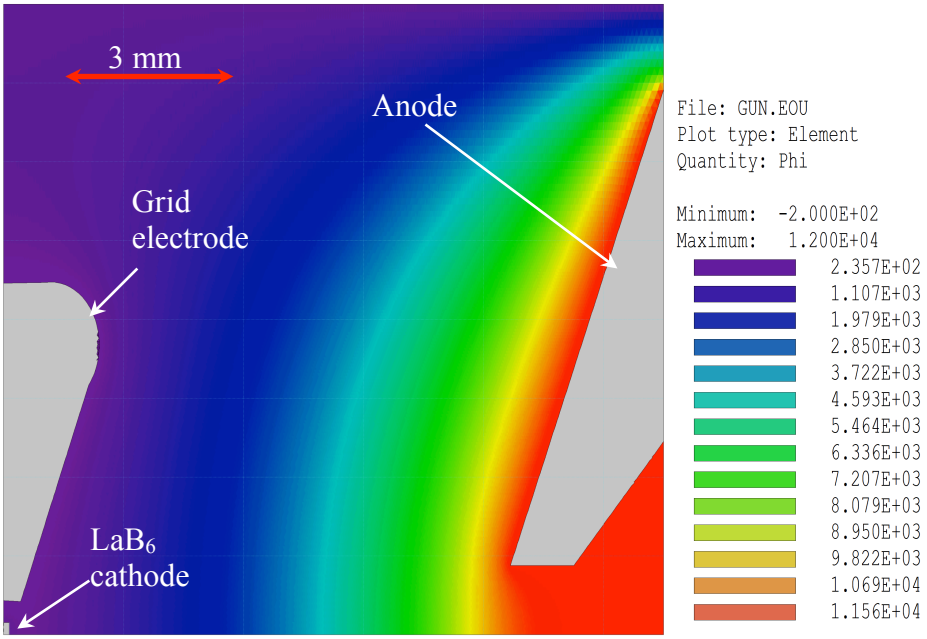

Figure 4.6. *Scale drawing and electric field simulation of MK III electron gun. Gray areas represent the field free zones with a conducting solid.*

Once the electric field with the gun had been calculated, the solution file was fed into the TRAK ray tracing program (Field Precision, NM, USA) along with its own input file. Also a simple list of commands, the TRACK input file is divided into three sections; fields, particles and diagnostics. In the 'fields' section the output file resulting from an ESTAT run (EFile), along with the scaling factor (DUnit) used, are specified. In the 'particles' section the SCHARGE mode is specified for assigning current, J, to a surface in a manner consistent with Child's law (Child, 1911, Langmuir, 1923)

$$J = \frac{4\varepsilon_o}{9}\sqrt{\frac{2eV^{3/2}}{m_e d^2}} \tag{4.7}$$

where ε_o is the permittivity of free space, e and m_e the charge and mass of the electron, and V and d the potential difference and distance between the cathode

and anode. Here, as the accelerating voltage is increased, the electron density at the surface grows until the repulsive electric field at the surface falls to zero, thus allowing electrons to escape. With the 'Emit' command, the microflat was defined as the emitting surface and passed several parameters including the relevance mass and charge of the electron, the number of electrons to be emitted, and the source-limited current density in m^2.

After each TRAK run was complete, the emission current was compared against that for a 100 μm diameter cathode at the same heater current (Table 4.1). If found to be too low, the grid voltage used in the ESTAT model was reduced and TRAK model was run again. This step was repeated until the grid voltage was low enough to produce an emission current equal to the source-limited value, the maximum possible in TRAK. The grid voltage was raised in steps until the emission become space-charge limited, the build up of negative charge constraining the emission. The grid voltages, exposing an electron source of constant size, were recorded for experimental use. The electron-focusing lens was designed to obtain a 10 μm electron spot at the target position. In MK I (Section 3.2) the focusing lens was single pole and due to low magnetic field strength it could not achieve much smaller diameter of electron spot. The new magnetic lens consisted of two poles. This soft-iron lens was under development and simulation results are shown in figure 4.7.

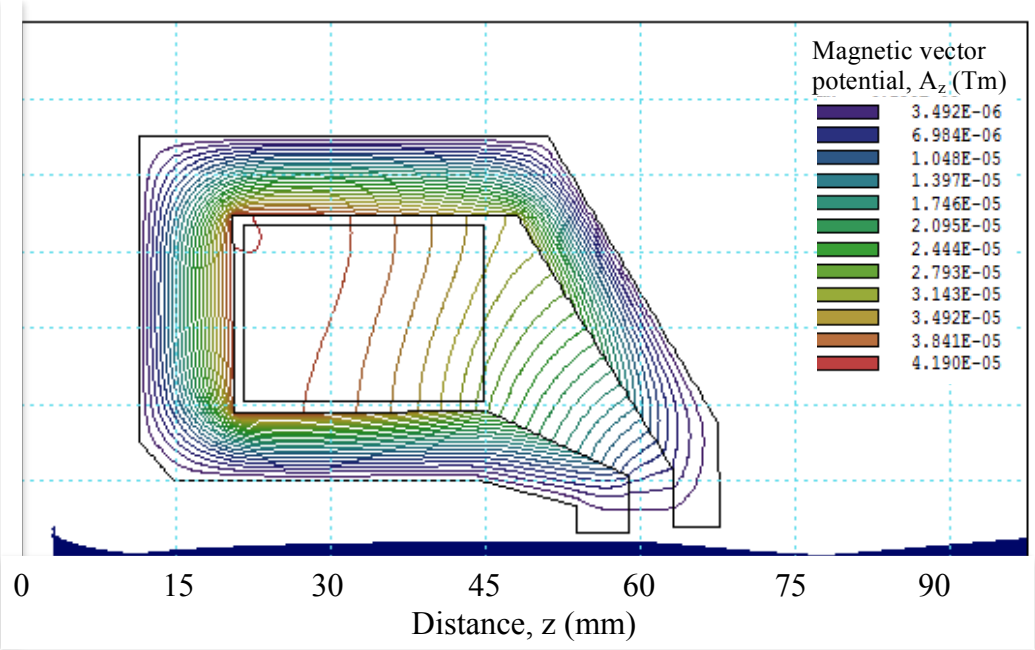

Figure 4.7. *Magnetic vector potential field lines in the two-pole piece electromagnetic lens (the lens coil consisting of 240 turns of copper wire and 12 V, 12 A drive current)*

Using a method analogous to that used when modeling the electron gun, the magnetic lens was drawn in AutoCAD (Autodesk, CA, USA) and a structured with the MESH program (Field Precision, NM, USA). I would like to acknowledge Saleh Alatabi, Radhwan Alnaimi and Daniel Adjei for their contribution to these simulations. Finite element magnetostatic analysis was then carried out using PERMAG (Field Precision, NM, USA). The calculated magnetic field strength along the axis of the electromagnetic field was found to be 0.335 T.

Once the magnetic field within the electromagnet had been determined, TRAK simulations were conducted for paraxial electron beams of varying diameter

and for realistic beams with different properties of cathode. Figure 4.7 shows the result of tracking a 2.5 mm diameter, 15 keV paraxial electron beam through the electromagnetic lens and indicates that the electrons are focused to a point roughly 8 mm from the outer pole piece. Similar simulations were conducted at beam energies in the range 15 - 25 keV, and showed that the maximum focal length was approximately 10 mm from the lens.

Unfortunately, while these simulations should have allowed the focal length and spot diameter to be accurately predicted, as the resolution of the mesh was in the tens of micrometers, this was not possible. Moreover, for similar reasons, the effects of space charge at the focal spot could not be investigated.

4.4 Summary

This chapter proceeded to discuss the advantages of boride cathodes over refractory metal in high brightness electron guns. It went on to calculate the different parameters of the 100 μm diameter lanthanum hexaboride cathode and Schottky effects. Development of a two pole pieces electromagnetic lens was described and the finite element analysis techniques employed in its design were explained. The results of ray tracing simulations, performed in order to establish the grid voltage required to give optimum beam currents for a range heater currents were presented. After the ray tracing simulations, performed in order to determine the expected focal length of the lens were monitored, the limitations of the model were explained.

Chapter 5

Conclusions and Future work

5.1 Conclusions

The work presented in this thesis describes the re-instating and calibration of an ultrasoft X-ray micro-irradiation facility for radiobiological studies. The project is followed from its theoretical conception to the calibration of a micro focus source. The main microfocus source investigated in this research is called MK I. It was initially used to study the optical characterization of Micro-Structured Optical Arrays. Several changes were carried out to make it suitable for radiobiological studies. The MK I can operate at 10 keV acceleration voltage with Carbon as a X-ray target material. Silica mirrors were introduced to the source to filter the bremsstrahlung component of Carbon K X-rays to obtain a nearly monochromatic X-ray beam. Theoretical simulations were conducted using the CXRO data program to determine the optimum reflection angle for a Silica mirror. A custom-built proportional counter was used to calibrate the X-ray output. A 0.5 μm thickness Mylar film was used as a counter window. This film was chosen because of low absorption of soft X-rays. For radiobiological experiments, the cells will be plated on the same Mylar film as that used for the counter window. Therefore, if all other factors are left unchanged, the corrected

number of photons absorbed in the counter is the same as that incident on the cells. The specially designed set up and the use of an infinity optics microscope allows the precise alignment of the focusing elements in a short time. The design allows X-rays to be brought to a focus outside the source vacuum window as vacuum represents an unacceptable condition for cells; X-ray attenuation will be minimized by filling the X-ray path with helium and leaving sufficient space for the micropositioning stage and microscope hardware.

Chapter 4 presented an extensible micro-irradiation facility called MK III. This system is currently under development and part of the system development was discussed. The MK III source composed a 30 keV electron gun and variable target materials. This is an advanced and sophisticated system compared to the MK I source. An electron gun and control system was obtained from Kimball Physics (Wilton, NH, USA). An electron focusing lens design was discussed in detail. Modeling of the focusing lens was carried out using commercially available software called Field Precision (Field Precision, NM, USA). According to the simulation, the proposed electromagnetic lens is able to focus a 15 keV paraxial electron beam, emitted from 100 μm cathode into ~ 10 μm spot in diameter. Instead of a tungsten cathode this source is fitted with a lanthanum hexaboride emitting surface in the center of the carbon guard ring.

5.2 Future work

To complete the MK I for cellular studies it is necessary to couple the focusing optics (i.e., zone plates) and appropriate OSA. According to the X-ray spot size at the target the zone plate characteristics can be calculated. A suitable OSA needs to be placed on the top of the focusing assembly to select first order X-ray focusing from the zone plate. This implementation will complete the MK I source for radiobiology studies.

At the present the MK I facility is not equipped with any arrangement to stop the focused X-ray beam from reaching the samples. Moving the samples away from the irradiation position is the only way to terminate the irradiation. This can be overcome by introducing an X-ray shutter to the MK I system. This can be achieved using a fast mechanical shutter placed between the filament and the target or by decreasing the anode voltage. This method will provide rapid termination of irradiation. The main disadvantage of this approach is the fact that the graphite target is not then hit by a continuous current of electrons but by a series of pulses. As a consequence, the characteristic of the X-ray source may change from pulse to pulse. The thermal variation caused in the target by the electron pulses may result in a fluctuating X-ray production rate and moreover in a change of the position of the electron focus on the graphite target. The position and the intensity of the X-ray focus may therefore not be stable during the experiment. The second approach is to stop the X-ray beam before reaching the samples without altering its production. In order to achieve this, a fast mechanical

shutter has to be installed between the graphite target and the samples. A suitable place for such a shutter could be immediately above the target. As the shutter will be electronically controlled by the PC, particular care has to be taken to prevent any stray electro-magnetic field produced by its operation interfering with the electron beam. The choice of a particular shutter and appropriate electro-magnetic shielding will therefore be necessary. The shutter will be automatically controlled by the PC and it is expected to terminate the irradiation in few tenths of millisecond.

The MK III source needs a designed target holder with a proper cooling system. This source is supposed to use different target materials (i.e., C, Al, Cr) and therefore a better cooling system must be introduced. A water-cooling system will be the most suitable option for this source. For cellular irradiation purposes focusing optics, a microscope system with a PC control software should be introduced to the MK III source.

References

1. Agarwal, B. K. (1991). "X-ray spectroscopy". London, Springer-Verlag: 18-38; 51-67.

2. Alpen, E. L. (1998). Radiation Biophysics, 2nd Edition, Academic Press, San Diego, ISBN 0120530856.

3. Atkinson, K. D., Folkard, M., Vojnovic, B., Schettino, G., Prise, K. M., Michael, B. D. and Michette, A. G. (2004). "Developing a Laboratory-Based Titanium K_α X-ray Microprobe". Extended Abstract from the 6th International Workshop on Microbeam Probes of Cellular Radiation Response. Radiat. Res. 161, 103-104.

4. Berger, M. J., Coursey, J. S., Zucker, D. S. and Chang, J. (2005b). ESTAR, PSTAR, and ASTAR: Computer Programs for Calculating Stopping-Power and Range Tables for Electrons, Protons, and Helium Ions, Version 1.2.3, National Institute of Standards and Technology, Gaithersburg, MD. http://physics.nist.gov/star.

5. Berger, M. J., Hubbell, J. H., Seltzer, S. M., Chang, J., Coursey, J. S., Sukumar, R. and Zucker, D. S. (2005a). XCOM: Photon Cross Section Database, Version 1.3, National Institute of Standards and Technology, Gaithersburg, MD. http://physics.nist.gov/xcom.

6. Berns, M. W., Wright W. H., Steubing R. W. (1991). “Laser microbeam as a tool in cell biology” International Review of Cytology 129: 1-44.

7. Bethe, H. A. (1930). “Zur Theorie des Durchgangs schneller Korpuskularstrahlen durch Materie” Ann. Phys. 5: 325-400.

8. Bethe, H. A. (1932). “Bremsformel für Elektronen relativistischer Geschwindigkeit” Z. Phys. 76: 293-299.

9. Bethe,. H. A and Ashkin,J. (1953). Passage of Radiations Through Matter in Experimental Nuclear Physics, (Eds,Segré,E.),John Wiley and Sons, New York, ASINB0000CIJHK.

10. Bettega, D., Calzolari P., Doglia S. M., Dulio B., Tallone L., Villa A. M. (1998). “Cell thickness measurements by confocal fluorescent microscopy on C3H10T1/2 and V79 cells” International Journal of Radiation Biology 74(3): 379-403.

11. Bloomer, R. N. (1957). The lives of electron microscope filaments, Brit. J. Appl. Phys. 8, 83-85.

12. Booz, J. (1978). Mapping of Fast Neutron Radiation Quality, Third Symposium on Neutron Dosimetry in Biology and Medicine, 499. Report No EUR 5848.

13. Booz, J., Feinendegen L.E. (1988). "A microdosimetric understanding of low-dose radiation effects" International Journal of Radiation Biology 53(1): 13-21.

14. Botchway, S. W., Stevens D. L., Hill M. A., Jenner T. J., O'Neill P. (1997). "Induction and rejoining of DNA double-strand breaks in Chinese hamster V79-4 cells irradiated with Characteristic aluminium K and copper L ultrasoft X-rays" Radiation Research 148: 317-324.

15. Braby, L. A., Reece W. D. (1990). "Studying low dose effects using single particle microbeam irradiation" Radiation Protection Dosimetry 31: 311-313.

16. Braby, L. A. (1992). "Microbeam studies of the sensitivity of structures within living cells" Scanning Microscopy 6(1): 167-175.

17. Brenner, D. J., Bird R. P., Zaider M., Goldhagen P., Kliauga P. J. Rossi H. H. (1987). "Inactivation of synchronized mammalian cells with low energy X-rays: results and significance" Radiation Research 110: 413-427.

18. Bridgman, P. W. (1926). The Universal Constant of Thermionic Emission, Phys. Rev. 27, 173-180.

19. Buckley, C. J., Browne M. T., Burge R. E., Charalambous P., Pgawa K., Takeyoshi T. (1988). "Zone plate for scanning X-ray microscopy: contamination writing and efficiency enhancement" in X-ray microcopy II. Eds. H. M. Sayre D., Kirz J., Rarback H., Heidelberg, Springer. Springer Series in Optical Sciences 56: 88-94.

20. Carpenter, S., Cornforth M. N., Harvey W. F., Raju M. R. Schillaci M. E., Wilder M. E., Goodhead D. T. (1989). "Radiobiology of ultrasoft X-rays IV. Flat and round-shaped hamster cells (CHO-10B HS-23)" Radiation Research 119: 523-533.

21. Catcheside, D. G., Lea D. E. (1943). "The effect of ionizing distribution on chromosome breakage by X-rays" Journal of Genetics 45: 186-196.

22. Chadwick, K. H., Leenhouts H. P. (1973) "A molecular theory of cell survival" Physics in Medicine and Biology 18(1): 78-87.

23. Charlton, D. E., Goodhead D. T., Wilson W. E., Paretzke H. G. (1985). "The deposition of energy in small cylindrical targets by high LET radiations" Radiation Protection Dosimetry 13: 123-125.

24. Child, C. D. (1911). Discharge From Hot CaO, Phys. Rev. (Series I) 32, 492-511.

25. Compton, A. H., Allison S. K. (1951). "X-rays in theory and experiments." in X-rays in theory and experiments. 2nd edition. Van Nostrand, Princeton (NJ): 614.

26. Cornforth, M. N., Schillaci M.E., Raju M.R. (1988). "Small volume (< 7 nm) energy depositions effective in producing isochromatid aberrations in CHO cells." Radiation Research Society Annual Meeting, Philadelphia: 137.

27. Cox, R., Thacker J., Goodhead D. T.(1977). "Inactivation and mutation of cultured mammalian cells by aluminum characteristics ultrasoft X-rays. II. Dose-response of Chinese hamster and human diploid cells to aluminum X-rays and radiations of different LET" Int. J. Radiat. Biol. 31(6): 561-576.

28. Datasheet for CCD chip. http://www.e2v.com/assets/media/files/documents/imaging-space-and-scientific-sensors/08-42-40-FI-AIMO-Cpak.pdf. Sept. 2011.

29. De Lara, C. M., Hill, M. A., Jenner, T. J., Papworth, D. and O'Neill, P. (2001). Dependence of the Yield of DNA Double-Strand Breaks in Chinese Hamster V79-4 Cells on the Photon Energy of Ultrasoft X Rays, Radiat. Res. 155, 440-448.

30. DuBridge, L. A. (1928a). The thermionic Emissions from clean platinum, Phys. Rev. 32, 961-966.

31. DuBridge, L. A. (1928b). The Photoelectric and Thermionic Work Functions of Outgassed Platinum, Phys. Rev. 31, 236-243.

32. Dushman, S. (1923). Electron Emission from Metals as a Function of Temperature, Phys. Rev. 21, 623-636.

33. Dushman, S., Rowe, H. N., Ewald, J. and Kidner, C. A. (1925). Electron Emission from Tungsten, Molybdenum and Tantalum, Phys. Rev. 25, 338-360.

34. Folkard, M. (2005). Radiation Damage to Biomolecules, International Workshop on Interdisciplinary Research with Slow Ion Beams, Caen, France.

35. Folkard, M., Schettino, G., Vojnovic, B., Gilchrist, S., Michette, A. G., Pfauntsch, S. J., Prise, K. M. and Michael, B. D. (2001b). A Focused

Ultrasoft X-Ray Microbeam for Targeting Cells Individually with Submicrometer Accuracy, Radiat. Res. 156, 796-804.

36. Folkard, M., Vojnovic B., Prise K.M., Bowey A.G., Lock R.J., Schettino G., Michael B.D. (1997). "A charged-particle microbeam: I. Development of an experimental system for targeting cells individually with counted particles" International Journal of Radiation Biology 72(4): 375-385.

37. Folkard, M., Vojnovic, B., Schettino, G., Atkinson, K. D., Prise, K. M. and Michael, B. D. (2007). A Variable-Energy Soft X-Ray Microprobe to Investigate Mechanisms of the Radiation-Induced Bystander Effect, US Department of Energy.

38. Folkard, M., Vojnovic B., Schettino G., Forsberg M., Bowey G., Prise K. M., Michael B. D., Michette A. G., Pfauntsch S. J. (1997b). "Two approaches for irradiating cells individually: a charged-particle microbeam and a soft X-ray microprobe" Nuclear Instruments and Methods in Physics Reaserch B 130: 270-274.

39. Friedl, A. A., Drexler, G. A., Deutsch, M., Strickfaden, H., Dietzel, S., Cremer, T., Hauptner, A., Krücken, R., Greubel, C., Habled, V. and Dollinger, G. (2006). Radiobiological Experiments at the Munich

Microprobe SNAKE, 7th International Workshop: Microbeam Probes of Cellular Radiation Response, New York, Radiat. Res. 161, 668-669.

40. Goodhead, D. T. (1987). "Biophysical models of radiation action: introductory review" Eds: Fielden, Fowler, Hendry and Scott: 306-311.

41. Goodhead, D. T. and Nikjoo, H. (1989). Track structure analysis of ultrasoft X-rays compared to high- and low-LET radiations, Int. J. Radiat. Biol. 55, 513-529.

42. Goodhead, D. T., Thacker J. (1977a). "Inactivation and mutation of cultured mammalian cells by aluminium characteristic ultrasoft X-rays. I. Properties of aluminium X-rays and preliminary experiments with Chinese hamster cells." International Journal of Radiation Biology 31(6): 541-559.

43. Goodhead, D. T. (1977b). "Inactivation and mutation of cultured mammalian cells by aluminium characteristic ultrasoft X-rays. III. Implication for theory of dual radiation action." International Journal of Radiation Biology 32(1): 43-70.

44. Goodhead, D. T., Thacker J., Cox R. (1979). "Effectiveness of 0.3 keV carbon ultrasoft X-rays for the inactivation and mutation of cultured

mammalian cells." International Journal of Radiation Biology 36(2): 101-114.

45. Gowen, J. W., Gay E. H. (1933). "Gene number, kind, and size in drosophila" Genetics, 8: 1-31.

46. Griffin, C. S., Stevens D. L., Savage J. R. K. (1996). "Ultrasoft 1.5 keV aluminium K X-rays are efficient producers of complex chromosome exchange aberrations as revealed by fluorescent in situ hybridisation" Radiation Research 146: 144-150.

47. Hall, E. J. and Giaccia, A. J. (2006). Radiobiology for the Radiologist, 6th edition, Lippincott Williams & Wilkins, Philadelphia, ISBN 0-7817-4151-3.

48. Henke, B. L., E. M. Gullikson, J. C. Davis (1993). "X-ray interactions: photoabsorption, scattering, transmission and reflection at E = 50-30000 eV, Z = 1 - 92 ". Atomic Data and Nuclear Data Tables 54(2): 181-342.

49. Herve du Penhoat, M. A., Fayard B., Abel F., Touati A., Gobert F., Despiney-Bailly I., Ricoul M., Sabatier L., Stevens D. L., Hill M. A., Goodhead D. T., Chetioui A. (1999). "Lethal effect of carbon K-shell

photo-ionisations in Chinese hamster V79 cell nuclei: experimental method and theoretical analysis" Radiation Research 151: 649-658.

50. Hill, M. A. and Goodhead, D. T. (2005). Do low energy electrons produce lesions characteristic of high-LET or low-LET radiation?, 52nd Annual Meeting of the Radiation Research Society, Unpublished. http://abstracts.co.allenpress.com/pweb/rrs2005/document/54336.

51. Hill, M. A., Stevens, D. L., Marsden, S. J., Allott, R., Turcu, I. C. E. and Goodhead, D. T. (2002). Is the increased relative biological effectiveness of high LET particles due to spatial or temporal effects? Characterization and OER in V79-4 cells, Phys. Med. Biol. 47, 3543-3555.

52. Humphries, S. (1990). Charged Particle Beams, John Wiley & Sons, New York, ISBN 0-471-60014-8.

53. ICRU (1989). Tissue substitutes in radiation dosimetry and measurement, International Commission on Radiation Units and Measurements, Bethesda, 44.

54. Jacobsen, C. (1999). "Soft X-ray microscopy" Trends Cell Biol 9(2): 44-47.

55. Kaye, G. W. C. and Laby, T. H. (1995). Tables of physical and chemical constrants, 16th edition, Lognman, Harlow, Essex, ISBN 0-582-226295.

56. Keller, A. M., Rossi H. H. (1972) "The theory of dual radiation action" Radiation research 8: 85-158.

57. Kimball-Physics (2003a). "ES-423 catalog JI2300124 graphs.jnb", Private Communication.

58. Khare, S. P., Wadehra J. M. (1996). "K-, L-, and M-shell ionisation of atoms by electron and positron impact" Canadian Journal of Physics 74: 376-383.

59. Kramer, H. A. (1923). "On the theory of X-ray absorption and of the continuous X-ray spectrum" Philos. Mag. 46: 836-871.

60. Kuzin, A. M., Wainson A. A. (1966). "Effect of alpha-particle microbeam irradiation on the synthesis deoxyribonucleic acid in tissue culture" Nature 212: 819-820.

61. Lea, D. E., Smith K. M. (1942a). "The inactivation of plant viruses by radiation. II. The relation between inactivation dose and size of virus" Parasitology 34: 227-237.

62. Lea, D. E. (1941). “The production and measurement of soft Roentgen rays for biological experiments” American Journal of Roentgenology 45: 614-619.

63. Lea, D. E., Catcheside D. G. (1942b). “The mechanism of the induction by radiation of chromosome aberrations in Tradescantia” Journal of Genetics 44: 216-245.

64. Lafferty, J. M. (1951). Boride Cathodes, J. Appl. Phys. 22, 299-309.

65. Langmuir, I. (1923). The Effect of Space Charge and Initial Velocities on the Potential Distribution and Thermionic Current between Parallel Plane Electrodes, Phys. Rev. 21, 419-435.

66. Long, X., Liu M., Ho F., Peng X. (1990). “Cross sections for K-shell ionisation by electron impact” Atomic data and nuclear data tables 45: 353-366.

67. Mak, B. K., Bird J. R. and Sabine T. M. (1966). “Proton microanalysis”. Nature 211: 38-73.

68. Master, J. and Schmahl G. (1992). “Coupled wave description of the diffraction by zone plates with high aspect ratios”. Opt. Comm. 89: 355-362.

69. Meger wells, C. M., Pearson D. W., De Luca P. M., Wells G. M., Cerrina F., Kennan W. S., Gould M. N. (1991). “Synchrotron-produced ultrasoft X-rays: a tool for testing biophysical models of radiation action” International Journal of Radiation Biology 59(4): 985-996.

70. Michael, B. D., Michette, A. G., Folkard, M., Prise, K. M., Pfauntsch, S. J., Buckley, C. J., Schettino, G., Forsberg, M., Turcu, I. C. E. and Allott, R. (1996). Use of Focused Laser Plasma Generated Soft X-Rays To Simulate The Biological Effects of Densely Ionising Radiations, CCLRC, Central Laser Facility Experimental Report. http://www.clf.rl.ac.uk/reports/1995-1996/pdf/CCLRC0715.pdf.

71. Michette, A. G. (1993a). X-Rays and their Properties in X-Ray Science and Technology, (Eds, Michette, A. G. and Buckley, C. J.), IOP Publishing, Bristol, 1-47, ISBN 075030233X.

72. Michette, A. G., Buckley C. J. (1993a). “Electron impact X-ray sources”. In: X-ray Science and Technology. Edited by The Institute of Physics, London: 48-63.

73. Michette, A. G., Buckley C. J. (1993b). “X-ray detectors”. In: X-ray Science and Technology. Edited by The Institute of Physics, London: 207-253.

74. Moreno, G., Salet C. (1985). “Cytotoxic effects following micro-irradiation of cultured cells sensitized with haemotoporphyrin derivative” International Journal of Radiation Biology 47(4): 383-386.

75. Motz, V. D., Quarles C. A. (1971). “The X-ray intensity ratios from electron bombardment” Nuclear Physics A164: 219-224.

76. Neary, G. J., Savage J. R. K., Evans H. J. (1964). “Chromatid aberration in tradescantia pollen tubes induced by monochromatic X-rays of quantum energy 3 and 1.5 keV” International Journal of Radiation Biology 8(1): 1-19.

77. Neary, G. J., Preston R. J., Savage j. R. K. (1967). “Chromosome aberrations and theory of RBE III Evidence from experiments with soft X-rays, and a consideration of the effects of hard X-rays ” International Journal of Radiation Biology 12(4): 317-345.

78. Nikjoo, H., Goodhead D. T., Charlton D. E. Paretzke H. G. (1989). “Energy deposition in small cylindrical targets by ultrasoft X-rays” Physics in Medicine and Biology 34(6): 691-705.

79. Paretzke, H. G. (1987). Radiation track structure theory. In: Kinetics of nonhomogeneous processes. Ed.: G. R. Freeman, New York, Wiley-Interscience: 89-170.

80. Perry, R. P. (1956). “Changes in the ultraviolet absorption spectrum of part of living cells following irradiation with an ultraviolet microbeam” Experimental Cell Research 12: 546-559.

81. Pierce, T. B., Peck P. F. and Cuff D. R. A. (1966). “Examination of surfaces by scanning with charged particles” Nature 211: 66-67.

82. PI-MTE in vacuum CCD detector. PI-MTE system manual. 3.D. Princeton Instruments. Mar. 2006.

83. Prise, K. M., Folkard, M., Davies, S. and Michael, B. D. (1989). Measurement of DNA damage and cell killing in Chinese hamster V79 cells irradiated with aluminum characteristic ultrasoft X rays, Radiat. Res. 117, 489-499.

84. Raju, M. R., Carpenter, S. G., Chmielewski, J. J., Schillaci, M. E., Wilder, M. E., Freyer, J. P., Johnson, N. F., Schor, P. L., Sebring, R. J. and Goodhead, D. T. (1987). Radiobiology of ultrasoft X rays. I. Cultured hamster cells (V79), Radiat. Res. 110, 396-412.

85. Randers-Pehrson, G. (2002). Microbeams, Microdosimetry and Specific Dose, Radiation Protection Dosimetry 99, 471-472.

86. Randers-Pehrson, G., Geard C., Marino S., Johnson G. (1993). "Development of the RARAF microbeam." 4th L.H. Gray Workshop: Microbeam probes of cellular radiation response, Gray Laboratory C.R.C., Northwood, UK: 4.3.1.

87. Randers-Pehrson, G. (1994). "Operating characteristics of the Columbia alpha-particle microbeam." Particle microbeam workshop, Pacific Northwest Laboratory, Richland, Washington:01.

88. Randers-Pehrson, G., Geard C., Johnson G., Brenner D. (1999). "Technical characteristics of the Columbia University single-ion microbeam" 4th International Workshop: Microbeam probe of cellular radiation response, Dublin, UK: 4.

89. Richardson, O. W (1912). Some applications of the electron theory of matter, Phil. Mag. 23, 594-619.

90. Richardson, O. W (1924). Electron emission from Metals as a Function of Temperaure, Phy. Rev. 23. 153-155.

91. Rufolph, D., Niemann B., Schmahl G. (1982). “Status of the sputtered sliced zone plate for X-ray microscopy”. Proc. SPIE 316: 103-105.

92. Schettino, G., Folkard, M., Prise, K. M., Vojnovic, B. and Michael, B. D. (2001a). Upgrading of the Gray Laboratory soft X-ray microprobe and V79 survival measurements following irradiation of one or all cells with a CK X-ray beam of different size, Radiation Protection Dosimetry 99, 287-288.

93. Schettino, G., Folkard, M., Prise, K. M., Wu, L., Atkinson, K. D., Vojnovic, B., Michette, A. G. and Michael, B. D. (2003a). Improvement of the GCI X-Ray Microprobe and Bystander Studies Using V79 Cells, 6th International Workshop: Microbeam Probes of Cellular Radiation Response, Oxford, Radiat. Res. 161, 112-113.

94. Schettino, G., Folkard, M., Michette, A. G., Vojnovic, B., Pfauntsch, S. J., Prise, K. M., Atkinson, K. D., Holroyd, J. and Michael, B. D. (2003b). The Gray Cancer Institute X-ray microprobe and its radiobiological applications, J. Phys. IV France 104, 301-304.

95. Schillaci, M. E., Carpenter S., Raju M. R., Sebring R. J., Wilder M. E., Goodhead D. T. (1988). “Radiobiology of Ultrasoft X-rays II. Cultured C3H Mouse Cells (10T1/2)” Radiation research 118: 83-92.

96. Schottky, W. (1914). Die Wirkung der Raumladung auf Thermionenströme im hohen Vakuum, Phys. Z 15, 872.

97. Seltzer, S. M. and Berger, M. J. (1985). Bremsstrahlung spectra from electron interactions with screened atomic nuclei and orbital electrons, Nucl.Inst.Meth.B12, 95–134.

98. Sewell, P. B. (1991). General Guidelines for Operating LaB6 Cathodes, Kimball Physics Inc., Wilton, Technical Bulletin # LaB6-01B. http://www.kimphys.com/cathode/support_PDF/LaB6_01B.pdf

99. Shand, M. T., (2012). "X-ray microprobe source characteristics". Personal communications.

100. Shimomura, T., Naruse S., Tekeda S. (1967). "Stomatogenesis and cell division in euplotes inhibited by ultraviolet microbeam irradiation" Nature 215: 91-92.

101. Smith, F. A. (2000). A Primer in Applied Radiation Physics, World Scientific, Singapore, ISBN 9810237138.

102. Sowa Resat, M. and Morgan, W. F. (2004). Microbeam developments and applications: A low linear energy transfer perspective, Cancer Met. Rev. 23, 323-331.

103. Sternheimer, R. M. (1952). The Density Effect for the Ionization Loss in Various Materials, Phys. Rev. 88, 851-859.

104. Sternheimer, R. M., Seltzer, S. M. and Berger, M. J. (1982). Density effect for the ionization loss of charged particles in various substances, Physical Review B 26, 6067-6076.

105. Tanno, Y., Kobayashi K., Tatsuka M., Gotoh E., and Takakura K. (2006). "Mitotic arrest caused by an X-ray microbeam in a single cell expressing EGFP-Aurora Kinase B" Radiation Protection Dosimetry 112: 301-370.

106. Thacker, J., Wilkinson, R. E. and Goodhead, D. T. (1986). The Induction of Chromosome Exchange Aberrations by Carbon Ultrasoft X-rays in V79 Hamster Cells, Int. J. Radiat. Biol. 49, 645-656.

107. Timofeeff-Ressovsky, N. W. (1934). "The experimental production of mutations" Biol.Rev. 9: 411-457.

108. Tschachotin, S. (1912). "Die mikroskopische Strahlenstichmethode, eine Zelloperationmethode" Biolog. Centralbl. 32: 623-630.

109. Uretz, R. B., Bloom W., Zirkle R. E. (1954). “Irradiation of parts of individual cells II. Effects of an ultraviolet microbeam focused on parts of chromosomes” Science 20: 197-199.

110. Virsik, R. P., Schafer C. H. Harder D., Goodhead D. T., Cox R., Thacker J. (1980). “Chromosome aberrations induced in human lymphocytes by ultrasoft Al (k) and C (k) X-rays” Int. J. Radiat. Biol. 38(5): 545-557.

111. Vladimirsky, Y., Kern D. P., Chang T. H. P., Attwood D., Ade H., Kirz J., McNulty I., Rarback H., Shu D. (1988). “High-resolution Fresnel zone plates for soft X-rays” J. Vac. Sci. technol. B6: 311-315.

112. Watt, F. (1982). “The Oxford 1 μm proton microprobe” Nuclear Instruments and Methods 197: 65-77.

113. Wilson, W. E., Paretzke H. G. (1981). “Calculation of distribution for energy imparted and ionizations by fast protons in nanometer sites” Radiation Research 81: 521-537.

114. Wohlfarth, E. P. (1948). Thermionic Emission Constants and Band Overlap, Proc. Roy. Soc. 60, 360-370.

115. Zirkle, R. E., Bloom W. (1953). “Irradiation of parts of individual cells” Science 117: 487-493.